

Materials Horizons

Accepted Manuscript

This article can be cited before page numbers have been issued, to do this please use: S. A. Talas, S. El-Hout, F. M. Alissa, J. K. El-Demellawi, P. Castaño, H. Mohamed, P. D. Kolubah, R. Khairova and M. Alqahtani, *Mater. Horiz.*, 2025, DOI: 10.1039/D5MH00905G.



This is an Accepted Manuscript, which has been through the Royal Society of Chemistry peer review process and has been accepted for publication.

Accepted Manuscripts are published online shortly after acceptance, before technical editing, formatting and proof reading. Using this free service, authors can make their results available to the community, in citable form, before we publish the edited article. We will replace this Accepted Manuscript with the edited and formatted Advance Article as soon as it is available.

You can find more information about Accepted Manuscripts in the [Information for Authors](#).

Please note that technical editing may introduce minor changes to the text and/or graphics, which may alter content. The journal's standard [Terms & Conditions](#) and the [Ethical guidelines](#) still apply. In no event shall the Royal Society of Chemistry be held responsible for any errors or omissions in this Accepted Manuscript or any consequences arising from the use of any information it contains.

Wider Impact Statement

This review discusses key advances in the application of MXene-based materials as electrocatalysts for CO₂ reduction, emphasizing their tunable surface chemistry, high conductivity, and structural robustness. The field has witnessed notable progress in understanding the role of composition, defect engineering, surface terminations, and heterostructure integration in tailoring catalytic performance and selectivity. These developments are of broad significance, as CO₂ electroreduction presents a direct link between greenhouse gas mitigation and renewable energy utilization, enabling the production of value-added chemicals and fuels under mild conditions. The study of MXenes intersects materials science, electrochemistry, and environmental engineering, making it of compelling interest for both fundamental research and industrial applications. As global energy and climate goals intensify, the demand for efficient, scalable, and sustainable catalytic platforms is set to rise. Insights from this review—especially those concerning the molecular-level mechanisms and synthetic strategies—will help guide the rational design of next-generation 2D catalysts with enhanced activity and stability. Ultimately, these contributions will influence the development of modular and deployable CO₂ utilization systems, shaping the future of materials science toward low-carbon technologies and circular economy models.



MXene-Based Electrocatalysts for CO₂ Reduction: Advances, Challenges, and Perspectives

Sawsan Abo Talas^{a1}, Pewee D Kolubah^{b1}, Rushana Khairova^b, Manal Alqahtani^c, Soliman I. El-Hout^d, Faisal M. Alissa^e, Jehad K. El-Demellawi^{e,f}, Pedro Castaño^{b,g*}, Hend Omar Mohamed^{b*}

^a Department of Chemical Engineering, Faculty of Engineering, Minia University, Minia, 61111, Egypt.

^b Multiscale Reaction Engineering (MuRE), King Abdullah University of Science and Technology (KAUST), Thuwal, 23955-6900, Saudi Arabia.

^c Biological and Environmental Science and Engineering (BESE) Division, Water Desalination and Reuse Center, King Abdullah University of Science and Technology, Thuwal 23955-6900, Saudi Arabia.

^d Nanostructured Materials and Nanotechnology Department, Advanced Materials Institute, Central Metallurgical Research and Development Institute, CMRDI, P.O. Box 87, Helwan, 11421, Cairo, Egypt.

^e Saudi Aramco, EXPEC Advanced Research Center, P.O. Box 5000, Dhahran, 31311 Saudi Arabia.

^f Center of Excellence for Renewable Energy and Storage Technologies (CREST), King Abdullah University of Science and Technology (KAUST), Thuwal, 23955-6900, Saudi Arabia.

^g Chemical Engineering Program, Physical Science and Engineering (PSE) Division, King Abdullah University of Science and Technology (KAUST), Thuwal, 23955-6900, Saudi Arabia.

¹ These authors contributed equally

* Corresponding authors: pedro.castano@kaust.edu.sa, hend.mohamed@kaust.edu.sa



Abstract

The electrochemical reduction of carbon dioxide (CO₂) is a crucial step toward a sustainable carbon economy, enabling the conversion of greenhouse gases into valuable fuels and chemicals. Among the emerging materials for this transformation, two-dimensional (2D) MXenes comprising transition-metal carbides, nitrides, and carbonitrides are notable due to their tunable surface chemistry and high conductivity. This review comprehensively analyzes recent advancements in MXene-based electrocatalysis for the CO₂ reduction reaction (RR) and explores the unique electronic properties of MXenes that drive their catalytic performance. Composition, surface terminations, defect engineering, and interfacial dynamics dictate activity and selectivity and are analyzed to contextualize the structure-function correlations. This work discusses state-of-the-art strategies to enhance MXene-based electrocatalysts, including compositional modifications, heteroatom doping, and heterostructure integration. Mechanistic insight regarding CO₂RR is examined to pinpoint the advantages and challenges of MXenes in the overall reaction network. Finally, this work presents a forward-looking perspective, outlining challenges and emerging opportunities for MXenes in driving sustainable CO₂ electrocatalytic conversion technology.

Keywords: Carbon dioxide (CO₂) capture and storage, electrocatalyst, two-dimensional materials, CO₂ reduction



1. Introduction

Energy and environmental sustainability are essential for the continuation of life on the planet and have recently risen to the forefront of global concerns.^{1,2} The overutilization of natural resources, combined with unsustainable production and consumption practices such as fossil-fuel combustion, deforestation, and industrial processes, has led to extensive environmental degradation and the emergence of climate change via CO₂ emissions.^{3–5}

Global energy consumption is projected to increase by about 80% by 2030, potentially driving CO₂ levels and associated warming even higher without proactive mitigation.⁶ According to the Intergovernmental Panel on Climate Change (IPCC), anthropogenic greenhouse gas emissions raised average surface temperatures by 1.1°C above the pre-industrial levels from 2011 to 2020, with more severe impacts to follow absent substantial emission reductions.⁷ As shown in Figure 1A, global temperatures have increased and are expected to continue rising throughout the lifespans of three representative generations born in 1950, 1980, and 2020. Projections indicate that, without proactive mitigation measures, global surface temperatures could rise by up to 4°C by 2100, underscoring the urgent need for collective action across governments, industry, and civil society.

The CO₂ capture, storage, and utilization (CCSU) strategies aim to mitigate these emissions by capturing CO₂ from major point sources (power plants, gas-processing facilities, industrial sites), purifying, compressing it, and injecting it into deep geological formations (depleted reservoirs, saline aquifers, coal seams) for long-term sequestration. The choice of capture method (pre-combustion, post-combustion, or oxy-fuel combustion) depends on the CO₂ concentration, required purity, and pressure of the emission stream. Those strategies are considered vital tools that could reduce global CO₂ emissions by up to 32 % by 2050 (Figure 1B).^{8–15} The CCS provides the CO₂ feedstock for utilization pathways, enhanced oil recovery, construction materials, chemical and fuel synthesis, and agricultural applications, creating value and supporting a circular-carbon economy.¹⁶ However, the thermodynamic stability of CO₂ requires high energy



input for the chemical activation and conversion of the $\text{O}=\text{C}=\text{O}$ molecule into hydrocarbons, alcohols, or oxygenates.

Four primary catalytic approaches have been explored for CO_2 conversion: thermal, electrochemical, photocatalytic, and photothermal catalysis. In thermal catalysis, CO_2 is converted through high-temperature reactions such as hydrogenation and dry reforming with methane (CH_4), typically conducted at elevated pressures and above-atmospheric conditions.¹⁷ Photocatalysis mimics natural photosynthesis, using solar energy to generate electron-hole pairs that migrate to the catalyst surface and drive redox reactions with adsorbed CO_2 species.¹⁸ Photothermal catalysis combines photochemical and thermochemical pathways to enhance reaction rates. This approach operates at lower temperatures than conventional thermal methods by harnessing the synergistic effects of semiconductor excitation and localized heating induced by plasmonic or nonplasmonic nanostructures.^{19,20}

Among these approaches, electrocatalysis offers a uniquely advantageous route for CO_2 utilization by directly coupling with renewable electricity. Unlike thermal processes that depend on externally produced H_2 (e.g., via water electrolysis), electrochemical CO_2 reduction (CO_2RR) proceeds via a proton-coupled electron transfer (PCET) mechanism. This enables CO_2 conversion under mild operating conditions, typically at room or moderately elevated temperatures ($<100^\circ\text{C}$) and ambient pressure, making it energy-efficient and scalable.²¹ The CO_2RR can generate a wide range of high-value products, including carbon monoxide (CO), formic acid (HCOOH), ethylene (C_2H_4), ethanol ($\text{C}_2\text{H}_6\text{O}$), and propanol ($\text{C}_3\text{H}_8\text{O}$).²² However, the competing hydrogen evolution reaction (HER), which reduces product selectivity by diverting electrons toward H_2 production, remains a key challenge.

All CO_2RR products possess commercial relevance, and their selectivity can be tailored through rational design of the reaction environment, namely, electrolyte composition, reactor configuration, and, most critically, catalyst engineering.^{23,24} By tuning catalyst morphology, elemental composition, exposed crystal



facets, and defect structures, researchers aim to enhance catalytic activity, boost selectivity for specific products, and improve long-term operational durability.²⁵

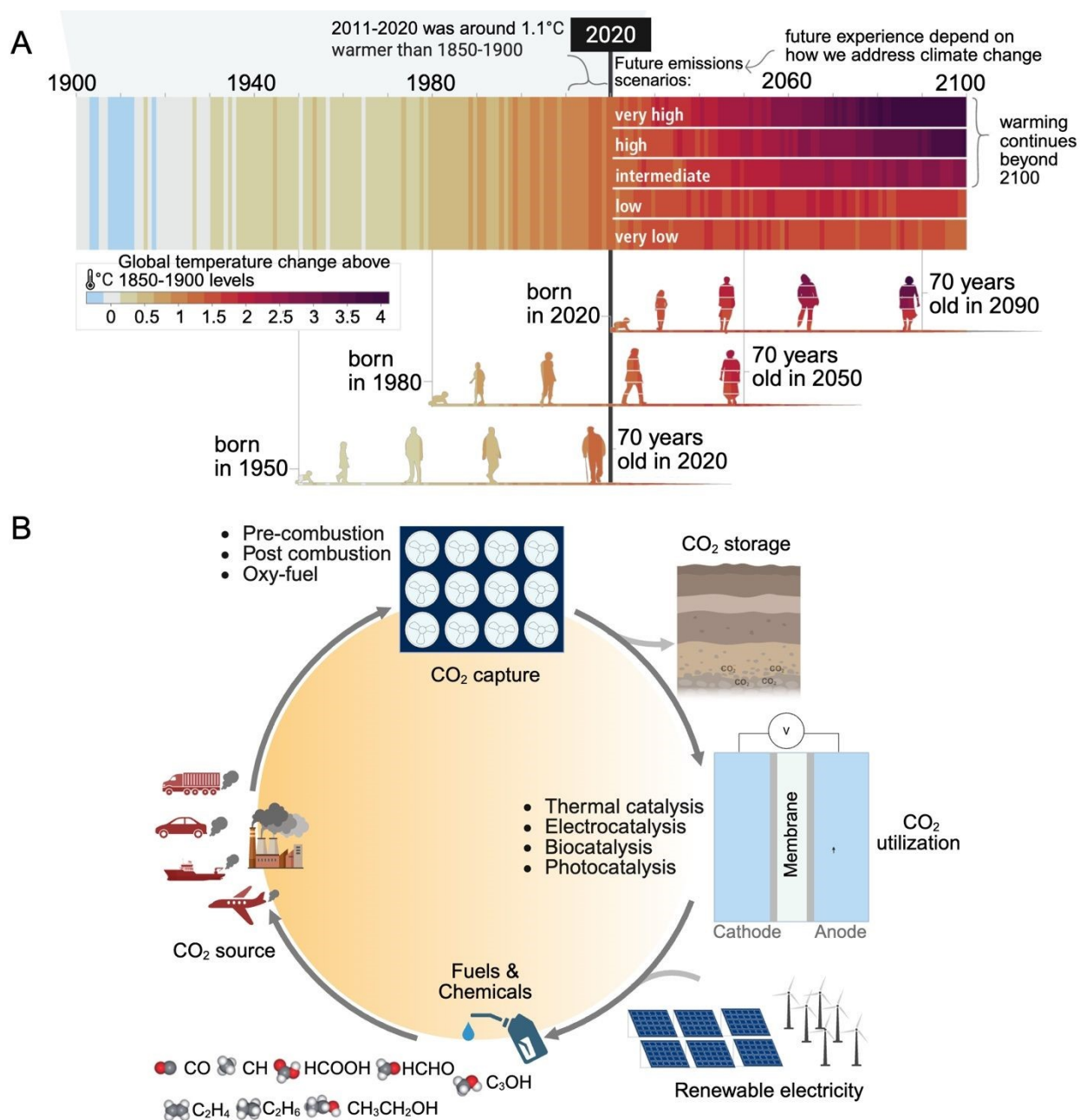


Figure 1. Circular economy: A) Observed (1900–2020) and projected (2021–2100) changes in global surface temperature (relative to 1850–1900), which are linked to changes in climate conditions and effects, illustrate how the climate has already changed and will change along the lifespan of three representative generations (born in 1950, 1980 and 2020) “Reproduced from reference [7] with permission from IPCC, Copyright [2023]”. B) Schematic of CO₂ capture, storage, and utilization for fuels and chemicals production.

Despite rapid progress in electrocatalytic CO₂RR, many conventional catalyst systems, such as transition metals, metal oxides, and carbides, suffer from low selectivity, poor product formation rates, and rapid deactivation.²⁶ As a result, significant research has focused on engineering more effective catalytic architectures, including alloy catalysts, metal–support hybrids, and heterostructures that enhance CO₂ activation, suppress the competing HER, and improve long-term stability.^{27–29}

Recent years have seen a few breakthrough studies that define the current performance frontier for CO₂RR. For instance, Wang et al.³⁰ developed a fluorine-modified copper (Cu) catalyst integrated into a flow-cell reactor, achieving an unprecedented current density of 1.6 A cm⁻², > 80 % C₂⁺ Faradaic efficiency (FE), and 16.5 % single-pass yield under ambient conditions. The fluorine surface functionalization was shown to enhance water activation and stabilize key CHO intermediates, thus promoting C–C coupling and boosting multicarbon product selectivity. Sargent et al.³¹ demonstrated that pairing a strong-acid electrolyte with an atomically sputtered planar Cu catalyst yields > 90 % C₂⁺ FE, 78 % single-pass CO₂ utilization, and 30 % energy efficiency for C₂⁺ products, with an exceptionally low energy cost of 249 GJ t⁻¹ for ethanol production. While promising, the synthesis approach is complex and cost-intensive, posing scalability challenges. Yang et al.³² achieved 97 % CO selectivity at –0.5 V vs. RHE and a specific current of 350 A g⁻¹ using nickel (Ni) single atoms supported on N, S-co-doped graphene. A 100 h durability test confirmed long-term operational stability, and DFT calculations revealed that the non-centrosymmetric ligand environment around Ni(I) significantly enhanced adsorption strength for CO₂ and key intermediates. These breakthroughs illustrate how combining precise atomic-level design, reactor integration, and advanced surface engineering can collectively overcome long-standing CO₂RR challenges. Yet despite such advances, broader challenges remain in scalability, cost, and long-term performance, motivating exploration of new catalyst platforms.

Among the most promising emerging materials are two-dimensional (2D) systems, including graphene, transition-metal dichalcogenides (TMDs), layered double hydroxides (LDHs),²³ and the newest class—MXenes. MXenes are a family of 2D transition-metal carbides, nitrides, or carbonitrides, known for their



high electrical conductivity, tunable surface chemistry, excellent mechanical integrity, and abundant redox-active sites, making them particularly attractive for CO₂RR applications.^{25,33–40} For instance, their metallic conductivity facilitates electron transport for complex proton-coupled electron transfer (PCET) steps. Surface terminations (e.g., –O, –OH, –F) can be engineered to steer intermediate adsorption and reaction pathways, while their robustness supports long-term operation under electrochemical conditions. However, despite these promising features, most experimental MXene-based CO₂RR studies focus on Ti₃C₂T_x, due to the ease of synthesis and well-established chemistry.⁴¹ The field remains in its early stages: over 80 % of reported studies are theoretical, relying on quantum mechanical calculations to evaluate CO₂ binding, activation energies, and selectivity trends.⁴² Experimental progress lags due to synthesis challenges, such as controlling etching, delamination, defect density, and surface terminations, affecting catalytic performance and reproducibility.

This review provides a comprehensive overview of recent progress in MXene-based catalysts for CO₂RR. A brief overview of CO₂RR covers general reaction mechanisms, pathways for various product groups (e.g., hydrocarbons, alcohol, and oxygenates), critical intermediates governing product formation, and the internal and external factors influencing the overall system architecture. Next, this work explores the distinctive chemical and structural properties of MXenes that support their catalytic potential for CO₂RR, highlighting how they differ from conventional CO₂RR catalysts.

A critical assessment of recent developments in catalyst design and modification strategies follows, particularly on progress in operational parameters that significantly affect catalytic activity and selectivity. Then, this work explores the electrocatalytic mechanisms of CO₂RR regarding MXene-based catalysts. This work discusses how these mechanisms can be optimized to enhance CO₂ conversion efficiency and steer product selectivity, underscoring the novelty and promise of MXene-based catalysts. Additionally, critical factors affecting CO₂RR performance, including electronic properties, surface chemistry, and electrolyte interactions, are reviewed. Finally, this work provides a forward-looking perspective, emphasizing the

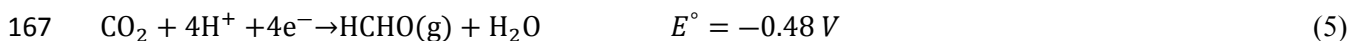


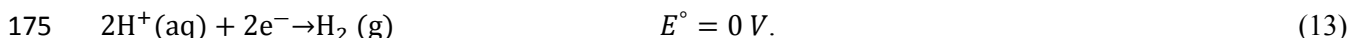
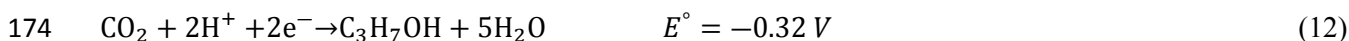
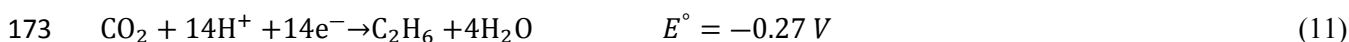
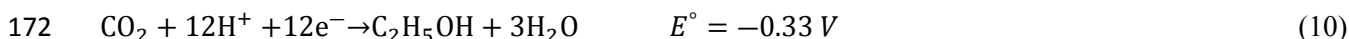
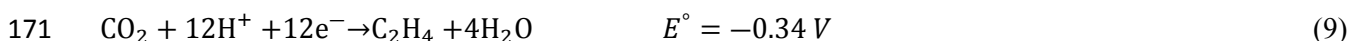
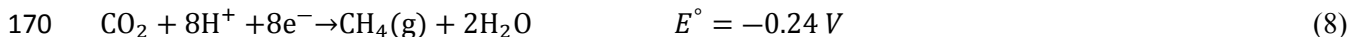
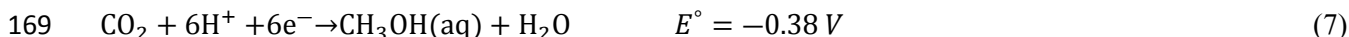
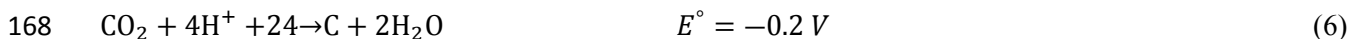
necessity of a systematic approach to developing cost effective MXene-based catalysts for practical application.

2. Fundamentals of the CO₂ Reduction

In a CO₂ electrolyzer, the anode and cathode reactions occur in separate chambers, divided by an ion-conducting membrane. The CO₂RR electrolyzers have distinct configurations, including H-cell, membrane electrode assembly (MEA), and microfluidic cells.⁴³ These reactor configurations have an anode and a cathode. At the anode, water is oxidized to produce molecular oxygen (O₂; Eq. 1), whereas at the cathode, CO₂ is reduced into C-containing species (Figure 2a). An external energy input is required to drive the overall reaction. From a thermodynamic perspective, the potential required to drive the one-electron reduction of CO₂ to the CO radical is -1.9 V vs. the standard H electrode (Eq. 2), making the reaction highly energy-intensive and thermodynamically unfavorable in the absence of an appropriate catalyst.⁴⁴ The formation of CO₂RR products is influenced by the PCET process involving electron transfers ranging from 2 to 18 e⁻ per CO₂ molecule (Eq. 3–12).^{45–47}

Although the proton-assisted process enables forming a wide range of products, achieving the selective production of the desired compounds remains a significant challenge due to the similar redox potentials of competing reaction pathways. Selectivity limitations are exacerbated in aqueous electrolyte-based CO₂ electrolyzers, where the HER occurs at a comparable potential (Eq. 13), directly competing with CO₂RR:





Depending on the available catalyst surface during the reaction, CO_2 is activated and converted into intermediates. These intermediates transform into final products via distinct mechanistic pathways (Figure 2B).⁴⁸ The paths are classified into C_1 products (CO , HCOOH , methanol (CH_3OH), and CH_4), C_2 products (C_2H_4 and $\text{C}_2\text{H}_6\text{O}$), and a C_3 product ($\text{C}_3\text{H}_8\text{O}$).^{46,49,50} For instance, HCOOH formation includes the creation of an $^*\text{OCHO}$ intermediate via the activation and reduction of CO_2 .⁵¹ This step requires catalysts with high O affinity, such as p-block metals (e.g., tin [Sn], bismuth [Bi], indium [In], and lead [Pb]), facilitating the reduction of $^*\text{OCHO}$ to form HCOOH .^{52–56}

In contrast, producing CO involves two proton-electron steps that generate a $^*\text{COOH}$ intermediate. Catalysts (e.g., gold [Au], silver [Ag], and zinc [Zn]) known for their lower affinities for O and H reduce $^*\text{COOH}$ to CO .⁴⁶ The selectivity of the overhead product in aqueous CO_2RR can be explained by the ability of various catalyst surfaces to bind reaction intermediates, in which catalyst surface properties play a critical role in determining the reaction pathway and product selectivity (Figure 2C).⁵⁷ Moreover, CO serves as a crucial intermediate for higher hydrocarbons and oxygenates, including formaldehyde (HCHO), CH_3OH ,



and CH₄, involving four, six, and eight electron transfers, respectively.⁴⁶ In addition, CO is widely considered an intermediate for forming C₂H₄ and C₂H₅OH. Table 1 shows the classification of value-added products and significant intermediates.

The formation of these C₂⁺ products involves the dimerization of two CO molecules or the combination of CO with *CHO. Copper (Cu)-based catalysts are effective in these reactions because they facilitate C–C coupling, achieving high selectivity and activity for C₂⁺ products.⁵⁸ In addition, Cu-based materials are among the most promising catalysts for CO₂ reduction because they exhibit relatively low activity toward HER while demonstrating unique intrinsic catalytic activity for CO₂RR, forming a wide range of hydrocarbons, alcohols, and oxygenates. Although the elemental composition of the CO₂RR catalyst is crucial in determining reaction pathways, the overall reaction mechanism is considerably influenced by several factors, including operating conditions, such as electrolyte pH and concentration, cation/anion size, applied potential, cell configuration, and catalyst surface characteristics (e.g., facets, defects, structure, morphology, and surface adsorbates).^{59–62} These physical and chemical parameters strongly influence the thermodynamic adsorption energies of critical intermediates and the kinetic barriers of the reactions, leading to alternative reaction pathways. The following section examines the crucial factors influencing the CO₂RR mechanism in greater detail.

Table 1 Classification of value-added products and significant intermediates.⁶³

	Products	Critical intermediates
Two-electron products	Formate (HCOO ⁻), formic acid (HCOOH) Carbon monoxide (CO)	*OCHO/HCOO* *COOH
Deeply reduced C1 products	Methane (CH ₄) Methanol (CH ₃ OH)	CH ₃ O*, *OH CH ₃ O*, *OH
Multicarbon products	Ethylene (C ₂ H ₄) Acetaldehyde (CH ₃ CHO) Ethanol (C ₂ H ₅ OH) Ethane (C ₂ H ₆) <i>n</i> -Propanol (<i>n</i> -C ₃ H ₇ OH)	CH ₂ CHO* CH ₂ CHO* CH ₂ CHO*, CH ₃ CHO*, CH ₃ CH ₂ O* CH ₃ CH ₂ O* CH ₃ CHO*, CH ₃ CH ₂ O*

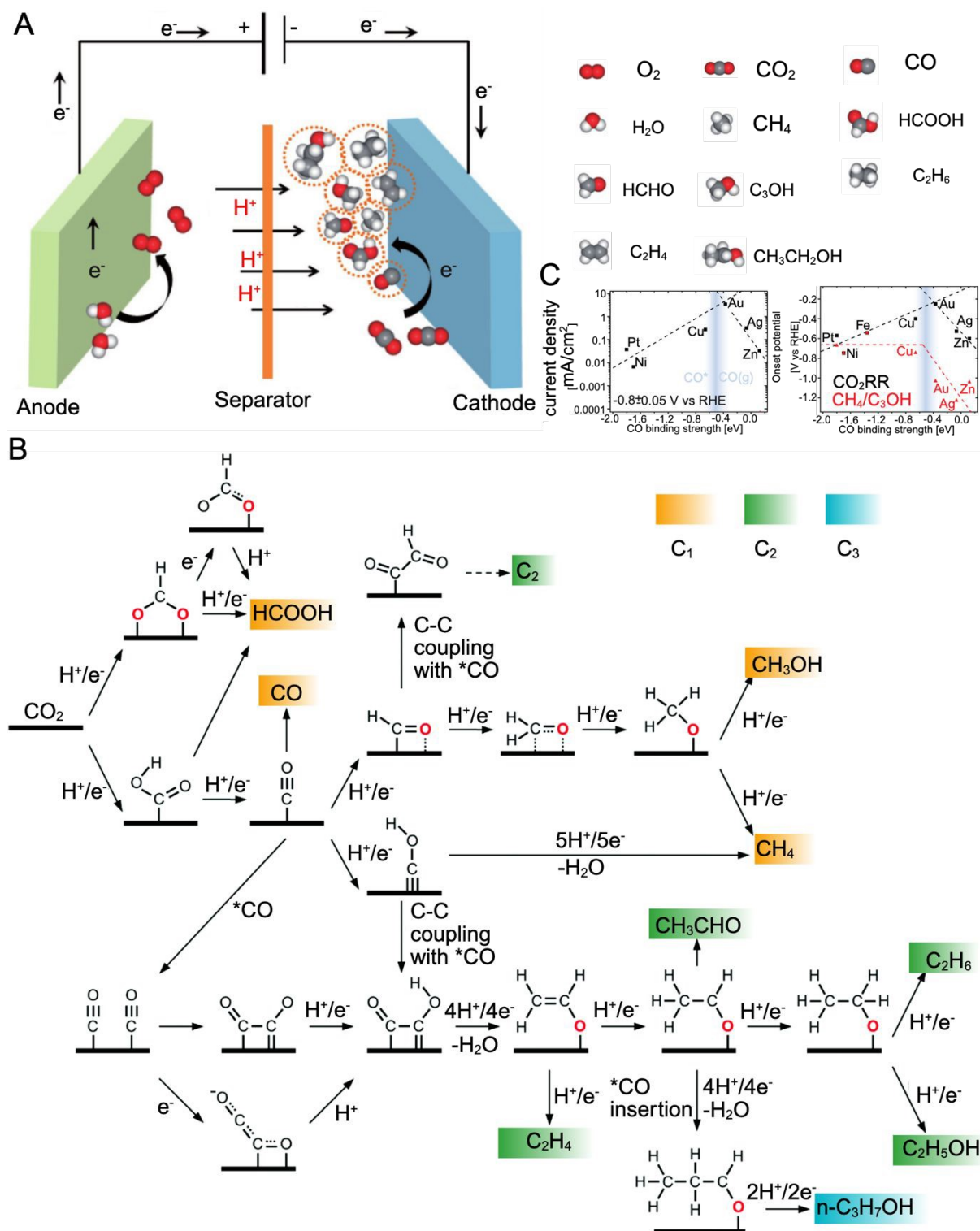


Figure 2. A) Schematic of the electrochemical CO₂ reduction reaction system. “Reproduced from reference [47], with permission from John Wiley and Sons, copyright [2017]”. B) Reaction mechanism, product distribution from CO₂ reduction (C1-C3). “Reproduced from reference [63], with permission from Royal Society of Chemistry, Copyright [2021]”. C) Left: Volcano plot of the partial current density for CO₂RR at 0.8 V vs. the CO binding strength. Right: Two onset potentials plotted vs. CO binding energy, the overall CO₂RR, and the conversion of CO₂ to methane or



methanol (Reprinted with permission from *Am. Chem. Soc.* 2014, 136, 40, 14107–14113. Copyright [2014] American Chemical Society).

2.1 Factors Affecting the CO₂ Electroreduction Process

The efficiency of CO₂RR is governed by the interrelation of internal and external factors in the overall system architecture (Figure 3A). Internal factors include the electrode configuration and electrolyte characteristics, whereas external factors include the applied potential and electrolyzer design. Significant research has been focused on computational modeling and the experimental analysis of the electrode/electrolyte (E/E) interface to clarify electrochemical processes, such as reaction dynamics, product selectivity, and overall electrochemical performance.^{64–66} The E/E interface is influenced by the constant potential during CO₂RR processes, inducing negative surface charges and promoting the formation of the electrical double layer (EDL),^{67–69} as depicted in Figure 3B.

The EDL comprises charged species and oriented dipoles, organized into three distinct layers: the inner Helmholtz plane (IHP), the outer Helmholtz plane, and the diffuse layer.⁶⁸ The IHP is closest to the electrode surface where the electrochemical reaction occurs, whereas cations gather in the outer Helmholtz plane region in response to the applied potential. According to the classical Gouy–Chapman–Stern model, the EDL and bulk electrolytes have a distinctly different composition. Therefore, they are considered two distinct phases separated by the diffuse layer.⁷⁰ Ions form the diffuse layer due to electrostatic repulsion and thermodynamic diffusion. The concentration of the diffuse layer decreases progressively outward toward the bulk electrolyte. In the electrochemical system, the species in the EDL are widely accepted to be in equilibrium with the bulk electrolyte in the absence of any Faradaic processes.⁶⁷

The CO₂RR is an inner-sphere process in the IHP involving adsorption and bond rearrangement of CO₂ and intermediates. When the CO₂ molecule adsorbs onto the electrode surface, it binds through chemisorption, a process involving electron redistribution and chemical bond formation.⁷¹ The CO₂ binding process at the surface is influenced by the highest occupied and lowest unoccupied molecular orbitals. The orientation of



these orbitals relative to the surface determines the nature of the binding. Such a CO₂-binding process on MXenes is expected to be effective due to the tunable surface chemistry. According to the computational investigations, their surface chemistry influences the diffusion and adsorption of species and metal ions on MXene surfaces.⁷² Therefore, understanding the molecular-level interaction between CO₂ and MXene at the E/E interface is crucial to evaluating intermediates' adsorption/desorption process, reaction kinetics, and dynamic behavior, and designing highly active, selective, and durable catalysts.

In one of the earliest studies aimed at understanding the IHP in the EDL, Harris et al.⁷³ multinuclear magnetic resonance experiments were employed to elucidate the strong H-bonded water molecule to the terminal hydroxyl (–OH) group on the MXene surface. This finding significantly contributed to estimating the Gibbs free energy profiles and determining the reaction-limiting potential (U_L) for spontaneous electrochemical reactions.

Later, Cheng et al.⁷⁴ employed the density functional theory (DFT) to model EDL properties and proposed an intermediate electronic structure and reaction pathways of CO₂RR on modified Nb₂CO₂ surfaces while considering the effect of water. The results indicated that pure Nb₂CO₂ is unsuitable as a catalyst for CO₂RR; nonmetal-doped MXene can lower the U_L of CO₂RR and does not significantly change the reaction products. In contrast, MXene surface modification with TMs reduced the U_L of CO₂RR and altered the reaction products. The V-modified Nb₂CO₂ system was identified as the most effective CO₂RR catalyst, favoring HCOOH as the primary product with a U_L of –0.11 V (Figure 4A). The presence of *d*-levels in TMs provides a diverse range of electronic configurations, which can participate in bonding with CO₂ molecules, enhancing the electron transfer processes essential for CO₂RR. The interaction between the *d*-levels of the metal and the π^* orbitals of CO₂ can lead to a more efficient electron transfer, which is crucial for breaking strong C=O bonds in CO₂.^{75,76}

The EDL properties of MXene modified by TMs as single-atom catalysts (SACs) have been extensively explored.^{77–80} Li et al.⁸¹ investigated Mo₃C₂ MXene modified with a series of Group IVB, VB, and VIB



TMs and explored the mechanism behind the breaking of linear scaling relationships between TMs and the adsorption energies of critical intermediates OCH_2O^* and HOCH_2O^* (Figure 4B). Their findings revealed that substituting TMs on the MXene surface induces an upshift in the d-band center of the molybdenum (Mo) layer surface, selectively tuning the adsorption strength of OCH_2O^* and HOCH_2O^* , further lowering U_L from -0.651 V for Mo_3C_2 to -0.350 V for Mo_2TiC_2 (Figure 4C). The electron localization function analysis indicated the strong localization of lone electrons on the surface Mo layer upon TM substitution, enhancing its chemical activity due to electronic coupling between the valence states of adsorbates and the TM states, resulting in splitting the bonding and antibonding states (Figure 4D). In addition, Mo_2TiC_2 demonstrated the highest conversion performance of CO_2 to CH_4 among the studied MXenes.

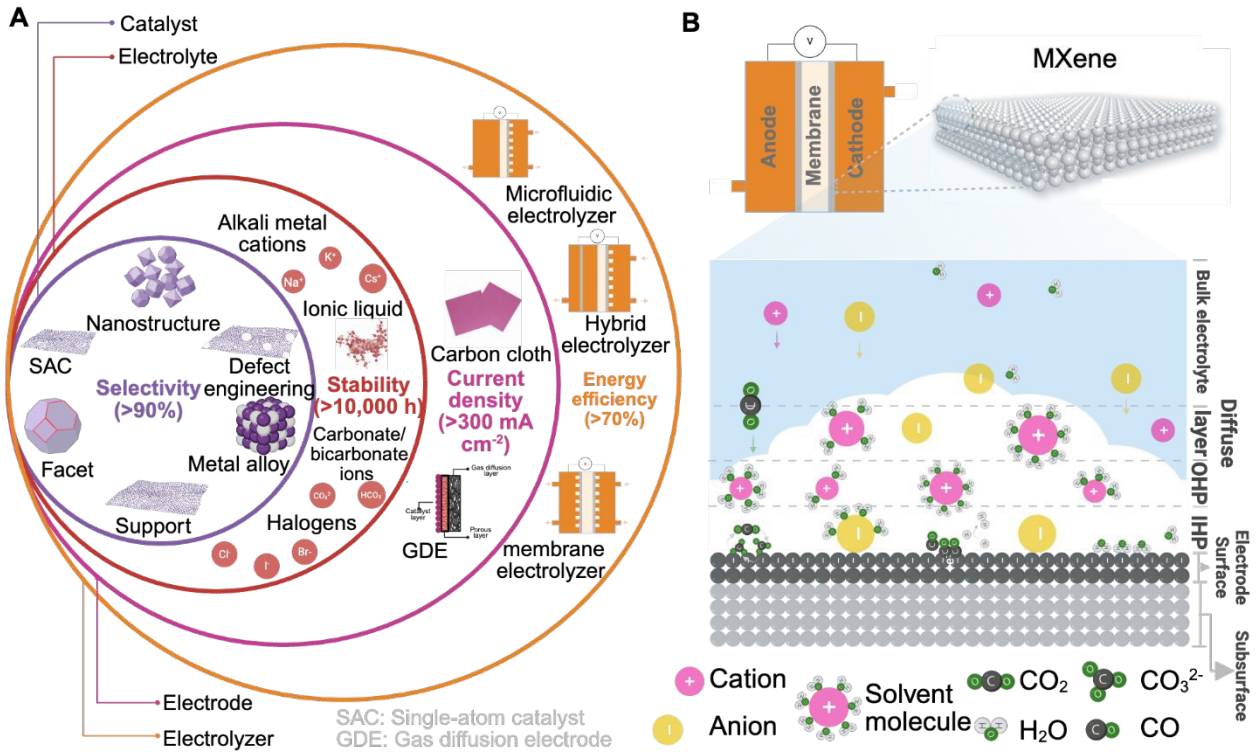


Figure 3. A) Factors affecting the CO_2 electroreduction process. B) Schematic of the electrode-electrolyte interface for CO_2 RR, accounting for the electric double layer and bulk electrolyte.

Although electrode properties play a crucial role, the E/E interface is significantly influenced by the electrolyte medium. Aqueous solutions, organic solvents, and ionic liquids (ILs) can stabilize the solid-

electrolyte interphase, enhance CO₂ solubility, and facilitate efficient ionic transport, all essential for optimizing electrochemical reactions. Among these, aqueous KHCO₃ solutions (0.1 to 0.5 M) are widely employed to evaluate the performance of MXene-based catalysts due to their cost-effectiveness, nontoxicity, and buffering capacity, making them the preferred medium for CO₂RR investigations. A recent experimental study⁸² demonstrated that the performance of Ti₃C₂T_x on a glassy carbon electrode improved for mono- and multicarbon products, achieved selectivity toward CO (42.2%), CH₃OH (23.6%), C₂H₆O (20.1%), and acetone (10.1%) as the KHCO₃ concentration in the electrolyte increased from 0.1 to 0.5 M. The authors attributed this performance to the enhanced CO₂ adsorption capacity of 0.16 mmol g⁻¹, facilitating a higher current density.

Otgonbayar et al.⁸³ demonstrated enhanced selectivity toward alcohols, such as CH₃OH and C₂H₆O, using 2D MXene coupled with cuprous oxide (Cu₂O)/magnetite (Fe₃O₄) nanocomposites using various electrolytes, including sodium carbonate (Na₂CO₃), potassium carbonate (K₂CO₃), potassium chloride (KCl), and sodium chloride (NaCl). A strong interaction between the catalyst surface and the electrolyte, particularly with alkali metals and halide ions (chlorine [Cl⁻]), enabled faster adsorption/desorption dynamics, influencing their ability to donate or retain a negative charge. This interaction generated a dipole moment, modified the local surface environment, and enhanced the catalytic activity.

Qu et al.⁸⁴ demonstrated CO₂ electrolysis using seawater as the cost-effective electrolyte. This strategy achieved 92% Faradaic efficiency (FE) for CO production using synthesized nitrogen (N)-doped Ti₃C₂ MXene nanosheets with abundant V_{Ti} defects. Mechanistic studies have revealed that N dopants and V_{Ti} synergistically modulate the electronic structure of the active titanium (Ti) site, significantly lowering the free energy barriers for *COOH formation and *CO desorption.

Notably, pH is pivotal in influencing aspects of PCET processes in CO₂RR. The local pH at the E/E interface can change during the CO₂RR, significantly affecting the selectivity and activity of the catalyst.^{85,86} For example, Varela et al.⁸⁷ investigated the influence of the electrolyte concentration and the importance of



301 local pH in controlling the selectivity of CO₂RR on Cu. The study demonstrated that the buffer capacity of
302 the electrolyte is critical in influencing catalytic activity and product selectivity. In diluted KHCO₃, the
303 lower proton concentration near the electrode surface suppresses the formation of H₂ and CH₄, whereas the
304 production rates of CO and C₂H₄ remain largely unaffected.

305 Xie et al.⁸⁸ employed lateral-type in situ surface-enhanced Raman spectroscopy combined with
306 computational simulations using COMSOL to investigate the effect of local pH variations at the E/E
307 interface on CO₂RR selectivity and activity (Figure 4E). The study revealed that, in the diffusion layer, the
308 local pH gradually decreases as the distance from the catalyst surface increases, with a sharp pH drop
309 indicating limited proton mass transport (Figure 4F–H). As reported, these local pH variations are influenced
310 by the buffering capacity of the electrolyte and can have a considerable influence on the selectivity of C₂⁺
311 products during CO₂RR (Figure 4I).⁸⁹

312 The pH dependence of CO₂ activation differs from that of the competing HER. For example, previous work
313 has demonstrated that the overall product selectivity of graphite-immobilized coprotoporphyrin is highly
314 pH sensitive. At a pH of 1, H₂ is the dominant product, whereas at a pH of 3, CO becomes the primary
315 product, illustrating the strong influence of pH on reaction pathways.⁹⁰ The DFT calculations indicate that
316 the critical intermediate is anionic hydride, which undergoes a nucleophilic attack on CO₂ to yield HCOO[−]
317 . The reaction is facilitated by potential-induced changes in the oxidation state of the catalyst, with the
318 hydride typically residing on the ligand for In and Sn porphyrins. The stability of the resulting species is
319 vital for reactions leading to CO or HCOOH/HCOO[−] formation.

320 Pourbaix diagrams, analogous to standard pressure–volume phase diagrams, offer insight into the
321 thermodynamic equilibrium surface structure under varying pH and applied potential (*U*) conditions.
322 According to the Pourbaix diagram of MXenes with various surface termination groups (Figure 5),⁹¹
323 MXenes do not exhibit a bare surface at any pH-*U* conditions in an aqueous environment. At a *U* value
324 below −0.6 V, the MXene surface is fully hydrogenated, with all reaction sites occupied by H*. As *U*



325 increases, the surface undergoes progressive oxidation, with OH* gradually replacing H*, highlighting the
326 strong *U* sensitivity of the process. The intricate relationship between *U* and MXene functionalization, as
327 demonstrated for other electrochemical reactions, such as HER⁹² and N reduction reaction,⁹³ is significant
328 because it directly influences catalytic activity. This understanding can guide the design of MXene-based
329 catalysts for CO₂RR, facilitating the selection of optimal surface terminations for enhanced performance.
330 Future studies should develop Pourbaix diagrams for MXene compositions under CO₂RR-relevant pH and
331 *U* conditions, offering deeper insight into their electrochemical stability and reactivity.



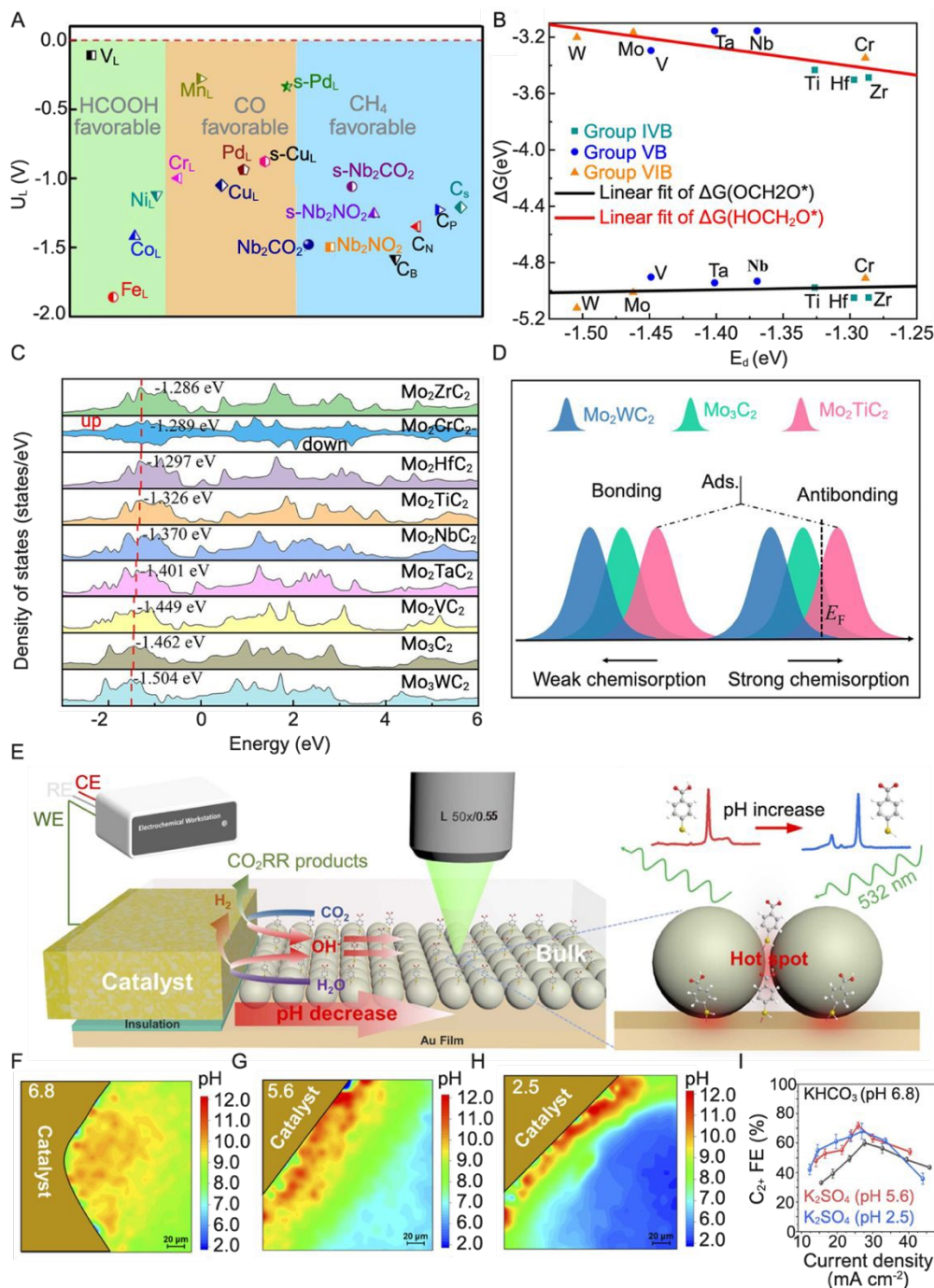


Figure 4. A) Potential limiting UL of NbCO₂ and modified Nb₂CO₂ “Reproduced from reference [74], with permission from Elsevier, Copyright [2021]”. B) Linear relation of adsorption free energy $\Delta G(\text{OCH}_2\text{O}^*)$ and $\Delta G(\text{HOCH}_2\text{O}^*)$ vs. the d-band center E_d . C) Projected density of state plots for the d orbital of surface Mo atoms in MXenes, in which the Fermi level was set to 0, and the calculated d-band centers are denoted by dashed vertical red lines. D) Schematic of the bond formation between the adsorbate (Ads.) and reaction surface of MXenes, represented by Mo₂WC₂, Mo₃C₂, and Mo₂TiC₂. (B-D, “Reproduced from reference [81], with permission from Elsevier, Copyright [2021]” E) Schematic of the L-SERS system for in situ local pH measurement and illustration of pH-sensitive molecules (4-MBA) in the SERS. F–H) Local pH images around the catalyst surface in CO₂-saturated electrolyte of (F) KHCO₃ (pH 6.8), (G) K₂SO₄ (pH 5.6), and (H)

K_2SO_4 (pH 2.5) with the applied current density of 10 mA cm^{-2} , and C_{2+} Faradaic efficiency by pH.
“Reproduced from reference [88] with permission from Elsevier, Copyright [2024]”.

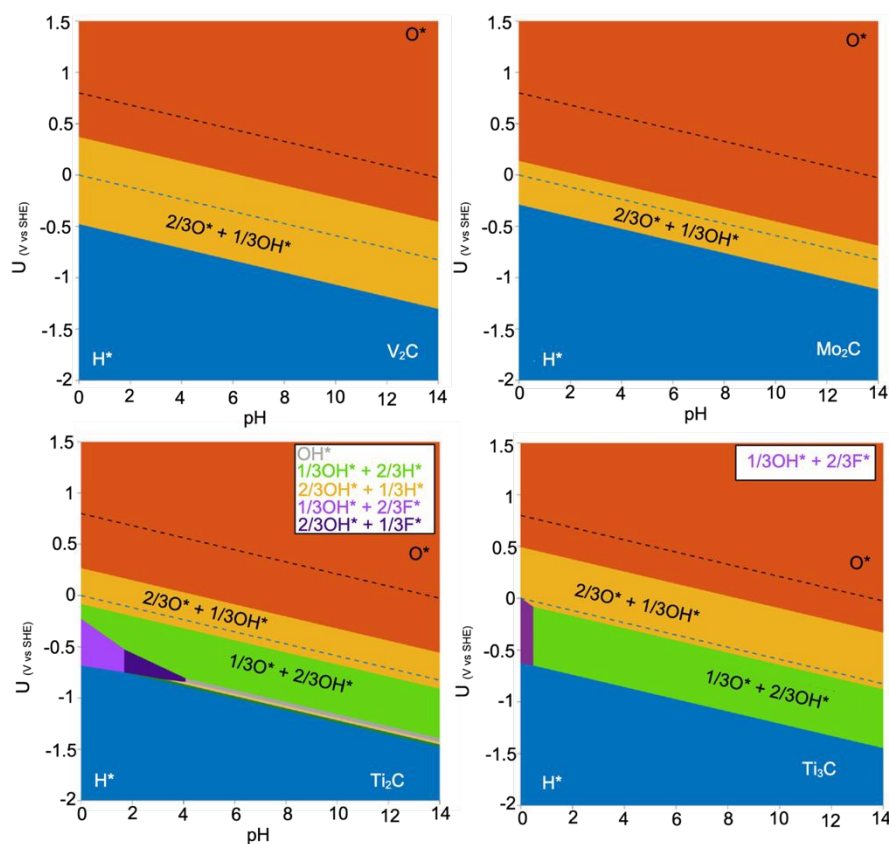


Figure 5. Pourbaix diagrams for Mo_2C , V_2C , Ti_2C , and Ti_3C_2 “Reproduced from reference [91] with permission from Wiley and Sons, Copyright [2022]”.

The electrolyte's metal cation/anion composition is another critical factor influencing the product distribution of CO_2RR . Alkaline-metal cations facilitate CO_2 adsorption in aqueous solutions and stabilize critical intermediates, such as COOH^* , via noncovalent interactions with adsorbed species or a field effect.⁹⁴ For instance, Hori et al.⁹⁵ observed that C_2H_4 formation increased relative to CH_4 as the cation size increased (lithium [Li^+] < sodium [Na^+] < potassium [K^+] < cesium [Cs^+]).⁹⁶ This variation in hydrocarbon selectivity was attributed to differences in specific adsorption or the preferential hydrolysis of various cations. Among anions, halide ions (F^- , Cl^- , bromine [Br^-], and iodine [I^-]) could modulate the geometry and electronic structure of metal-based electrocatalysts, stabilize active species, regulate the adsorption and desorption of



reaction intermediates, and reduce the overpotential to enhance the selectivity and activity of CO₂RR for multicarbon products.^{97–99} This finding is attributed to halide ions donating electrons to the empty orbitals of CO₂.¹⁰⁰

Ni et al.¹⁰¹ synthesized fluorine (F)-doped caged porous C, achieving an FE of 88.3% for CO production at –1.0 V vs. RHE, with a corresponding current density of –37.5 mA·cm^{–2}. The microporous structure of the F-doped C shells, particularly at edge positions, induces localized high electric fields, lowering the thermodynamic energy barrier for CO₂ reduction. Similarly, Gao et al.¹⁰² demonstrated that O₂-plasma-activated Cu catalysts, combined with electrolyte design, exhibited enhanced CO₂RR activity and selectivity toward multicarbon hydrocarbons and alcohols, achieving a FE of ~69% and a partial current density of –45.5 mA cm^{–2} for C₂₊ products at –1.0 V vs. RHE. Their findings indicated that larger alkali-metal cations and subsurface O species promoted cation adsorption, facilitating C–C coupling on CuO_x electrodes. Furthermore, using an electrolyte containing Cs⁺ and I[–] induced a significant reorganization of the CuO_x surface, forming well-defined Cu species, and enhanced the intermediate stabilization and C₂⁺ product selectivity.

Considering the well-documented positive influence of halide ions on CO₂RR performance, MXenes, with abundant halide surface terminations, present a promising platform for enhancing the selectivity of multicarbon products. Halogen-based etching using molecular Cl, Br, or I can introduce halide terminations onto MXene surfaces, potentially modulating active species and regulating the adsorption–desorption dynamics of reaction intermediates during CO₂RR.^{103–105} For instance, a Cu-immobilized Ti₃C₂Cl_x MXene demonstrated over 58% selectivity for CH₃OH, with dominant Cl functional groups residing on the outermost Ti layers.¹⁰⁶ Synchrotron-based x-ray absorption spectroscopy and DFT calculations attributed the exceptional performance of the catalyst to single-atom Cu species with an unsaturated electronic structure (Cu^{δ+}, 0 < δ < 2), facilitating a low-energy-barrier conversion from HCOOH* to the CHO* intermediate.



However, despite confirming the abundant Cl terminations, the study did not explicitly address their role in the activity and selectivity of the catalyst. Given the widely accepted understanding that halide ions influence reaction mechanisms by modulating intermediate adsorption and desorption, further investigation of the Cu-immobilized $\text{Ti}_3\text{C}_2\text{Cl}_x$ catalyst is necessary to clarify the role of Cl termination groups. Future research should systematically explore the effects of $-\text{Cl}$, $-\text{Br}$, $-\text{F}$, and $-\text{I}$ terminations on MXene-based catalysts, offering deeper insight into their influence on CO_2RR performance and product distribution.

The electrolyte employed during CO_2RR can also influence product distribution and overall performance. Despite being the most applied electrolyte systems in CO_2RR , aqueous solutions have limited CO_2 solubility (about 0.034 M), constraining their application in the H-cell. Research efforts have been directed toward using dipolar aprotic solvents, such as acetonitrile (about 0.27 M)¹⁰⁷ and ILs, which can serve as mediators that prevent HER and as cocatalysts that form complexes with CO_2 molecules to overcome this problem and improve CO_2 solubility. In one of the earliest studies on MXene using ILs, Handoko et al.¹⁰⁸ combined experimental and theoretical approaches to investigate Ti- and Mo-based MXenes for HCOOH production, achieving a 56% FE in an electrolyte system containing IL 3-butyl-1-methyl-1H-imidazol-3-ium tetrafluoroborate dissolved in an acetonitrile–water solution. This work highlighted the crucial role of $-\text{O}$ surface termination groups in suppressing HER while revealing the limitations of acetonitrile as an electrolyte due to its volatility, causing fluctuations in HCOOH selectivity.

Attanayake et al.¹⁰⁹ suppressed the competing HER using IL 1-ethyl-2-methylimidazolium tetrafluoroborate as an electrolyte in acetonitrile. Under these conditions, Ti_3C_2 and Mo_2C demonstrated a remarkable FE of 90% for CO production. Despite the favorable solubility of CO_2 in ILs, their relatively high viscosity compared to conventional solvents poses challenges, including a lower CO_2 adsorption rate and increased pumping costs in industrial applications. Cosolvents, such as water or CH_3OH , can be introduced to reduce viscosity while maintaining CO_2 solubility to mitigate viscosity-related limitations.¹¹⁰



403 Previous studies on energy storage devices have demonstrated strong synergy between surface terminations
404 of MXenes and IL functional groups, significantly influencing supercapacitor performance.^{111–114} Applying
405 insight from MXene-IL interactions in energy storage devices to CO₂RR could enhance interfacial
406 interactions, improving product selectivity and addressing stability challenges. This approach presents a
407 promising strategy for applying the complementary properties of MXenes and ILs to enable efficient and
408 scalable CO₂ conversion into a diverse range of valuable products.

409 The catalyst structure can also affect the activity and selectivity of CO₂RR. A Cu-based catalyst is highly
410 capable of producing multicarbon products. However, selectivity toward a specific product is challenging.
411 Nanostructured Cu, including nanoparticles, nanowires, and hierarchical structures with varying
412 compositions, sizes, morphologies, and crystal orientations, has gained considerable research attention due
413 to its ability to enhance the selectivity of CO₂RR.^{115,116} The exposed crystal facets of the nanostructured Cu
414 play a crucial role in determining the reaction pathway and controlling product distribution. Adjusting the
415 exposed facet on the Cu crystals can change the specific atom arrangements, reaction intermediate affinity,
416 and surface energy, influencing the CO₂RR pathway and product distribution.¹¹⁷

417 Luo et al.¹¹⁸ investigated the facet-dependent selectivity of Cu₂O nanocrystals, demonstrating that tailoring
418 the exposed facets enhanced selectivity toward C₂H₄. Star-shaped Cu₂O nanocrystals with (332) facets
419 achieved over 74% selectivity for C₂H₄. This high selectivity was attributed to a reduction in Gibbs free
420 energy, with the (332) facets exhibiting the lowest energy barrier (0.13 eV) in the initial step of gaseous
421 CO₂ hydrogenation, compared to (111) at 0.20 eV and (100) at 0.22 eV. Furthermore, the in situ Raman
422 spectroscopy of star-shaped Cu₂O (332) nanocrystals revealed the presence of *COOH and *CHO
423 intermediates, indicative of C–C coupling, facilitating C₂H₄ formation.

424 The nanocrystal structure influences the facet dependence of the selectivity of Cu nanocrystals in CO₂RR.
425 An investigation of Cu single crystals in an H-cell has revealed that (100) is suitable for C₂H₄ formation,
426 whereas (111) favors CH₄ formation. For example, Gregorio et al.¹¹⁹ develop a colloidal method to



synthesize Cu cubes, spheres, and octahedra nanocrystals and tested them for CO₂RR in flow cells. The study revealed that the Cu octahedra nanocrystals dominantly produced CH₄, in line with the presence of the exposed (111) facets. In contrast, the Cu cubes with dominant (100) facets exhibited much higher selectivity (55%) toward C₂H₄. These studies demonstrated the facet-structure dependence of the selectivity of Cu-based nanocrystals. The influence of external factors, such as temperature and applied voltage (constant and pulse/dynamic), remains underexplored in optimizing MXene performance for CO₂RR. Most studies have focused on ambient temperature conditions,¹²⁰ either via DFT predictions or experimental investigations, aiming to maintain temperature as a constant parameter to ensure catalyst stability and durability. Conversely, the applied potential is a dynamic factor essential for activating the catalyst surface and forming an E/E interface. Changes in applied voltage alter the charge density on the MXene surface, affecting the organization of ions and solvent molecules in the EDL, and affecting CO₂ adsorption and intermediate stabilization. Moreover, potential variations can modify the oxidation state of the catalyst, changing its electronic structure and overall surface properties and influencing reaction pathways and product selectivity.

For example, Han et al.¹²¹ used an in situ x-ray analysis to monitor changes in Sn species' oxidation states and local chemical environment in SnO₂/MXene catalyst under various applied potentials ranging from −0.6 to −1.2 V vs. RHE. The authors observed a gradual shift toward lower energy on Sn K-edge x-ray absorption near-edge structure (XANES) profiles with a more negative applied potential. They reported a progressive reduction in the oxidation valence state under CO₂RR. The excellent performance and selectivity of CO₂RR to HCOOH in a 0.1 M KHCO₃ aqueous solution reached a maximum of 94% at −0.8 V, attributed to the intermediate/mixed Sn oxidation state between metallic Sn⁰ and Sn⁴⁺.

Furthermore, Govindan et al.¹²² highlighted the influence of the applied potential on MXene-based catalysts, where tuning the cell potential enabled a palladium (Pd)-MXene nanocomposite to achieve a FE of 67.8% for CH₃OH at −0.5 V vs. RHE. Moreover, CO and H₂ became the dominant products at higher potentials, attributed to CO serving as a crucial intermediate in CH₃OH formation. However, as the potential increased,



CO desorption from the catalyst surface intensified, restricting its further conversion to CH₃OH and shifting the selectivity toward CO and H₂ evolution. This observation highlights the vital role of the applied potential in determining product selectivity and reaction pathways. However, despite its importance, no studies have investigated using a pulsed potential for MXene in CO₂RR, highlighting a notable research gap for future investigation.

The system configuration is a critical factor in determining the overall catalytic performance of MXene-based electrocatalysts in the CO₂RR. This configuration encompasses electrode type (e.g., carbon paper, glassy carbon, and gas diffusion electrodes) and reactor design (e.g., H-cells, microfluidic cells, and membrane electrode assemblies, MEAs). Each component plays a distinct role in controlling mass transport behavior, product selectivity, energy efficiency, and scalability. (Figure 6).

While H-cells are the most widely used reactors for fundamental CO₂RR studies, they frequently underrepresent real-world performance due to low CO₂ solubility (~33 mM), mass transport limitations, and high ohmic resistance from large inter-electrode spacing (>2 cm). As a result, H-cells typically achieve modest current densities (<50 mA cm⁻²) and produce Faradaic efficiencies that are difficult to reproduce under industrial conditions^{123,124}. In contrast, flow-cell reactors, particularly those employing gas diffusion electrodes (GDEs), directly expose the catalyst to a continuous CO₂ gas stream, dramatically improving CO₂ mass transport and achieving reliable partial current densities between 50–300 mA cm⁻². For instance, a SnO₂ quantum dot/MXene composite attained 57.8 mA cm⁻² with 94% Faradaic efficiency for formate in a flow-cell GDE/MEA configuration, significantly outperforming H-cell benchmark. Similarly, an FePc/MXene composite tested in a flow cell demonstrated ~98% FE for CO with stability over 24 h, highlighting improved mass transport and HER suppression compared to the H-cell configuration¹²⁵.

MEA-based reactors integrate solid-state ion-exchange membranes, enabling compact reactor designs, ion-specific transport control, and minimal reactant/product crossover. A Bi₂O₃/MXene composite demonstrated continuous operation at 300 mA cm⁻² with >90% formate selectivity over 60 h in an MEA¹²⁶.



Abdinejad et al. evaluated a Cu–Pd/MXene composite catalyst using both configurations. In an H-cell, the catalyst achieved a CO₂-to-formate conversion with a FE of 79% at –0.5 V vs. RHE. In contrast, when tested in a zero-gap MEA reactor, the same catalyst achieved an enhanced FE of 93% at –2.8 V and a full-cell energy efficiency of 47%, showcasing the MEA's ability to sustain higher current densities and reduce resistance.¹²⁷ These comparisons underscore that while H-cells are valuable for mechanistic insights, they are limited in reflecting the behavior of MXene catalysts under realistic, high-throughput conditions. MEAs offer enhanced gas transport, stable interfaces, and minimized side reactions, allowing MXenes to achieve higher selectivity, greater stability, and industrially relevant current densities. This reinforces the need to assess MXene catalysts under MEA configurations to realize and report their catalytic potential. Table 2 shows comparison of MXene catalyst performance across different reactor configurations.

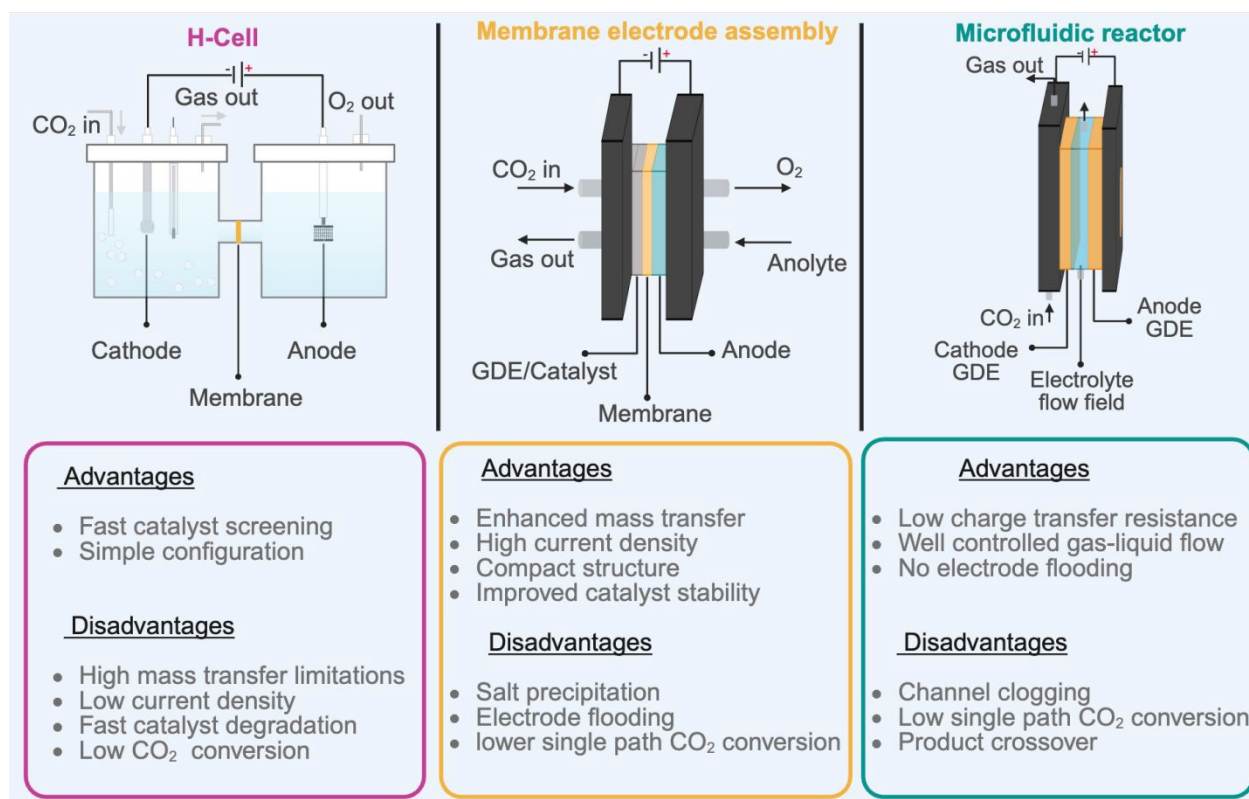


Figure 6. Schematic of the typical electrochemical flow cells for CO₂ reduction.



Table 2. Comparative performance of MXene-based electrocatalysts in H-cell, flow-cell, and MEA configurations, showing the same material under different reactor designs, associated current densities, product selectivities, and literature references.

MXene catalyst	Cell configuration	Current Density (mA cm ⁻²)	Product & FE (%)	Ref.
Au/Ti ₃ C ₂ T _x MXene	H-cell	17.3	CO (48.3%), H ₂ (25.6%)	128
Cu–Pd/MXene aerogel	H-cell	~20	Formate (~79%)	127
Cu–Pd/MXene aerogel	MEA	150	Formate (>90%)	127
FePc/MXene composite	Flow-cell	>100–200+	CO (~98%) stable	125
FePc/MXene composite	MEA	200+	CO (~98%), 96% stability	125
Pd–Ti ₃ C ₂ T _x MXene	H-cell	~10–20	CO (~48%), H ₂ (~26%)	122
SnO ₂ QD / MXene composite	H-cell	<30	Formate (<70%)	121
SnO ₂ QD / MXene composite	Flow-cell	57.8	Formate (~94%)	121

3. MXene Fabrication, Structure, and Characteristics

3.1 MAX Phase Synthesis and Etching

The MAX phase is a layered carbide, nitride, or carbonitride with the formula M_nAX_n. The A layers (group of 11 to 16 elements) are weakly bonded to the M layers via metallic bonds, making them selectively etchable, whereas strong covalent bonds hold together the M and X layers. Figure 7A presents the chemical composition of MAX phase precursors and their MXene derivatives. Since MXene was first discovered, over 150 MAX phases have been predicted via computational investigations.¹²⁹ The diversity of MAX phases is presented through the possible MAX chemical compositions and the ability to form various *n* structures, including MAX precursors (M₂AX, M₃AX₂, M₄AX₃, and M₅AX₄)¹³⁰. Recently, out-of-plan (M₂M'AX₂ and M₂M'₂AC₃) and in-plan (e.g., (M_{2/3}M'_{1/3})₂AlC) ordered structure MXenes have been reported.¹³¹

The MAX phases are synthesized at elevated temperatures (800°C to 1,800°C) in an inert atmosphere. The process involves mixing elemental powders (M and A) or carbide/nitride mixtures, followed by sintering. The precursor selection, stoichiometry, and heating rate strongly influence the properties and purity of the MAX phase. Since the discovery of MXene, extensive research has focused on optimizing MAX phase synthesis, refining etching protocols, and improving delamination methods. The addition of excess Ti and

aluminum (Al) beyond the stoichiometric ratio during the reactive sintering of Ti_3AlC_2 enhances the stability and conductivity of the resulting MXene.^{132,133} This improvement is attributed to the excess Al, which reacts with O in the system, promoting the formation of more stoichiometric Ti_3AlC_2 with fewer defects, including O substitution in the C sublattice.

Recently, Michałowski et al.¹³⁴ employed atomic-resolution ultralow-energy secondary-ion mass spectrometry to detect O incorporation in the C sublattice. The study revealed that when a stoichiometric Ti:Al:C ratio is used, Ti_3AlC_2 can contain up to 30% O in the C sublattice, forming an oxycarbide MXene upon etching. In contrast, using excess metals in synthesis led to Ti_3AlC_2 with no detectable O. Excessive A-layer content during the MAX phase synthesis reduces O substitution and C vacancies, improving MXene stability and electronic properties.¹³² Similarly, the composition of X in the MAX phase can influence MXene properties.

For example, Shuck et al.¹³⁵ used three C sources, graphite, TiC, and C lampblack, to synthesize the MAX phase. The produced MXene exhibited distinct stability and conductivity depending on the composition and morphology. Therefore, choosing elemental precursors, mixing ratios, and sintering conditions is crucial to achieving desirable MAX phase characteristics for CO_2RR applications. Future research should explore the influence of these factors, particularly the M, A, and X compositions, on the electrocatalytic performance of MXenes.

MXene synthesis involves the removal of the A layer from the MAX phase to form multilayered MXene, with the reaction's Gibbs free energy determining the etching effectiveness. This approach is called the top-down approach for MXene synthesis (Figure 7B). MXenes produced using this approach come in M_2XT_x , $\text{M}_3\text{X}_2\text{T}_x$, $\text{M}_4\text{X}_3\text{T}_x$, and $\text{M}_5\text{X}_4\text{T}_x$ forms (Figure 7C). Naguib et al.¹³⁶ synthesized the first MXene by etching Ti_3AlC_2 with concentrated hydrofluoric acid (HF), selectively weakening Ti–Al bonds while preserving Ti–C bonds. During etching, the initial adsorption of H and F atoms onto Ti atoms selectively weakens the less stable Ti–Al bonds, leaving the stronger Ti–C bonds intact. This process creates interlayer spacing,



532 facilitating the intercalation of HF and H₂O for sequential layer-by-layer etching.¹³⁷ This process exposed
533 undercoordinated Ti metallic surfaces, which were saturated with termination groups, such as –O, –OH, and
534 –F, denoted as T_x .^{138,139} Since the first reported synthesis of MXene, significant efforts have been directed
535 toward optimizing synthesis protocols and minimizing the use of hazardous HF. Therefore, numerous
536 alternative methods have been developed, including low HF etching, electrochemical, alkaline, molten salt,
537 and halogen etching approaches.

538 Low concentrations or reduced quantities of HF yield high-quality MXenes with fewer defects. Acid
539 mixtures have been explored as alternative etching solutions to minimize HF usage while maintaining
540 efficient MAX-phase etching. For example, a comparative study evaluated HF/HCl and HF/H₂SO₄ etching
541 systems to remove the Al layer from Ti₃AlC₂ and reported that MXene synthesized via HF/HCl displayed
542 larger interlayer spacing and higher structural water compared to HF and HF/H₂SO₄, which might be due to
543 the –Cl termination.¹⁴⁰ Recently, an optimized HCl:HF:H₂O etching solution has gained widespread
544 adoption due to its reduced HF content and ability to produce high-quality MXene sheets. This approach
545 uses a 6:1:3 ratio of HCl, HF, and H₂O per gram of MAX powder.¹⁴¹

546 Shuck et al.¹⁴² applied the HCl:HF:H₂O etching method for the scalable synthesis of up to 50 g of Ti₃C₂T_x
547 MXene (Figure 7D). Notably, the large-batch synthesized MXene exhibited identical structural and
548 chemical characteristics to small-batch samples, demonstrating that this approach enables scaling up without
549 compromising material quality (Figure 7E), making it a promising route for commercialization.



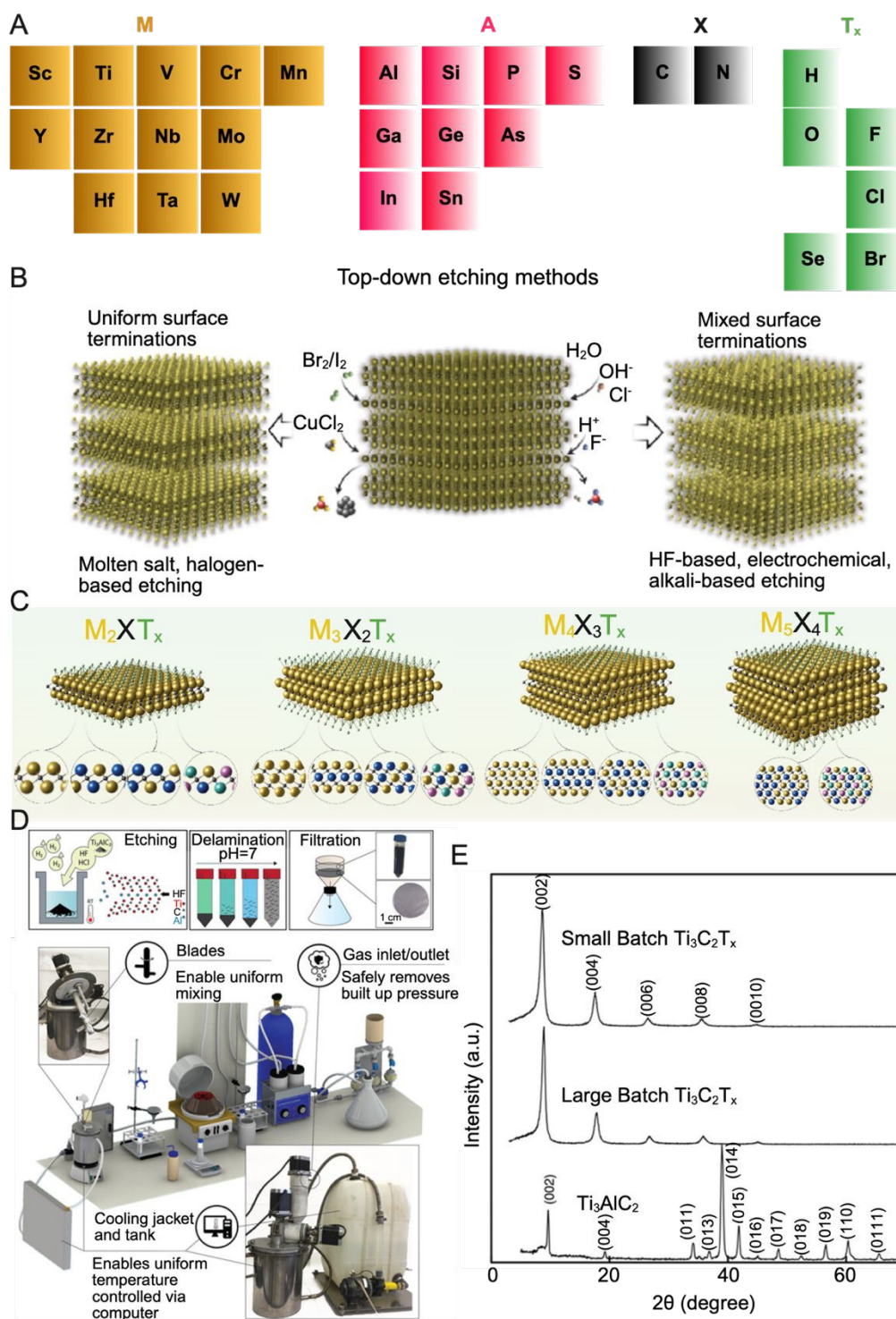


Figure 7. A) Periodic tables presenting MAX phase and MXenes compositions. B) Top-down etching methods for MXene synthesis. C) MXene forms synthesized using top-down etching methods (B and C, “Reproduced from reference [143] with permission from Springer Nature, Copyright [2025]”. D) Schematic demonstrating the large-scale synthesis of MXene using the HCl:HF:H₂O etching method. E) X-ray diffraction pattern of MXene synthesized via a large-scale process and a small batch. No notable change in structure is observed. (D and E, “Reproduced from reference [142] with permission from Wiley and Sons, Copyright [2020]”.



557

558 In a three-electrode configuration, the electrochemical etching method selectively removes the A atomic
559 layer by applying a potential while using the MAX phase as an electrode. The applied potential disrupts the
560 M–A bond using electrolyte solutions, such as NaCl, HCl, or HF.¹⁴⁴ Effective control over the etching
561 potential and time ensures selective A atom removal, enabling precise control over MXene synthesis. An
562 uncontrollable increase in the applied potential can eliminate the M-layer, yielding amorphous C
563 materials.^{145,146}

564 Chen et al.¹⁴⁷ synthesized $\text{Ti}_3\text{C}_2\text{T}_x$ via electrochemical etching in a mixed lithium hydroxide (LiOH) and
565 lithium chloride (LiCl) aqueous solution, achieving over 90% etching efficiency. The synthesis was
566 performed at 5.5 V for 5 h, using two identical Ti_3AlC_2 blocks as symmetric electrodes. As the etching
567 progressed, the Ti_3AlC_2 cathode remained intact, whereas the Ti_3AlC_2 anode was partially consumed. The
568 presence of Li^+ ions in the etching solution facilitated the etching process by intercalating into the layers
569 and promoting the delamination of MXene with $-\text{Cl}$ surface termination.

570 Similarly, Shen et al.¹⁴⁸ prepared an F-free $\text{Ti}_3\text{C}_2\text{Cl}_2$ MXene using a molten-salt-assisted electrochemical
571 etching technique. During the electrochemical etching process, the surface termination was modified from
572 $-\text{Cl}$ to $-\text{O}$ and sulfur ($-\text{S}$), considerably shortening the modification steps and enriching the variety of
573 surface terminations.

574 Electrochemical etching is a green and safe synthesis method with low energy consumption. However,
575 challenges remain, including forming an amorphous C layer under uncontrolled etching conditions and the
576 relatively low yield of MXene. Although the MAX phase electrode can be reused multiple times, the typical
577 etching process results in limited MXene production, making it unsuitable for large-scale synthesis. Despite
578 these limitations, this approach can potentially prepare MXene for CO_2RR .



Alkaline etching is a nonacid etching method for synthesizing MXene with functional groups, such as $-\text{OH}$ and $-\text{O}$, making it hydrophilic and suitable for fabricating electrodes for aqueous applications, such as CO_2RR . Despite the limited toxicity of this method, MXene synthesis using this approach is challenging because the reaction is spontaneous at elevated temperatures, making it difficult to control oxidation at elevated temperatures and low concentrations. The fast oxidation is attributed to $-\text{OH}$ termination groups that oxidize MXene quickly.

For example, Li et al.¹⁴⁹ successfully prepared $\text{Ti}_3\text{C}_2(\text{OH})_2$ MXenes using KOH in a hydrothermal reactor. Replacing the Al atoms with $-\text{OH}$ groups allows the formation of 2D $\text{Ti}_3\text{C}_2(\text{OH})_2$. Similarly, NaOH -assisted hydrothermal alkali etching at 270°C yielded $\text{Ti}_3\text{C}_2\text{T}_x$ with a yield of 92% and improved interlayer spacing.¹⁵⁰ The primary reaction pathway involves converting Al into $\text{Al}(\text{oxide})$ hydroxides, followed by their dissolution in an alkaline medium. Elevated reaction temperatures and concentrated NaOH facilitate the rapid dissolution of $\text{Al}(\text{oxide})$ hydroxides, forming F-free MXene with abundant $-\text{OH}$ and $-\text{O}$ surface terminations. The abundant $-\text{OH}$ terminations on MXenes synthesized using this method may enhance C_2 product formation.

Literature reports indicate that the presence of $-\text{OH}$ terminations on Cu catalysts can lower the binding energy of CO and improve the charge equilibrium between C atoms in the adsorbed OCCO intermediate. This interaction reduces the energy barrier for C_2H_4 formation by facilitating CO dimerization.^{151–153}

Molten salt etching can be divided into fluoride-containing and fluoride-free molten salt etching.¹⁵⁴ The fluoride-containing approach allows the in situ formation of HF during synthesis. By combining a strong acid (e.g., HCl or H_2SO_4) and fluoride salts (e.g., LiF , NaF , KF , NH_4F , and FeF_3) or using bifluoride salt (e.g., NH_4HF_2 , NaHF_2 , and KHF_2), HF can be formed in situ during the etching process^{154,155}. During synthesis, metal cations (Li^+ , Na^+ , and K^+) enter negatively charged MXene layers and increase interlayer spacing, eliminating the need for an extra intercalation step. The etching temperature and concentration of the acid and fluoride salt can significantly affect the quality of MXene sheets.



Wang et al.¹⁵⁶ reported on the synthesis of a MXene with an accordion-like structure by introducing LiF into a NaCl–KCl molten salt etchant with CuCl₂. The reaction was kept for 5 h at 750°C, and monolayer flakes of MXene nanosheets were synthesized by incorporating the prepared MXene into a tetrabutylammonium hydroxide (TBAOH) solution during agitation, achieving a MXene yield of ≈15% to 20%.

The Lewis acidic molten salt etching approach is proposed to prepare fluoride-free MXenes by adjusting MAX precursors with various Lewis acid salts under elevated temperatures. For example, Li et al.¹⁵⁷ used an element replacement approach that replaces the A-layer atom in the MAX phase with Zn atoms in a molten ZnCl₂. This approach synthesizes and etches several MAX phases, including Ti₃ZnC₂, Ti₂ZnC, Ti₂ZnN, and V₂ZnC, to achieve their respective MXene derivatives. The MXene synthesis was achieved by MXene Al-MAX with ZnCl₂ in a 1:6 molar ratio and heating at 550°C for 5 h to achieve pure Cl-terminated MXene sheets.

Li et al.¹⁰⁵ expanded this approach using Lewis acidic etching to synthesize MXenes from the MAX phase precursors containing A elements, such as Si, Zn, and gallium (Ga; Figure 8A). As illustrated in Figure 8B, this approach can prepare MXene with other types of A-layer atoms. By tuning the chemistry of the MAX precursor and the composition of the Lewis acid melt, a direct redox interaction between the A element and the cation of the Lewis acid molten salt enables the prediction of MAX phase reactivity in the molten salt, facilitating MXene synthesis. For instance, Ti₃SiC₂ was immersed in molten CuCl₂ at 750°C. During the reaction, the exposed Si atoms, which are weakly bonded to Ti in the Ti₃C₂ sublayers, were oxidized to silicon (Si⁴⁺) cations using Lewis acid Cu²⁺, forming volatile SiCl₄ and the concomitant reduction of Cu²⁺ to metallic Cu. The metallic Cu was removed by immersing the Ti₃C₂Cl₂ product in an ammonium persulfate solution. High-resolution scanning transmission electron microscopy (STEM) revealed that the resulting MXene exhibited a lamellar microstructure similar to that of MXene synthesized using the HF etching approach (Figure 8C). Considering the high activity of Cu for CO₂RR, this research should optimize this approach to preserve Cu metallic particles in the resulting MXene structure and test it for CO₂RR.



Kamysbayev et al.¹⁵⁸ employed substitution and elimination reactions in molten organic salts to synthesize MXenes with varied surface termination groups using CdCl₂ or CdBr₂ molten salts (Figure 8D). The study demonstrated that Cl- or Br-terminated MXenes can actively participate in surface reactions, where halide ion exchange enables precise control over the surface chemistry and properties of MXene sheets. The surface terminations of the synthesized MXenes were further modified by dispersing them in molten alkali-metal halides, such as Li₂Te, Li₂S, Li₂Se, Li₂O, and NaNH₂ (Figure 8E), allowing for tailored functionalization and enhanced material properties.

Recently, Liu et al.¹⁵⁹ prepared a Ti₃C₂T_x (Tx: Cl- and O-) via a molten-salt-etching route in acetonitrile-based electrolyte. Moreover, CuCl₂ was applied as the main molten salt etching, and NaCl/KCl was employed as a supporting electrolyte. The synthesis was performed at 680°C for 24 h in an argon (Ar)-filled furnace. The obtained MXene displayed enhanced electrochemical stability.

The literature has reported several new top-down MXene synthesis approaches, including hydrothermal-assisted HCl etching¹⁶⁰ and microwave-assisted molten salt etching.^{161–163} These development methods are still in their early stages and require more investigation to optimize them to produce high-quality MXenes.

Most studies on MXene synthesis are based on a top-down approach. Three bottom-up synthesis approaches, chemical vapor deposition (CVD), the template method, and plasma-enhanced pulsed laser deposition, have been reported for synthesizing MXene. The CVD method allows the growth of ultrathin MXene sheets at elevated temperatures and a nonterminated surface.

Xu et al.¹⁶⁴ produced defect-free molybdenum carbide (Mo₂C), tungsten carbide (WC), and tantalum carbide (TaC) thin films using CVD at elevated temperatures (1085°C). Recently, Wang et al.,¹⁶⁵ synthesized Ti₂CCl₂ using CVD. The reaction of CH₄ and TiCl₄ on a Ti surface enables direct CVD growth at 950°C of Ti₂CCl₂ carpets and complex spherulite-like morphologies that form via buckling and the release of the MXene carpet to expose a fresh surface for further reactions (Figure 8F). Scanning electron microscopy imaging revealed that the synthesized MXene evolved from bulges into spherical MXene vesicles



(Figure 8G) with sheets radiating from the center and oriented normally to the surface (Figure 8H). The template method uses 2D TM oxide (TMO) nanosheets as templates. During the synthesis, the TMO nanosheets are carbonized or nitrified to form carbide or nitride MXene, respectively.¹⁶⁶

For example, Xiao et al.¹⁶⁷ produced molybdenum nitride (MoN) using 2D molybdenum trioxide (MoO₃) nanosheets as templates. The MoN was synthesized by annealing the MoO₃ cover with NaCl at 280°C for 2 h. The MoN exhibited very uniform nanosheets with a thickness of about 0.71 nm. The 2D tungsten nitride and vanadium nitride nanosheets were also synthesized using this method. Plasma-enhanced CVD and pulse laser deposition can be combined to prepare 2D MXenes.

Zhang et al.¹⁶⁸ prepared an ultrathin large-area Mo₂C films on sapphire by combining plasma-enhanced CVD and pulse laser deposition. The sapphire substrate was heated to 700°C for depositing high-quality Mo₂C film using CH₄ plasma as the C source.

In a recent study, Xiang et al.¹⁶⁹ reported a scalable gas-phase technology for synthesizing Cl-terminated Ti₂CCl₂. The synthesis was conducted in a fluidized CVD reactor bed, where TiCl₃ was introduced into the reactor at 770°C and was rapidly sublimated to form a gaseous precursor for nucleation (Figure 8I). The gaseous precursors were transported by Ar gas to react with CH₄ in the upper region of the fluidized reactor bed, forming TiCCl₂ powders. The process yielded about 0.1 kg per batch, underscoring the high efficiency of the synthesis method. X-ray diffraction (Figure 8J) and atomically resolved high-angle annular dark-field (HAADF)-STEM images (Figure 8K) revealed the typical characteristics of Ti₂CCl₂.



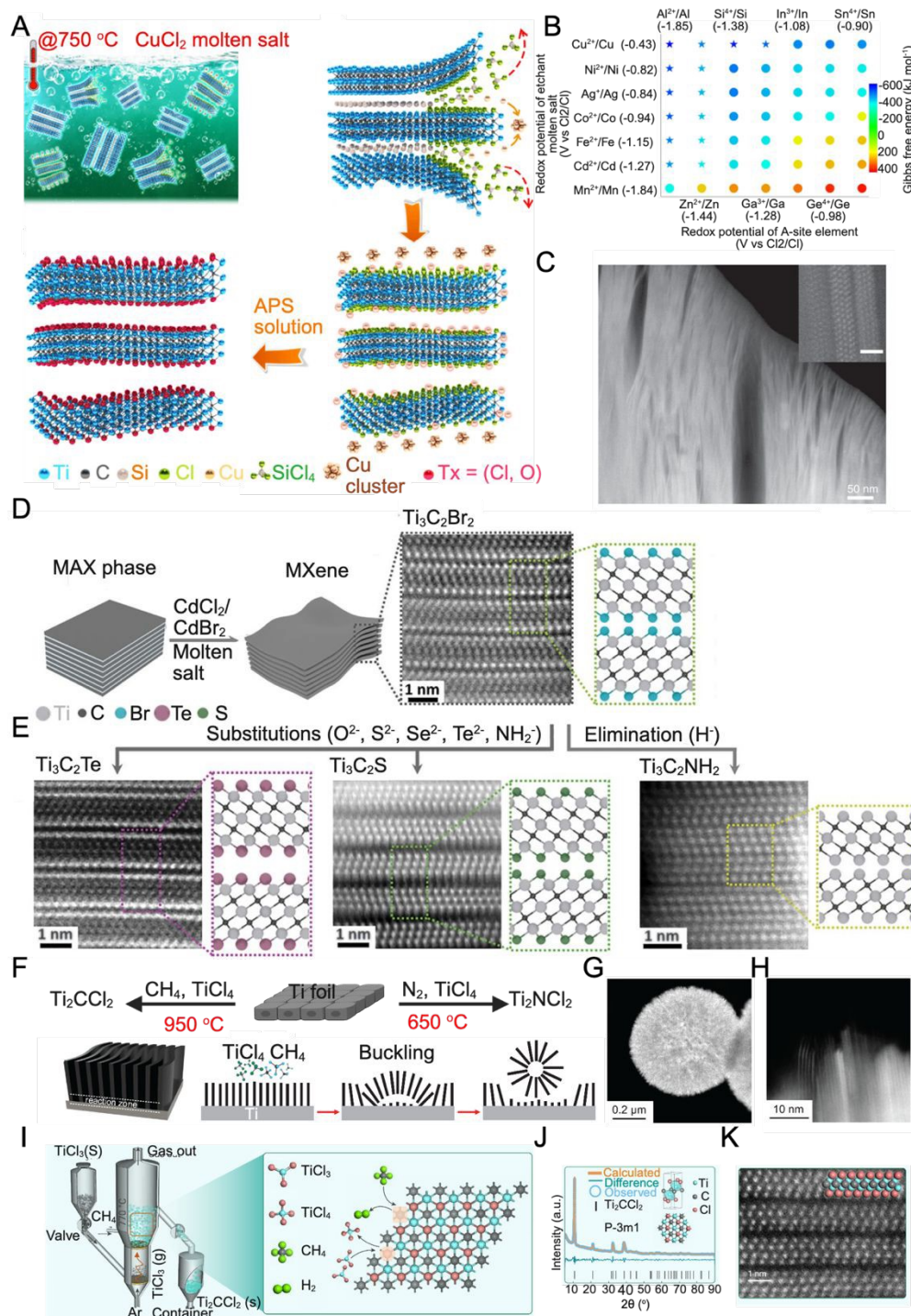


Figure 8. A) Schematic of $\text{Ti}_3\text{C}_2\text{Cl}_2$ synthesis via the Lewis acid etching route. B) Gibbs free energy mapping (700 °C) guiding the selection of Lewis acid Cl salts based on the electrochemical redox potential. C) High-resolution transmission electron microscopy imaging of MXene (A-C, “Reproduced from reference [170] with permission from Springer Nature, Copyright [2020]”). D) Etching MAX phases in Lewis acidic molten salts and atomic-resolution high-angle annular dark-field (HAADF) image of $\text{Ti}_3\text{C}_2\text{Br}_2$. E) HAADF images of $\text{Ti}_3\text{C}_2\text{Te}$, $\text{Ti}_3\text{C}_2\text{S}$, and $\text{Ti}_3\text{C}_2\text{NH}_2$ MXenes (B and E, “Reproduced from reference [158] with permission from American Association for the Advancement of Science, Copyright [2020]”). F) Schematic of the reaction zone and proposed mechanisms of CVD- Ti_2CCl_2 . G) Micrograph of a Ti_2CCl_2 crystal. H) High-resolution TEM image of Ti_2CCl_2 . I) Schematic of the CVD- Ti_2CCl_2 synthesis. J) Calculated difference intensity of Ti_2CCl_2 . K) High-resolution TEM image of Ti_2CCl_2 .



Scanning transmission electron microscopy (STEM) images of spherical MXene. H) High-resolution image spherical MXene (F-H, “Reproduced from reference [165] with permission from American Association for the Advancement of Science, copyright [2023]”. I) Schematic of fluidized reactor bed for CVD process. J) X-ray diffraction pattern for Ti_2CCl_2 obtained using FBR-CVD before delamination. K) Cross-sectional HAADF-STEM image of the (0001) plane of Ti_2CCl_2 flake (I-K, “Reproduced from reference [169] with permission from Elsevier, Copyright [2024]”.

3.1.1 Intercalation and Delamination

Top-down approaches for MXene synthesis typically yield multilayer MXenes, requiring intercalation and delamination to obtain monolayer MXene sheets, which have enhanced physical and chemical properties compared to their multilayer counterparts. Due to strong interlayer interactions in multilayer MXene, the insertion of organic molecules or inorganic ions can weaken these interactions and increase interlayer spacing, facilitating delamination.¹⁷¹ Common organic intercalants include dimethyl sulfoxide (DMSO), N-methyl-2-pyrrolidone, tetramethylammonium hydroxide (TMAOH), TBAOH, hydrazine monohydrate, N,N-dimethylformamide, and urea, whereas LiCl is widely used as an inorganic intercalant.¹⁷²

Following the initial discovery of MXene in 2011, Mashtalir et al.¹⁷³ demonstrated in 2013 that multilayer MXene could be delaminated into monolayer MXene nanosheets via DMSO intercalation. After delamination, the x-ray diffraction analysis revealed that the interlayer spacing of $\text{Ti}_3\text{C}_2\text{T}_x$ MXene increased from 1.95 to 3.50 nm, reducing van der Waals interactions and promoting exfoliation via ultrasonication. Delamination into monolayer MXene increases surface terminations and enhances hydrophilicity and the negatively charged surface of MXene nanosheets, facilitating their dispersion and the formation of stable colloidal solutions. Although DMSO has promising results as an intercalation molecule for $\text{Ti}_3\text{C}_2\text{T}_x$, it is not effective for delaminating other MXene types.

Hydrazine monohydrate, N,N-dimethylformamide, and urea have been explored as intercalation agents to exfoliate multilayer $\text{Ti}_3\text{C}_2\text{T}_x$ into monolayer $\text{Ti}_3\text{C}_2\text{T}_x$ MXene.¹⁷³ However, these methods have demonstrated limited efficiency due to the aggregation of monolayers, resulting in thicker flakes (20 to 50 nm). Naguib et al.¹⁷⁴ demonstrated that TBAOH, hydroxyl choline, and n-butylamine could facilitate the delamination of V_2C_x and Ti_3CNT_x from their multilayered structures into single layers via simple



handshaking in water. Following intercalation and delamination, the interlayer spacing increased from 2.14 to 3.86 nm for Ti_3CNT_x and from 1.99 to 3.86 nm for $\text{V}_2\text{C}\square_x$. The similarity in interlayer spacing for both MXenes highlights the crucial role of intercalating molecules in determining the final interlayer spacing of delaminated MXenes.

Han et al.¹⁷⁵ demonstrated that hydrothermal-assisted intercalation of TMAOH can efficiently intercalate multilayer $\text{Ti}_3\text{C}_2\text{T}_x$, increasing the monolayer $\text{Ti}_3\text{C}_2\text{T}_x$ MXene yield to over 73% while achieving a thickness of 1.7 nm. The hydrothermal-assisted intercalation process facilitates diffusing and incorporating TMAOH between layers. Ascorbic acid was introduced as a mild reductant to prevent the oxidation of MXene at elevated temperatures.

With the continuous expansion of the 2D MXene family, alternative delamination solvents have been explored for various MXene compositions. Montazeri et al.¹⁷⁶ applied NaOH to intercalate Na^+ ions into $\text{Nb}_2\text{C}\square_x$ and $\text{Mo}_2\text{Ti}_2\text{C}_3\text{T}_x$ multilayers following a washing step with TBAOH. The resulting delaminated MXenes exhibited increased d-spacing values of 1.6 and 1.5 nm for $\text{Nb}_2\text{C}\square_x$ and $\text{Mo}_2\text{Ti}_2\text{C}_3\text{T}_x$, respectively. In addition to assisting with delamination, NaOH also reduced the surface oxidation of the flakes. Similarly, Mashtalir et al.¹⁷⁷ reported on an amine-assisted delamination of Nb_2C MXene, where the intercalation of isopropylamine between the $\text{Nb}_2\text{C}\square_x$ layers followed by mild sonication in water for 18 h at room temperature led to successful exfoliation. An x-ray diffraction analysis of the delaminated $\text{Nb}_2\text{C}\square_x$ revealed an increased interlayer spacing of 1.23 nm, which is sufficiently large to accommodate more than one isopropylamine molecule and water between layers.

In addition, LiCl can be employed as an intercalator for multilayer MXenes to enlarge their interlayer spacing by inserting Li^+ .¹⁴¹ Zhang et al.¹⁷⁸ applied LiCl as an etchant to delaminate $\text{Ti}_3\text{C}_2\text{Cl}_2$, synthesized via Lewis acid molten salt etching. A primary challenge associated with Lewis acid molten salt etching is the difficulty of achieving monolayer nanosheets due to the hydrophobic nature and strong interlayer interactions of halogen-terminated MXenes. Delamination was accomplished using a LiCl-assisted DMSO



intercalation approach, where the sample was treated for 24 h followed by centrifugation. As $\text{Ti}_3\text{C}_2\text{Cl}_2$ is hydrophobic, hydrated cations struggle to intercalate between layers. The experiment was conducted in a moisture-free environment to avoid forming a hydration shell around Li^+ , which could hinder intercalation.¹⁷⁹

Notably, the HCl/LiF molten salt etching approach eliminates the need for additional intercalation because MXenes synthesized via this method can be directly delaminated. This result is attributed to the spontaneous insertion of Li^+ into interlayers, expanding and weakening interlayer interactions, facilitating separation into monolayers via ultrasonication or simple shaking by hand.¹⁸⁰

Song et al.¹⁸¹ proposed a freeze-sonication delamination strategy for exfoliating multilayer MXene into monolayer MXene with a yield exceeding 74%. This approach applies the synergistic effect of ultrasonic treatment and ionic intercalation, facilitating the penetration of numerous water molecules into the interlayer space. The volume expansion, followed by ultrasonic treatment in a frozen state, forms monolayer MXene. The delaminated MXene demonstrated an excellent gravimetric capacitance of 261.1 F/g and satisfactory cycling stability. Many of the reported delamination approaches produce MXene with smaller flakes, limiting their application for large MXene flakes.

3.1.2 Scalability and Defects Minimization

Large-scale synthesis of various MXenes, beyond the commonly reported Ti_3C_2 , is essential to broaden their practical use in catalytic applications such as CO_2 reduction. Conventional top-down synthesis methods, particularly HF-based etching (including HF, $\text{HCl/HF/H}_2\text{O}$, and LiF/HCl mixtures), are widely adopted for MXene production due to their simplicity and relatively high throughput. However, these approaches suffer from significant limitations when applied to large-batch synthesis. Challenges include the toxicity of etchants, poor control over surface terminations (typically resulting in F-rich terminations), and considerable variability in flake morphology and chemistry, including thickness, lateral dimensions, and termination groups, all of which adversely impact catalytic performance and batch-to-batch



reproducibility^{182,183}. Alternative etching techniques have emerged, including low-HF protocols, electrochemical etching, alkaline (e.g., NaOH/KOH) etching, molten salt, and halogen-based etching. Each offers different trade-offs regarding yield, safety, termination control, and structural preservation¹⁸⁴. For instance, molten salt etching provides better control over surface terminations (e.g., –Cl, –O) without hazardous liquid acids, though it requires high temperatures (>600 °C)¹⁸⁴. Electrochemical etching in flow reactors enables tunable, fluoride-free synthesis under ambient pressure, but is limited by relatively low yields and the risk of defect formation from overpotential exposure¹⁸². These methods are summarized in Table 3, which compares key parameters including scalability, termination control, industrial suitability, and limitations.

Table 3. Comparative Overview of Top-Down MXene Synthesis Methods.

Method	Scalability and Throughput	Termination Control	Advantages	Industrial Suitability	Key Limitations
HF Etching ¹³⁹	High (tens of grams per batch)	Poor (–F dominated)	Simple, fast, widely adopted	Mature, used in academic and lab-scale work	Highly toxic; uncontrolled terminations; defect formation
HCl–HF–H ₂ O / LiF–HCl ^{105,142}	Moderate (~5–15 g per batch)	Moderate (mixed –F/–OH)	Safer than pure HF; better delamination via Li ⁺	Feasible at lab and pilot scale (~50 g)	Involves fluoride; sensitive to processing parameters
Electrochemical Etching ¹⁴⁷	Low (batch); Moderate (flow reactors: ~10 g/hr)	High (tunable –O, –Cl)	Fluoride-free; selective and tunable; potential-controlled	Promising for industrial translation	Lower yield; possible defect formation; scaling challenges
Alkaline Etching ^{149,150}	Moderate (gram-scale hydrothermal setups)	Good (–O, –OH rich)	Fluoride-free; environmentally benign; improved hydrophilicity	Feasible for specific MAX phases	Limited to few MAX phases; low efficiency
Molten Salt Etching ^{159,184}	Moderate to High (up to tens of grams per run)	Moderate (–Cl, –O, –S possible)	Fluoride-free; high crystallinity; controlled terminations	Pilot studies reported	Requires >600 °C; substrate dependent
Halogen Etching ^{158,169}	Moderate–High (~0.1 kg per batch via CVD or halide vapor route)	Tunable (–Cl, –Br, –I)	Unique terminations; dry etching; scalable in CVD setups	Emerging technique	Toxic gases; process maturity is low



As MXene synthesis scales toward industrial production, reducing structural defects and chemical impurities becomes vital for preserving material performance and enabling application-specific functionality¹⁴². Several complementary strategies have been proposed to mitigate these challenges throughout the synthesis workflow. Continuous-flow etching systems offer more homogeneous reaction environments than static batch processing, ensuring consistent exposure of MAX phases to etchants and minimizing local concentration gradients that can induce uneven etching¹⁸⁵. This leads to improved uniformity in layer thickness and flake size^{142,185}. Additionally, precursor engineering, such as stoichiometric optimization of MAX phases with slight excesses of Ti or Al, can suppress intrinsic carbon vacancies and oxygen substitutions that degrade the final MXene quality^{132,135}. The choice of etching media significantly affects structural integrity and termination control. Mixed-acid systems, such as the commonly used 6:1:3 HCl:HF:H₂O ratio, offer safer and more reproducible etching than pure HF, reducing structural collapse and enhancing monolayer yield¹⁸⁶. Shuck et al. demonstrated that this protocol could be scaled to synthesize up to 50 g of Ti₃C₂T_x MXene per batch, while maintaining flake morphology and surface chemistry similar to those obtained in small-scale syntheses^{143,187}. Among the emerging approaches, soft delamination has shown significant promise^{188,189}. This method eliminates ultrasonication, shaking, or centrifugation while separating MXene sheets. Instead, the intercalated MXene mixture is left undisturbed for ~30 minutes, allowing gravity-assisted flake separation and the formation of a dark colloidal suspension. Although this method tends to yield more bi- and tri-layered flakes and is relatively slow, it produces large, low-defect flakes ideal for catalytic applications where surface integrity is critical^{188,189}.

Finally, storage and environmental stability must be considered, as freshly synthesized MXenes are highly susceptible to oxidation and hydrolysis when exposed to air or moisture. Best practices include storing MXenes under inert atmospheres (e.g., Ar or N₂), applying freeze-drying techniques to avoid hydrolysis, or using protective encapsulation (e.g., polymer or carbon coatings) to retain surface activity before electrochemical deployment^{190,191}. Collectively, these defect-mitigation strategies, spanning reactor design,



etchant optimization, purification, delamination, and post-synthesis stabilization, are critical for producing high-quality, scalable MXenes suitable for industrial CO₂RR and other energy applications.

3.2 MXene Properties

MXenes possess a unique combination of physicochemical properties, making them promising materials for CO₂RR. Their compositional diversity, derived from various transition metals (M), carbon or nitrogen X layers, and surface terminations, grants them exceptional tunability of electronic structure,¹⁸⁶ metallic electronic conductivity,¹⁷¹ and mechanical robustness.¹⁹² Pristine MXenes such as Ti₃C₂ are metallic, with reported conductivities as high as 24,000 S cm⁻¹,^{171,193,194} which facilitates rapid electron transfer kinetics critical for electrocatalysis¹⁴³. Their surface termination groups (e.g., -O, -OH, -F, -Cl) play a central role in modulating reactivity by stabilizing key intermediates (*COOH, *HCOO) and adjusting binding energies, thereby influencing product selectivity. These terminations also impart hydrophilic behavior¹⁹⁵, enhance electrolyte accessibility, and affect mechanical properties, such as Young's modulus, which ranges from ~0.33 to 0.50 TPa depending on surface chemistry, synthesis route, and defect density^{196,197}. MXenes also demonstrate thermal stability under inert conditions (up to ≥500 °C)¹⁹⁸ and are structurally robust in acid electrolytes or under electrochemical cycling when surface terminations are well controlled. However, their susceptibility to oxidation and hydrolysis under ambient or aqueous environments is a well-documented challenge. Therefore, maintaining MXene stability during CO₂RR requires appropriate synthesis methods, surface passivation, and environmental controls. Several studies have explored strategies to mitigate this degradation, demonstrating long-term cycling stability and preserved morphology in a controlled environment. For example, Xie et al.¹⁹⁹ performed a comprehensive DFT analysis showing that Ti₂C and Ti₃C₂ MXenes retain their structural integrity and electronic conductivity during multivalent ion intercalation. Their findings support that MXenes can exhibit structural and electrochemical stability under conditions relevant to energy storage, provided that surface terminations and operating environments are carefully controlled. Also, Ghidui et al.¹⁵⁴ demonstrated long-term electrochemical stability of Ti₃C₂T_x synthesized via a LiF-HCl route, maintaining performance over thousands of cycles in 1 M H₂SO₄. This



suggests that MXenes can exhibit high structural stability under specific aqueous electrochemical conditions. In contrast, Cao et al.¹⁹⁰ highlighted degradation pathways and proposed mitigation strategies including i) defect-controlled synthesis, ii) post-treatment (e.g., annealing or reduction), iii) encapsulation with carbon or polymer coatings, and iv) controlled storage in inert, low-moisture conditions. Soomro et al. further reported that low-temperature, deoxygenated storage extended the stability of aqueous $\text{Ti}_3\text{C}_2\text{T}_x$ dispersions up to 60 days²⁰⁰. Post-treatment techniques such as thermal annealing under inert gas or chemical functionalization can be employed to remove labile terminations or introduce more stable groups, thereby improving MXene's catalytic performance. Ultimately, the catalytic behavior of MXenes for CO_2RR depends not only on their inherent properties but also on how they are processed and stabilized. Post-reaction and operando characterization (e.g., XPS, XRD, Raman, and XAS) will be crucial to track structural evolution and guide the rational design of durable, selective MXene-based electrocatalysts. Despite their known advantages, current understanding of MXenes in CO_2RR remains largely based on computational studies. Experimental efforts are urgently needed to validate theoretical predictions, tune surface chemistry, enhance electrode–electrolyte interactions, and achieve long-term stability and selectivity under realistic reaction conditions.

4. Effect of Surface Chemistry

The surface chemistry of MXenes plays a pivotal role in governing CO_2 adsorption behavior, stabilization of key reaction intermediates, and product selectivity during electrochemical reduction. Computational investigations, especially density functional theory (DFT) studies, have demonstrated that specific surface terminations, such as $-\text{O}$ and $-\text{OH}$, significantly lower the Gibbs free energy barriers for the formation of intermediates like $^*\text{COOH}$ and $^*\text{HCOO}$, thereby favoring the production of CO and formic acid (HCOOH). In contrast, $-\text{F}$ terminations typically exhibit weak binding with $^*\text{CO}_2$ and $^*\text{CO}$, leading to reduced catalytic activity but may promote $^*\text{CHO}$ intermediate formation, thereby shifting selectivity toward CH_3OH or CH_4 under specific conditions. More recently, halogen terminations (e.g., $-\text{Cl}$), introduced via molten salt or halogen etching, have been shown to alter surface charge distribution and electronic structure, potentially



influencing intermediate adsorption and desorption dynamics. However, their direct influence on CO₂RR performance remains insufficiently explored and warrants further study.

DFT calculations further indicate that CO₂ interacts with MXene surfaces via physisorption, driven by noncovalent interactions, or chemisorption, involving covalent bonds with surface metal sites. The computed Gibbs free energy (ΔG) for chemisorption varies substantially depending on the MXene composition, ranging from -3.19 to -1.29 eV, as summarized in Table 4. These energetic variations, combined with the electronic effects introduced by different surface terminations, underscore the importance of functional group engineering in tuning MXene-based catalyst activity and selectivity toward targeted CO₂RR.^{120,201} These energetic variations and the electronic effects introduced by different surface terminations underscore the critical importance of tailoring MXene functional groups to direct specific CO₂RR pathways. Table 5 compares the effects of MXene surface terminations on CO₂RR intermediates and product selectivity.

Table 4. Gibbs free energy of reaction (in eV) for CO₂RR intermediates calculated from the density functional theory²⁰²

Species/M ₃ C ₂	Group IV			Group V			Group VI		
	Ti ₃ C ₂	Zr ₃ C ₂	Hf ₃ C ₂	V ₃ C ₂	Nb ₃ C ₂	Ta ₃ C ₂	Cr ₃ C ₂	Mo ₃ C ₂	
*CO ₂	-0.59	0.17	0.18	0.29	0.35		0.25	0.15	
**CO ₂	-3.01	-3.19	-3.05	-1.47	-1.60	-2.30	-1.29	-2.11	
**OCHO	-2.04	-2.25	-2.89	-1.40	-1.71	-1.58	-1.61	-1.74	
**HOCO	-2.06	-2.49	-2.79	-1.41	-1.54	-1.92	-1.74	-1.91	
**OCH ₂ O	-3.51	-4.08	-4.31	-1.93	-2.22	-2.86	-1.60	-1.64	
**HCOOH	-1.01	-2.19	-2.47	-0.15	-0.12	-0.32	0.01	-0.78	
**CO	-1.18	-1.11	-1.54	-1.45	-1.39	-1.80	-2.00	-2.27	
**HOCH ₂ O	-2.47	-2.82	-3.11	-1.59	-1.88	-2.56	-1.85	-2.15	
**HOCH ₂ OH	-1.09	-1.07	-3.56	-0.61	-0.68	-1.10	-0.69	-0.90	
**H ₂ CO	-2.43	-3.21	-3.31	-1.81	-2.16	-2.39	-1.78	-1.86	
**C ₂ OH	-1.58	-2.05	-1.89	-1.26	-1.36	-1.94	-1.51	-1.64	
**CH ₃ O	-2.93	-3.12	-3.33	-2.20	-2.36	-2.98	-2.12	-2.53	
**CH ₂	-1.81	-1.88	-1.21	-0.97	-1.47	-2.33	-1.65	-2.11	
**CH ₃ OH	0.06	0.07	0.01	0.33	0.08	0.22	0.33	0.17	
**O	-4.80	-5.24	-5.23	-3.45	-3.95	-4.27	-3.53	-3.57	
**CH ₃	-2.04	-2.37	-2.86	-2.26	-2.47	-3.27	-2.52	-2.98	
**OH	-4.59	-4.65	-4.80	-3.70	-3.90	-4.35	-3.73	-3.91	
**CH ₄	-1.18	-0.70	-0.94	-2.15	-0.77	-0.82	-0.55	-0.70	
**H ₂ O	-3.03	-2.96	-3.04	-2.46	-2.37	-2.64	-2.55	-2.88	



Table 5. Effects of MXene Surface Terminations on CO₂RR Pathways and Intermediates.

Termination	Representative MXene	Key Intermediaries	Favored Product(s)	Mechanistic Insight
–O ^{203,204}	Ti ₃ C ₂ O ₂ , Ti ₂ CO ₂	*COOH, *HCOO	CO, HCOOH	Strong binding of O-bound species; promotes proton-coupled electron transfer
–OH ^{120,205,206}	Ti ₃ C ₂ (OH) ₂	*COOH	CO	Increases local proton availability; improves surface hydrophilicity
–F ^{207–210}	Ti ₃ C ₂ F _x	*CHO, weak *CO ₂	CH ₃ OH, CH ₄ (low rate)	Weakens CO ₂ adsorption; shifts path to *CHO; often lowers activity
–Cl ²⁰⁹	Ti ₃ C ₂ Cl ₂	Not fully studied; charge effects	(Under study)	Alters electronic distribution; stabilizes some adsorbates; promising but immature.

Among TM-based MXenes, Group IV (e.g., Ti₃C₂, Zr₃C₂, and Hf₃C₂) exhibits a stronger binding affinity for CO₂ compared to Group V (e.g., V₂C and Nb₂C) or VI (e.g., Mo₃C₂ and Cr₃C₂).¹²⁰ This trend can be attributed to the TM atoms' electronic configuration and d-band center, influencing the overlap between metal orbitals and CO₂ antibonding orbitals.^{202,211,212} For example, Mo₃C₂ and Cr₃C₂ MXenes preferentially interact with CO₂ over H₂O, making them highly promising for CO₂RR in aqueous environments. The mechanistic pathway for CH₄ formation on Mo₃C₂ involves successive hydrogenation steps of intermediates, such as OCHO*, •OCH₂O*, and HOCH₂O*, yielding CH₃O* and CH₄ as products (Figure 9A). The DFT calculations suggest that CH₃O* is thermodynamically favored over H₂COH* during the fifth H⁺/e[–] addition, directing the reaction away from CH₃OH and toward CH₄ formation.

Moreover, M₂C MXenes, such as V₂C and Cr₂C, have demonstrated potential for HCOOH production, as evidenced by a volcano-type relationship between the adsorption strength and catalytic activity (Figure 9B). This relationship suggests that intermediate adsorption strengths facilitate efficient CO₂-to-HCOOH conversion. Excessively strong adsorption impedes intermediate desorption, whereas weak adsorption hinders activation, demonstrating the critical role of adsorption energy in catalytic performance.^{121,213–215}

The surface functionalization of MXenes significantly enhances their catalytic performance by modifying electronic properties, adsorption energies, and reaction pathways.^{216,217} Oxygen-terminated MXenes (e.g., Ti₂CO₂ and V₂CO₂) are effective for CO₂RR because the pathway to *HCOOH is preferred over the *CO pathway due to the stabilizing effect of –O groups on reaction intermediates (Figure 9C).²¹¹ Oxygen

vacancies, forming during the reaction, further improve selectivity by stabilizing transition states and creating active sites for intermediate binding. For instance, O-terminated MXenes have been reported to preferentially catalyze CO_2 to HCOOH with reduced overpotentials, applying the accessibility of H-coordinated mechanisms over C-coordinated pathways.²¹⁸ In addition, $\text{Sc}_2\text{Cl}(\text{OH})_2$ and $\text{Y}_2\text{C}(\text{OH})_2$ are promising candidates for CH_4 production due to the reactive H atom in the $-\text{OH}$ group. This reactive H atom facilitates stable intermediate formation, lowering overpotentials and enhancing selectivity for CH_4 formation.²⁰⁵ Fluoride-containing terminations influence product pathways differently. Further, Ti_3C_2 MXenes with $-\text{F}$ terminations tend to favor a path involving formaldehyde intermediates, forming CH_3OH . In contrast, $-\text{F}$ -free MXenes follow a distinct mechanism, producing HCOOH and methylene glycol, decomposing into CH_3OH and water.²¹⁹

Sun et al.²²⁰ used the DFT to evaluate the activity and selectivity of a dual-atom-modified MXene catalyst for CO_2RR to $\text{C}_2\text{H}_6\text{O}$. They demonstrated that the Co–Co dual-atom catalyst, with its asymmetric C–C coupling mechanism, achieves high catalytic activity due to its moderate d-band center, optimally balancing electron occupancy in antibonding orbitals, ensuring efficient adsorption of reaction intermediates. The d-band analysis revealed that vanadium (V)–V and chromium (Cr)–Cr dual-atom catalysts, characterized by higher d-band centers, exhibit stronger adsorption of intermediates ($^*\text{CH}_3\text{CH}_2\text{O}$ and $^*\text{CH}_2\text{OHCH}_2\text{O}$), making hydrogenation steps energetically demanding, with energy barriers of 0.81 and 0.93 eV, respectively (Figure 9D). In contrast, manganese (Mn)–Mn, iron (Fe)–Fe, and cobalt (Co)–Co dual-atom catalysts have d-band centers positioned farther from the Fermi level (Figure 9E), allowing antibonding orbitals to be more readily occupied by electrons. This positioning weakens the adsorption of intermediates (Figure 9F), facilitating smoother reaction pathways without excessive energy barriers and increasing chemical reactivity.²²¹

Table 6 presents innovative MXene-based electrocatalysts, their electrocatalytic activities, working electrolytes, performance, and CO_2RR products, further driving innovation in MXene-based electrocatalysts toward CO_2RR .



899 **Table 6.** Summary of CO₂RR results using MXene-based electrocatalysts.

Electrocatalyst	Potential	Current density (mA/ cm ²)	Electrolyte	Faradaic efficiency (%)	Prod.	Ref.
Pd-MXene	0.5 V;	17	CO ₂ -saturated 1.0 M KHCO ₃	67.8	CH ₃ OH	122
SA-Cu-MXene	−1.4 V vs. RHE	−21.3	0.1 M KHCO ₃	59.1	CH ₃ OH	106
CdS/Ti ₃ C ₂	−1.0 V _{RHE}	~6.4	0.1 M KHCO ₃	94	CO	222
VS-CdS/Ti ₃ C ₂	−1.0 V _{RHE}	~−6	0.1 M KHCO ₃	96	CO	
M _x O _y /MAX hybrid	−0.4 to −0.6 V	2.4	0.5 M NaHCO ₃	67	CO	223
Ag–ZnO/Ti ₃ C ₂ T _x	−0.87 V _{RHE}	22.5	0.5 M KHCO ₃	98	CO	224
d-Ti ₃ C ₂ T _x	−2.2 V vs. SCE	−1.5	Acetonitrile, 1 ethyl-3 methylimidazolium tetrafluoroborate EMIMBF4	65	CO	108
d-Mo ₂ CT _x	−2.2 V vs. SCE	−2.5	Acetonitrile, 1 ethyl-3 methylimidazolium tetrafluoroborate EMIMBF4	90	CO	108
Cu–Pd/MXene	−2.8 V	150	0.1 m KHCO ₃	93	Formate	127
SnO ₂ /MXene	1.1 V	−57.8	CO ₂ -saturated 0.1 M KHCO ₃	94	Formate	121
ZnO-Fe-MXene	1.0 V	18.745	0.5 M NaOH	-	Formate	225
Cu-/Ti ₃ C ₂ T _x	−1.5 V vs. Ag/AgCl	−1.08	0.1 M NaHCO ₃	58.1	HCOOH	76
MXene (Ti ₃ C ₂ T _x) modified with Boron-doped diamond	−1.3 V vs. Ag/AgCl		0.5 M KOH	97	HCOOH	226

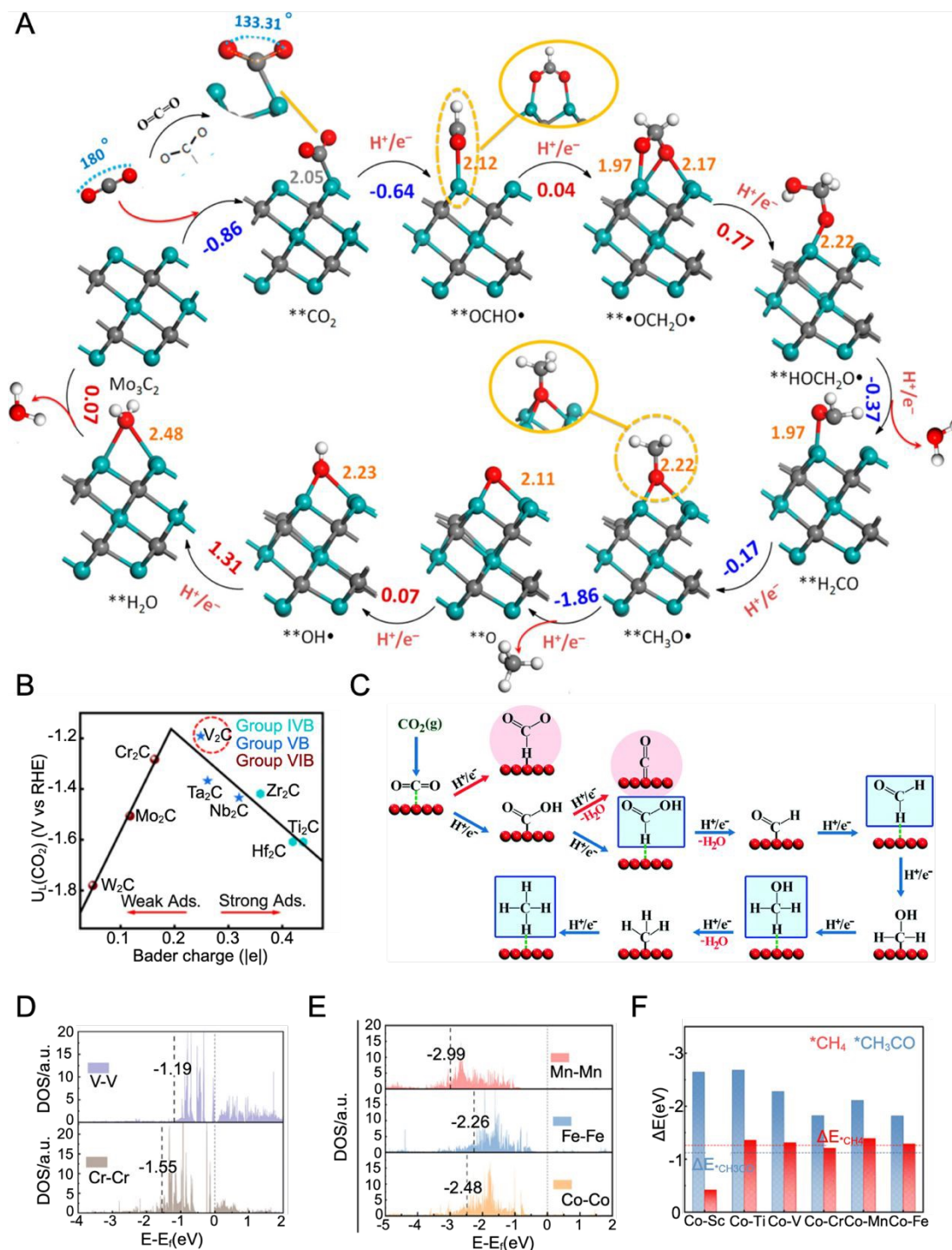


Figure 9. A) CO₂ conversion mechanism into *CH₄ and **H₂O catalyzed by Mo₃C₂ (Reprinted with permission from ACS Nano 2017, 11, 11, 10825–10833. Copyright [2017] American Chemical Society). B) Volcano-type relationship between U_L and the Bader charge of *HCOOH on M₂C (Reprinted with permission from Ind. Eng. Chem. Res. 2023, 62, 48, 20716–20726. Copyright [2023] American Chemical Society). C) Reaction mechanism of electrochemical reduction of CO₂ on O-terminated MXenes (Reproduced from reference [211] with permission from Royal Society of Chemistry, Copyright [2022]). D, E) Density of states (DOS) corresponding to *d*-orbitals of the adsorbed dual-atom, where the d-band center is denoted by dashed lines. F) Adsorption energy of *CH₃CO and *CH₄ intermediates on dual-



atom catalysts/Ti₂CO₂ (D-F, Reproduced from reference [227] with permission from Royal Society of Chemistry, Copyright [2025]).

5. Structural Engineering

MXene-based catalysts are emerging as promising electrocatalysts for the CO₂RR due to their excellent electronic conductivity, large surface area, tunable surface chemistries, and structural robustness^{228,229}. Their surface termination groups can effectively stabilize critical reaction intermediates, facilitating efficient proton-coupled electron transfers essential for CO₂ activation and subsequent reduction pathways. Despite these beneficial properties, the presence of specific surface functionalities, particularly hydrogen-affine groups (such as –OH or –F), can unintentionally promote the competing hydrogen evolution reaction.^{230,231} Specifically, the high density of reactive sites and negatively charged surfaces of MXenes can readily adsorb protons from aqueous electrolytes, thereby enhancing HER activity²³². This unintended promotion of HER poses a significant challenge by diverting electrons and protons from CO₂ reduction, thereby reducing selectivity toward valuable carbon products. To address this intrinsic limitation, various structural engineering approaches have been developed. These strategies include controlled surface termination modification, defect and vacancy engineering, single-atom or heteroatom doping, formation of MXene-based heterostructures, and hybrid composite catalysts. These tailored engineering methods are crucial to selectively suppress HER activity while enhancing MXene-based catalysts' performance and selectivity toward desired CO₂RR products.^{127,128,233–235}

5.1 Surface Termination Engineering

The catalytic selectivity of MXenes toward CO₂RR strongly depends on surface termination groups (e.g., –O, –OH, –F, –Cl),²³⁶. Table 5 compares the effects of MXene surface terminations on CO₂RR intermediates and product selectivity. For instance, Oxygen-terminated MXenes (–O) strongly stabilize key reaction intermediates such as *COOH and *HCOO, reducing the energy barriers for CO₂ conversion reactions and selectively suppressing HER²⁰⁷. Computational studies by Albertus et al. demonstrated that oxygen



terminations on Ti and Mo-based MXenes significantly enhance CO₂ adsorption and intermediate stabilization, promoting selective CO₂RR towards formic acid²⁰⁹. In contrast, MXenes with abundant fluorine (–F) terminations generally exhibit weaker CO₂ adsorption and lower selectivity for carbon-based products due to increased HER activity. Meng et al. explicitly found that fluorinated Ti₃C₂ MXenes exhibit a higher HER overpotential (~0.58 V), indicating their stronger proton affinity and subsequent HER promotion²³⁷. Additionally, recent studies have explored halogen-terminated MXenes (e.g., –Cl, –Br, –I), synthesized via molten salt or halogen etching methods, that offer potential avenues to adjust the electronic structure of MXenes and weaken proton adsorption, which may reduce HER activity²³⁸. However, comprehensive experimental validation of HER suppression in halogen-terminated MXenes remains limited and warrants further investigation.

5.2 Defect Engineering and Heteroatom Doping

Engineering defects and doping MXenes with heteroatoms have proven effective strategies for improving CO₂RR selectivity and suppressing HER by altering electronic structures, modifying intermediate adsorption energies, and enhancing active-site densities.^{239–242} Introducing controlled oxygen vacancies, metal vacancies, or edge defects can significantly boost MXene catalytic performance by selectively stabilizing CO₂-derived intermediates. For example, Qian et al. employed DFT to investigate dual-oxygen vacancies in Mo₂TiC₂O₂ MXenes, revealing enhanced catalytic activity and C–C coupling due to enriched adsorption of reaction intermediates³⁴. Furthermore, heteroatom doping (such as N, P, S, or transition metals) provides another powerful route to tune MXene catalytic properties. Three distinct doping strategies have been identified: lattice substitution, functional substitution, and surface adsorption. Lattice substitution involves replacing atoms in MXene lattices to alter their electronic structures significantly.²⁴³ Functional substitution adjusts surface-functional groups to improve catalytic selectivity. Surface adsorption involves anchoring active dopants on MXene surfaces, stabilizing CO₂RR intermediates, and selectively inhibiting HER. For instance, nitrogen-doped MXenes exhibited enhanced electronic modulation, reducing HER selectivity and promoting carbon-based products such as CO and formic acid.²⁴⁴



5.3 Hybrids and Heterostructures

Forming MXene-based heterostructures or hybrids by integrating MXenes with other 2D materials or active components effectively combines their intrinsic properties, mitigates individual limitations, and significantly enhances CO₂RR selectivity and HER suppression.²⁴⁵ Heterostructure formation typically involves the in situ growth of complementary 2D materials onto MXene surfaces, facilitated by electrostatic interactions or covalent bonding.^{246,247}

Liu et al. demonstrated the synthesis of MXene/metal-organic framework (MOF) heterostructures through electrostatic attraction, where the surface terminations of Ti₃C₂T_x MXene strongly interacted with MOF precursors, forming well-integrated composites that effectively enhanced CO₂ adsorption and catalytic selectivity²⁴⁸. Similarly, a covalent organic framework (COF)-Ti₃C₂ heterostructure achieved >90% CO selectivity at -0.6 V vs. RHE due to the synergistic effect of MXene's large exposed surface area and the COF's catalytic functionalities, substantially suppressing HER.²⁴⁹ This significant performance was primarily attributed to the large, exposed surface of the MXene, which effectively disperses the COF, endows the heterojunction with more active sites, and facilitates efficient transport channels. The 3D MXene/graphene oxide/perylene diimide aerogel heterostructure was synthesized via impregnation and freeze-drying for photocatalytic CO₂RR.²³⁴ The resulting heterostructure featured a large surface area, an enhanced photogenerated carrier, and an electron transfer network facilitated by π - π stacking via electrostatic attraction. This structural configuration, interconnecting the faces of the heterostructure, promotes the efficient transfer of photogenerated electron-hole pairs, enabling rapid carrier movement and separation. Additionally, perylene diimide functions as an electron donor, activating catalytic sites for enhanced photocatalytic CO₂RR.

5.4 Single-Atom Catalysts

The size of metal particles in metal-based heterogeneous catalysis is intricately linked to catalytic activity.²⁵⁰ Catalytic activity increases as the size of metal nanoparticles decreases until they reach an optimal size.



Understanding this fundamental concept has played a significant role in advancing SACs, which display high catalytic activity and maximize metal utilization due to the significantly larger surface area and quantum size effects of metal nanoparticles compared to their bulk counterparts.^{251–253} Based on this well-established principle, extensive studies have demonstrated that controlling the structure and size of metal nanoparticles at the atomic level maximizes metal utilization and enhances electrocatalytic performance.²⁵⁴ The choice of support material for dispersing single metal atoms plays a crucial role in determining the activity and stability of single atoms under reaction conditions. Therefore, strong metal–support interactions are essential for maintaining catalyst performance.²⁵⁵

Computational and experimental studies have highlighted the potential of MXenes as promising support materials for facilitating strong metal–support interactions in CO₂RR catalysts. The abundant surface-functional groups and metal vacancy defects in MXene serve as ideal anchoring sites for single metal atoms, primarily due to the high surface energy, adjustable electronic structure, and uniform atomic arrangement of MXene.^{213,256–258} The synthesis of MXene-based SACs can be achieved using three strategies: surface adsorption, metal vacancy anchoring, and anchoring at surface-functional group vacancies.²⁵⁹ According to a computational study, the adsorption of single metal atoms is possible on the top, hollow (hcp and fcc), and bridge sites.

Chen et al.²⁶⁰ employed electrostatic adsorption and in situ reduction to synthesize a Co-Ti₃C₂T_x SAC for photocatalytic CO₂ reduction. Cocations are initially adsorbed onto the negatively charged functional groups on the MXene surface during synthesis, forming ionic bonds facilitated by electrostatic attraction. The ionic bond formation is followed by reducing Co cations on MXene, leading to covalent bonds between the metal atoms and surface-functional groups (–F and –O). Sodium borohydride was employed as a reducing agent for Co²⁺ ions and as an oxidation inhibitor of MXene to overcome its fast oxidation.

Zhou et al.²⁴⁹ designed and synthesized the MXene@Por-COF-Co heterostructure. The dispersed COF structures and exposed MXene nanosheets offer more accessible reactive sites and quicker ion transfer



channels to the heterostructure because the covalent interactions between the aldehyde groups in the COF structures and the amino groups of MXene can facilitate the in situ formation of COFs on the surface of amino-functionalized MXene nanosheets. TEM images of MXene@Por-COF-Co-7 reveal a homogeneous distribution of COF nanosheets across the surface of the MXene nanosheets. Furthermore, MXene@Por-COF-Co-7 exhibits a remarkable CO FE of 97.28% at -0.6 V, significantly higher than that of Por-COF-Co (0%) at the same potential. In addition, MXene@Por-COF-Co-7 also maintains a high FE in the potential range of -0.5 to -1 V vs. RHE, suggesting its good selectivity for CO formation. The bias current density of CO increased with a rise in voltage.

Zhao et al.²⁶¹ employed self-reduction stabilization to anchor platinum (Pt) single atoms onto Ti vacancies of Ti_3C_2 for CO_2 activation with amines and silane, producing formamides. The single Pt atoms on the $\text{Ti}_{3-x}\text{C}_2\text{T}_y$ support exhibited partial positive charges and atomic dispersion. Adsorbing and reducing Pt^{4+} simultaneously was successful without adding a reductant. Moreover, HAADF imaging revealed that the Pt single atoms were anchored at the Ti site in Ti_3C_2 rather than at the lattice gap (Figure 10A). These Ti vacancies strongly correlate with the etching conditions during MXene synthesis, especially the etchant. Figure 10B reveals that $\text{Pt}_1/\text{Ti}_{3-x}\text{C}_2\text{T}_y$ SAC displayed superior catalytic performance for converting CO_2 compared to that of Pt nanoparticles (NPs).

Zhao et al.¹⁰⁶ developed a single-atom Cu loaded on MXene layers by selectively etching Al layers from quaternary MAX phases $[\text{Ti}_3(\text{Al}_{1-x}\text{Cu}_x)\text{C}_2]$ for CH_3OH synthesis, applying an easy sublimation of AlCl_3 and leaving unreacted Cu on the MXene. The improved selectivity for CH_3OH arises from the capacity of atomically dispersed Cu sites to impede the C–C coupling of $^*\text{CO}$, facilitating the formation of CH_3OH (Figure 10C). This coordination lowers the energy barrier for converting HCOOH^* into an absorbed CHO^* intermediate, enhancing electrocatalytic activity for CO_2 conversion. The SA-Cu-MXene catalyst exhibited an increased FE of 59.1% for CH_3OH production with high stability and a low energy barrier for the rate-determining step (HCOOH^* to CHO^* ; Figure 10D, E).



Bao et al.²⁶² synthesized a Cu SAC anchored on $\text{Ti}_3\text{C}_2\text{T}_x$ nanosheets via chemical reduction, followed by freeze-drying. The resulting Cu-NP/ $\text{Ti}_3\text{C}_2\text{T}_x$ SAC reduced CO well, achieving over 98% selectivity toward C_{2+} products with a high C_2H_4 selectivity of 71% (Figure 10F). The catalyst promotes the formation of the *CO-CHO intermediate, facilitating C-C coupling. The XANES analysis revealed that the Cu valence state in Cu-NP/ $\text{Ti}_3\text{C}_2\text{T}_x$ SAC lies between that of metallic Cu and Cu^+ , indicating the presence of O coordination and formation of Cu-O₃ species (Figure 10G and H).

Similarly, Liu et al.²⁶³ reported a monoatomic Cu catalyst featuring Cu-N₁C₁ coordination anchored on N-doped $\text{Ti}_3\text{C}_2\text{T}_x$ MXene for the efficient CO₂ reduction to CO. This catalyst achieved over 97% selectivity toward CO at an applied potential of -0.58 V vs. RHE (Figure 10J). The excellent performance was attributed to a potential-dependent valence transition of the Cu species. Aberration-corrected HAADF imaging indicated a high density of Ti vacancies in the MXene lattice, serving as preferential anchoring sites for immobilizing isolated Cu atoms (Figure 10I). The XANES analysis revealed a negative shift in the Cu absorption edge relative to the pristine $\text{Ti}_3\text{C}_2\text{T}_x$, which is indicative of strong electronic interactions between Cu single atoms and the MXene support (Figure 10K).

In developing SACs, a primary consideration is their stability because several factors, such as decomposition, dissolution, and atom migration, can promote cluster formation and morphological degradation. The high surface energy and mobility of isolated atoms drive these transformations.²⁶⁴ Instability in SACs often results in diminished current density and FE^{265,266}. Although many studies on MXene-based SACs for CO₂RR have emphasized activity and selectivity, the stability of the single atoms under reaction conditions remains underexplored. A comprehensive literature review reveals the scarcity of post-reaction structural and chemical characterization data for MXene SACs.

Future investigations should prioritize evaluating catalyst stability by conducting detailed post-reaction analyses. Such efforts could provide crucial insight into the structural and chemical evolution of catalysts,



1054 facilitating the rational design of MXene–single-atom interactions for enhanced catalytic activity, durability,
1055 and selectivity.

1056 The DFT has been pivotal in advancing 2D material-based electrocatalysis by predicting performance under
1057 several atomic configurations.^{80,267,268} This theory has been critical in developing SAC-supported 2D
1058 material-based electrocatalysts. Numerous studies have employed the DFT to design SAC-MXene-based
1059 catalysts for CO₂RR. For instance, Li et al.²⁵⁹ demonstrated the high catalytic activity of single-atom
1060 scandium (Sc), Ti, and V-supported Ti₂CN₂ to produce CO with a low overpotential of 0.37, 0.27, and
1061 0.23 eV, respectively. In contrast, Mn and Fe supported on Ti₂CN₂ primarily produce HCOOH with a low
1062 overpotential of 0.32 and 0.43 eV. The high catalytic activity of single atoms on Ti₂CN₂ can be attributed
1063 to N-functionalization, stabilizing SACs effectively by anchoring TM atoms. This functionalization also
1064 lowers the energy barrier for CO₂ reduction and improves catalytic selectivity. These SACs on Ti₂CN₂
1065 exhibit high catalytic activity with much lower overpotentials.

1066 Similarly, Athawale et al.²³⁵ explored the feasibility of MXene serving as an anchoring site for isolating TM
1067 SACs for CO₂RR. Several SAC systems containing 3d (Sc, Ti, V, Cr, and Mn), 4d (yttrium [Y], zirconium
1068 [Zr], niobium [Nb], and Mo), and 5d (hafnium [Hf]) transition metals, supported on an O-terminated MXene
1069 (TM@Ti₂CO₂), were designed using DFT calculations. The findings indicate that TMs anchored on top of
1070 the C atom of Ti₂CO₂ (hollow-C site) present the most stable configuration. The hollow-C site, primarily
1071 for Nb, Mo, Zr, V, Cr, and Ti atoms, exhibits the most negative E_b values, indicating higher stability and
1072 better suitability for CO₂RR.



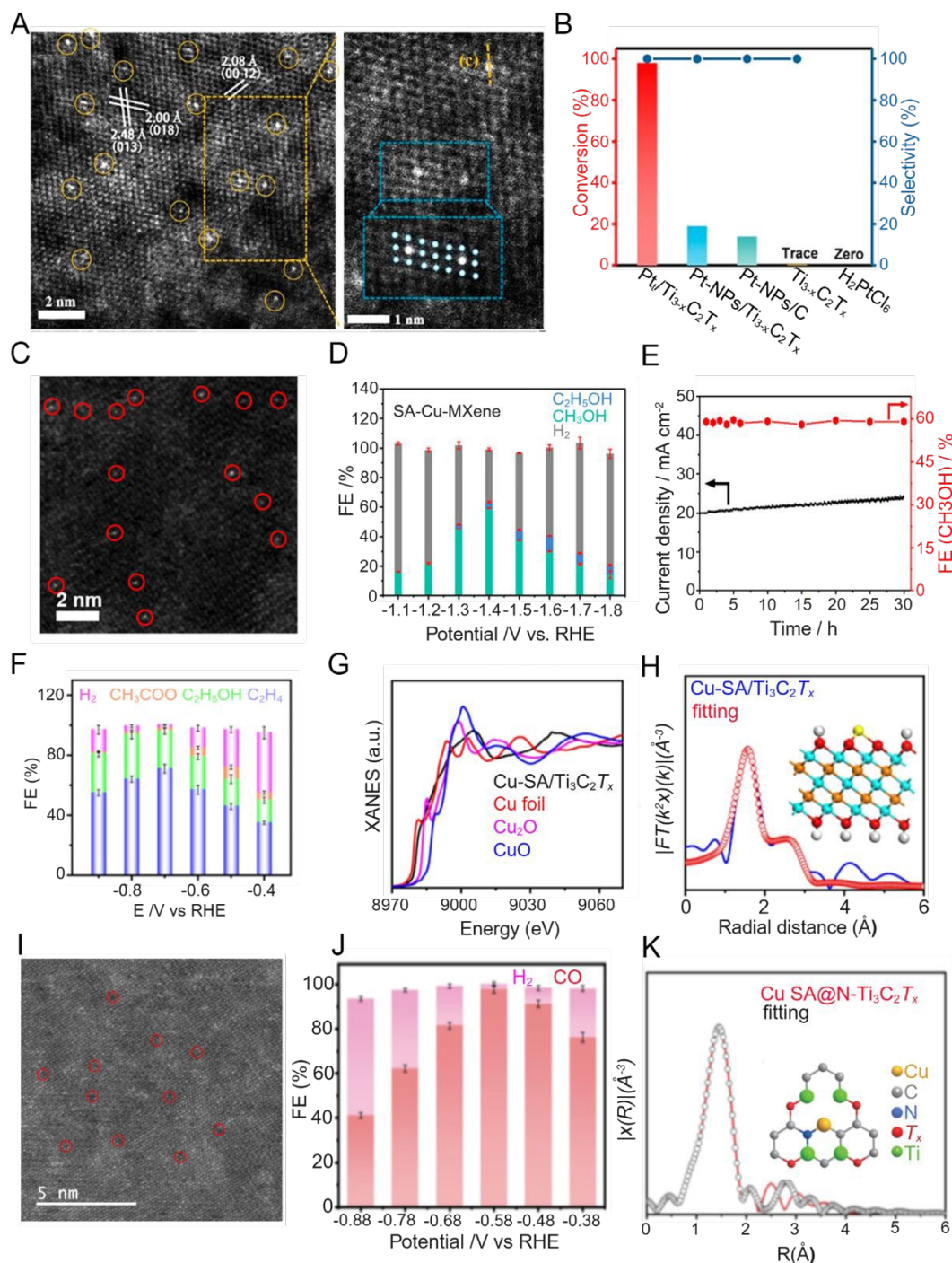


Figure 10. A) High-angle annular dark-field (HAADF) scanning transmission electron microscopy (STEM) image of Pt/Ti_{3-x}C₂T_x. B) Catalytic performance of catalyst systems (A and B, Reprinted with permission from J. Am. Chem. Soc. 2019, 141, 9, 4086–4093. Copyright [2019] American Chemical Society). C) Aberration-corrected (AC) HAADF-STEM image of SA-Cu-MXene. D) Faradaic efficiency (FE) of product formation on SA-Cu-MXene. E) Current stability and corresponding FE for CH₃OH formation on SA-Cu-MXene (C-E, Reprinted with permission from ACS Nano 2021, 15, 3, 4927–4936. Copyright [2021] American Chemical Society). F) FE of Cu-SA-Ti₃C₂T_x. G) X-ray absorption near-edge structure spectra at the Cu K-edge with CuO, Cu₂O, and Cu foil as a reference. H) Extended X-ray absorption fine structure (EXAFS) fitting curve of Cu-SA/Ti₃C₂T_x; inset illustrates the Cu-SA-Ti₃C₂T_x structure.



Yellow, blue, dark yellow, red, and white balls represent Cu, Ti, C, O, and H, respectively (F-H, Reproduced from reference [262] with permission from Springer Nature, Copyright [2021]). I) AC HAADF-STEM of $\text{Ti}_3\text{C}_2\text{T}_x$ demonstrating Ti vacancies.²⁶³ J) Potential-dependent FE of H_2 and CO on Cu SA@N- $\text{Ti}_3\text{C}_2\text{T}_x$ at applied potentials. K) EXAFS fitting of Cu SA@N- $\text{Ti}_3\text{C}_2\text{T}_x$, inset presents the atomic interface structure model (I-K, Reproduced from reference [263] with permission from Springer Nature, Copyright [2024]).

5.5 MXene-Metal/Metal–Oxide Hybrids

Metal and metal oxide (MMO) catalysts have demonstrated notable potential in CO_2RR ; however, their application is often limited by intrinsic drawbacks such as low electrical conductivity, poor long-term stability, and limited product selectivity.^{269–271} To overcome these challenges, hybrid electrocatalysts that integrate MMOs with conductive and chemically tunable materials, such as MXenes, have emerged as an effective strategy.^{272–274} MXenes offer high electrical conductivity, a two-dimensional architecture, and versatile surface terminations, collectively making them ideal supports for enhancing the performance of MMO-based systems. The integration of MMOs with MXenes generates synergistic interfacial interactions that modulate the electronic structure of active sites, improve charge transport, and promote favorable binding of CO_2RR intermediates. Specifically, the surface terminations of MXenes (e.g., $-\text{O}$, $-\text{OH}$, $-\text{F}$) can attract metal cations from the MMO phase and facilitate oxygen vacancy formation at the interface, enhancing catalytic activity and electron transfer efficiency.^{224,235,275} These vacancies serve as additional active sites and improve the adsorption and activation of CO_2 molecules. For example, Wu et al. developed a $\text{Fe}_2\text{O}_3@\text{MXene}$ hybrid photocatalyst in which the introduction of $\text{Ti}_3\text{C}_2\text{T}_x$ increased oxygen vacancy concentration and formed $\text{Fe}-\text{O}-\text{Ti}$ bonds at the interface. These interfacial sites enhanced $^*\text{COOH}$ intermediate formation and improved CO production. Although this system was used for photocatalytic CO_2 reduction, the findings highlight the general importance of MXene–MMO synergy, which is also transferable to electrocatalytic applications.^{41,233,276}

In the electrocatalytic domain, Liu et al.²⁷⁷ reported a hybrid composed of TiO_2 and SnO_2 nanowires self-assembled onto Ti_3C_2 MXene via van der Waals interactions. The MXene suppressed MMO aggregation,



provided efficient electron pathways, and improved structural integrity. This integration enhanced CO₂ adsorption and activation, significantly improving CO₂RR activity.²⁷⁸

Hao et al.²²⁴ Fabricated an Ag–ZnO/Ti₃C₂T_x hybrid catalyst via a cation exchange and self-assembly method—the MXene-regulated interface featured undercoordinated sites and mesoporous nanostructures. The catalyst achieved nearly 100% CO FE and a partial current density of 22.59 mA cm⁻² at –0.87 V vs. RHE (Figure 11A). DFT calculations confirmed that MXene addition shifted the d-band center, enhanced *COOH binding, and lowered the energy barrier for intermediate formation (Figure 11B). In situ attenuated total reflectance infrared spectroscopy offered valuable insight into the reaction intermediates, elucidating the origin of CO selectivity (Figure 11C, D). Within the applied potential window of –0.123 to –1.423 V, the attenuated total reflectance infrared spectra revealed characteristic signals corresponding to CO₂, CO₃²⁻, and adsorbed *CO species. The *CO bands exhibited a bipolar profile, indicative of Fano line shape modulation. For the Ag–ZnO/Ti₃C₂T_x catalyst, the inverted band observed at 1,920 cm⁻¹ was attributed to linearly bonded CO (CO_L), whereas the positive band at 1,800 cm⁻¹ was assigned to bridge-bonded CO (CO_B). These observations suggest that forming *CO intermediates from CO₂ is more favorable on Ag–ZnO/Ti₃C₂T_x than on Ag–ZnO. The DFT revealed that adding MXene facilitated stronger binding abilities of *COOH compared to Ag–ZnO. Moreover, MXene regulated the Ag–ZnO interface by reducing the electron filling of antibinding sites and optimizing the electronic structure by lowering the formation energy barrier of the intermediate.

Similarly, Cao et al.²³³ reported on a ZnO/N–Ti₃C₂T_x catalyst that achieved an FE exceeding 96% for CO production. ZnO provided the primary active sites for CO₂ conversion, while the N-doped MXene improved textural properties and conductivity, facilitating PCET. Similarly, SnO₂ quantum dots grown on ultrathin Ti₃C₂T_x MXene sheets (via hydrothermal synthesis) delivered a 94% FE and a partial current density of 57.8 mA cm⁻² for formate production. In situ XANES measurements revealed that SnO₂ was partially reduced to metallic Sn during operation, which acted as the true catalytic site. Coordination environment



changes observed via EXAFS confirmed strong Sn–Ti interfacial coupling unique to the MXene-based hybrid (Figures 11H–F).¹²¹ In addition, the absorption edge position of the Sn K-edge XANES spectrum for SnO₂/MXene is situated between that of metallic Sn foil (Sn⁰) and SnO₂ (Sn⁴⁺; Figure 11G). The extended x-ray absorption fine structure spectra of SnO₂/MXene in the R-space and K-space differ from those of pure SnO₂, suggesting that the local coordination environment of Sn in SnO₂/MXene is unlike that in pristine SnO₂.

In a similar study, Yu et al.²¹⁰ synthesized a TiO₂/Ti₃C₂ MXene photocatalyst via thermal calcination. By adjusting the temperature (350–650 °C), TiO₂ nanoparticle loading was modulated, influencing CH₄ production. Though photocatalytic, this system again underscores the broader relevance of MXene–MMO interactions across catalytic modalities.

Recently, a Cu₂O/MXene 0D/2D hybrid catalyst demonstrated excellent selectivity for propane (C₃H₈) production at –1.3 V vs. RHE.²⁷⁹ The interface between Cu₂O and MXene created cooperative binding sites, MXene favored *CO adsorption while Cu₂O stabilized *C₂ intermediates, facilitating C–C–C coupling and efficient hydrogenation to C₃ products. This hybrid highlights the unique potential of MXene–MMO heterostructures in enabling multicarbon product formation, which is rarely achieved using either component alone. These examples illustrate how electronic coupling, vacancy engineering, and interfacial coordination at the MXene–MMO boundary promote enhanced CO₂ adsorption, intermediate stabilization (e.g., *COOH, *CHO), and improved selectivity. Moreover, MXenes can help suppress competing hydrogen evolution reactions due to their hydrophilicity and binding site modulation, thereby further enhancing CO₂RR selectivity. Future work should focus on understanding how the oxidation states, vacancy density, and structural morphology of MXenes and MMOs evolve under electrochemical operating conditions, and how these changes influence catalytic stability and product distribution. In particular, quantifying the role of MXenes in HER suppression and tailoring interfaces for selective multi-electron/multicarbon pathways are promising directions for designing next-generation MXene-based hybrid electrocatalysts.



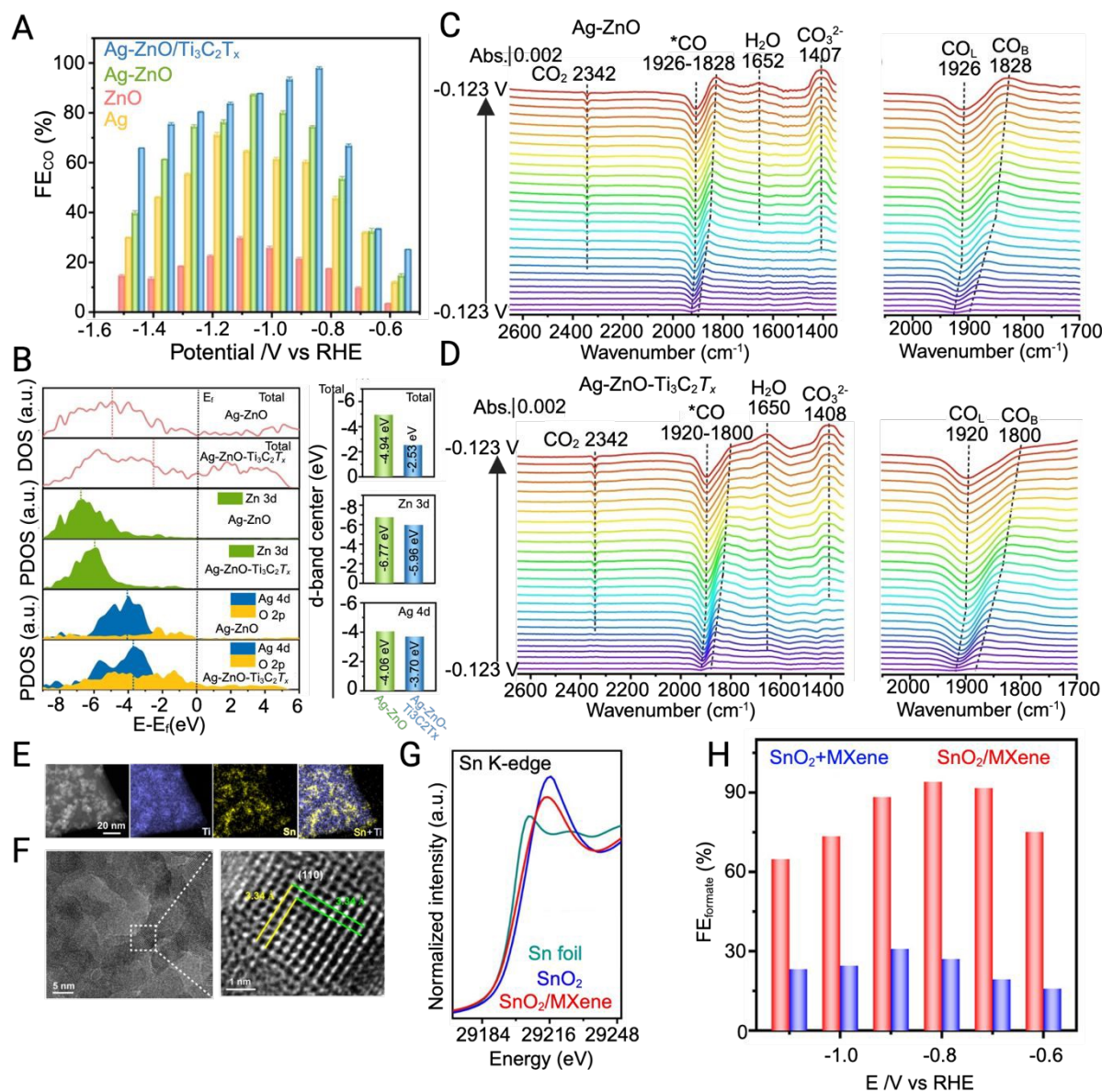


Figure 11. A) Faradaic efficiency (FE) of CO on Ag-ZnO-Ti₃C₂T_x. B) Density of states (DOS) for Zn 3d, Ag 4d, and O 2p orbitals of Ag-ZnO and Ag-ZnO-Ti₃C₂T_x (left pane) and the corresponding d-band center (right pane). C-D) In situ attenuated total reflectance infrared spectra while stepping the potential from -0.123 to -1.423 V on C) Ag-ZnO and D) Ag-ZnO-Ti₃C₂T_x. (A-D, "Reproduced from reference [224] with permission from Wiley and Sons, Copyright [2023]"). E) Low-magnification high-angle annular dark-field scanning transmission electron microscopy image and corresponding electron-dispersive spectroscopy element images of SnO₂/MXene. F) High-resolution transmission electron microscopy image and lattice plane. G) Sn K-edge x-ray absorption near-edge structure spectra of the SnO₂/MXene catalyst, Sn foil, and SnO₂ references. H) Potential-dependent FE of formate (E-H, "Reproduced from reference [121] with permission from PNAS, Copyright [2022]").

1159
1160
1161
1162
1163
1164
1165
1166
1167



6. Challenges and Outlook

MXene-based electrocatalysts show exceptional promise for the electrochemical reduction of CO₂ due to their high conductivity, tunable surface chemistry, and structural versatility. Despite significant progress, several interconnected challenges must be addressed to transition these materials from fundamental research to practical, large-scale implementation. A key challenge is balancing catalytic activity, selectivity, and energy efficiency, particularly the selective formation of higher-value multicarbon products such as ethylene, ethanol, and propanol. Currently, MXenes predominantly yield simpler products like CO and formate due to limitations in intermediate stabilization and the competing HER. Future strategies involving advanced surface engineering, controlled doping, and precise defect management are essential to overcome these scaling limitations and direct reaction pathways toward desired multicarbon products.

Beyond intrinsic catalyst design, the practical implementation of MXene-based electrocatalysts is significantly influenced by reactor-level constraints inherent to industrial electrolyzer systems (as discussed in Section 2.1). Industrial electrolyzers require operation under stringent conditions, including continuous high current densities (>200 mA cm⁻²), efficient heat and water management, effective control of CO₂ crossover, and stable long-term performance. Traditional laboratory-scale H-cell reactors, which dominate fundamental studies, fail to replicate these conditions due to inherent limitations such as low CO₂ solubility (~33 mM), diffusion-controlled mass transport, large electrode spacing, and dilute electrolytes, resulting in low achievable current densities (<100 mA cm⁻²). Consequently, performance metrics derived from H-cells rarely translate effectively to industrial-scale systems. These reactor designs significantly enhance CO₂ transport through direct gas-phase delivery, minimize ohmic losses, control reaction interfaces more effectively, and offer improved electrolyte management, addressing many limitations of conventional H-cell setups.

Nevertheless, a lack of standardized evaluation protocols hinders widespread adoption and advancement in MXene-based CO₂RR. Variations in cell designs, electrode materials, electrolyte compositions, gas flow conditions, and performance metrics currently impede meaningful comparison between studies.



1194 Establishing community-wide benchmarking guidelines and uniform testing standards will enhance
1195 performance evaluation reproducibility, transparency, and reliability.

1196 Moreover, the catalytic performance of MXenes remains closely tied to their synthesis routes, which
1197 influence structural characteristics such as flake size, surface termination chemistry ($-O$, $-OH$, $-F$), and
1198 defect density. Oxygen-terminated MXenes have demonstrated promising catalytic properties by lowering
1199 reaction barriers and stabilizing critical reaction intermediates. However, achieving reproducible and
1200 controlled termination profiles is challenging. To address this, scalable, cost-effective, and precisely
1201 controllable synthesis methods must be developed. Additionally, defect engineering and doping offer
1202 strategic routes to optimize the catalytic properties of MXenes. Introducing oxygen vacancies or doping
1203 with heteroatoms (N, P, or transition metals) can modify the electronic structure, enhance active site
1204 densities, and tune intermediate binding energies. However, excessive defects may negatively affect
1205 structural stability and induce undesired side reactions. Therefore, careful optimization and systematic
1206 evaluation of doping strategies under realistic electrochemical conditions are necessary.

1207 Significant gaps remain between computational predictions and experimental outcomes. Many theoretical
1208 studies utilize idealized MXene structures without realistic surface heterogeneities and defects.
1209 Experimentally synthesized MXenes typically feature mixed terminations, variable flake sizes, and
1210 structural imperfections. Future theoretical efforts should incorporate realistic structural models that account
1211 for these variations to enhance predictive accuracy, thereby more effectively guiding experimental
1212 development.

1213 Currently, most experimental CO_2RR studies focus on $Ti_3C_2T_x$ MXenes. Exploring under-investigated
1214 MXene compositions such as Mo_2CT_x , Nb_2CT_x , and V_2CT_x could uncover unique catalytic properties,
1215 improved stability, and enhanced activity. Leveraging machine learning and high-throughput computational
1216 screening methods may accelerate the discovery of promising MXene candidates and guide targeted
1217 experimental validation.

1218 The operational stability of MXenes under realistic electrochemical conditions remains relatively
1219 unexplored. Prolonged exposure to negative potentials, variable pH environments, and continuous gas flow



Open Access Article. Published on 22/07/2025. Downloaded on 30/07/2025 01:23:42.
This article is licensed under a Creative Commons Attribution 3.0 Unported Licence.



can induce oxidation, structural deformation, and changes in surface termination composition. To address this, in situ and operando characterization techniques such as transmission electron microscopy (TEM), X-ray absorption spectroscopy (XAS), and Raman spectroscopy should be employed to monitor catalyst evolution under reaction conditions. Such insights are crucial for designing MXenes with enhanced durability and reliable long-term performance. Finally, emerging fabrication technologies, particularly additive manufacturing and 3D printing, offer novel opportunities for transitioning MXene catalysts into practical, scalable electrode architectures. Printable MXene inks, already successfully demonstrated in energy storage and electronics, could facilitate customized, high-surface-area electrode designs, enhancing mass transport and reaction interface stability. Combining MXenes with complementary materials through advanced printing techniques further opens new possibilities for scalable integration into commercial CO₂RR systems. In summary, the successful industrial deployment of MXene-based electrocatalysts for CO₂RR demands a comprehensive approach that integrates advanced material synthesis and surface engineering, optimized reactor design, standardized evaluation methods, and scalable fabrication techniques.

6.1 Economic Viability and Cost Reduction

While MXenes offer significant advantages in catalytic performance, tunability, and selectivity, their current production costs remain a nontrivial challenge for commercial adoption. Laboratory-scale synthesis protocols, often involving high-purity MAX-phase precursors, hazardous etching agents (e.g., HF or LiF/HCl), and multi-step purification, contribute to relatively high per-gram costs, often ranging from 100 to 1000 USD, depending on scale and quality. However, recent advances in scalable and safer synthesis actively address this limitation. Alternative Fluoride-free etching strategies, including electrochemical, alkaline, and molten-salt routes, eliminate the need for hazardous chemicals while improving yield and environmental safety. Continuous-flow production methods have demonstrated multi-gram scale fabrication with excellent reproducibility and are being increasingly optimized for cost-effectiveness. For example, Anasori et al.⁴¹ reconducted a life-cycle analysis demonstrating reduced environmental and financial costs

Materials Horizons Accepted Manuscript

when replacing HF-based synthesis with alternative etching processes. Another critical factor in cost reduction lies in material efficiency. Due to their high intrinsic conductivity and activity, MXenes often require lower loadings to achieve catalytic performance than conventional catalysts. In hybrid systems, such as MXene-metal oxide composites or single-atom-doped MXenes, the synergy between active sites allows for minimized MXene usage while maintaining or enhancing selectivity and stability. Long-term durability further enhances economic feasibility. Stable MXene-based catalysts reduce the need for frequent replacement, lowering operational expenses over extended use cycles. Moreover, enhanced selectivity for high-value CO₂RR products, such as C₂₊ compounds, increases the overall value of the catalytic process. As interest grows, industrial integration and shared manufacturing infrastructure (e.g., with battery or supercapacitor industries) may further lower precursor costs and streamline production. Techno-economic assessments of MXene-based membrane electrode assemblies (MEAs) and gas-diffusion electrodes (GDEs) are beginning to demonstrate promising cost-performance tradeoffs at the device level. Finally, it's worth mentioning that while Ti₃C₂T_x MXenes currently cost approximately 20–100 USD/g, this is still considerably lower than noble-metal catalysts (e.g., Pt/C at ~156 USD/g), and MXenes offer additional value through superior tunability, conductivity, and durability. In conclusion, although MXenes are currently more expensive than traditional transition-metal-based electrocatalysts, ongoing innovations in synthesis, material design, and system integration are rapidly closing the gap. With continued improvements in low-cost, scalable production methods, reduced catalyst loading requirements, and enhanced operational lifetimes, MXene-based materials are increasingly positioned as cost-effective and high-performance candidates for industrial CO₂RR.

Acknowledgments

This work was conducted with the financial support of Saudi Aramco and the resources and facilities provided by the King Abdullah University of Science and Technology (KAUST, BAS/1/1403).



References

1 X. Q. Tan, W. Mo, X. Lin, J. Y. Loh, A. R. Mohamed and W. J. Ong, *Nanoscale*, 2023, **15**, 6536–6562.

2 L. J. R. Nunes, *Environments*, DOI:10.3390/environments10040066.

3 K. Wang, M. A. Rehman, S. Fahad and Z. Linzhao, *Resour. Policy.*, 2023, **81**, 103384.

4 Z. K. Dijoo and R. Khurshid, *Environ. Biotechnol.*, 2022, 39–56.

5 S. Fang, M. Rahaman, J. Bharti, E. Reisner, M. Robert, G. A. Ozin and Y. H. Hu, *Nat. Rev. Methods Primers.*, 2023, **3**, 1–21.

6 A. S. Joel and Y. M. Isa, *J. Chem. Tech. Biotechnol.*, 2023, **98**, 838–855.

7 H. Lee and J. Romero, 2023, 184.

8 T. M. Gür, *Prog. Energy Combust. Sci.*, 2022, **89**, 100965.

9 T. Patil, S. Dharaskar, M. Sinha and S. S. Jampa, *Environ. Sci. Pollut.*, 2022, **29**, 35723–35745.

10 N. Shreyash, M. Sonker, S. Bajpai, S. K. Tiwary, M. A. Khan, S. Raj, T. Sharma and S. Biswas, *Energies (Basel)*, 2021, **14**, 4978.

11 V. Kumaravel, J. Bartlett and S. C. Pillai, *ACS Energy Lett.*, 2020, 486–519.

12 M. Ozkan and R. Custelcean, *MRS Bull*, 2022, **47**, 390–394.

13 J. A. Garcia, M. Villen-Guzman, J. M. Rodriguez-Maroto and J. M. Paz-Garcia, *J. Environ.Chem. Eng.*, 2022, **10**, 108470.



- 1286 14 Y. Zhang, L. Yu, K. Cui, H. Wang and T. Fu, *Chem. Eng. J.*, 2023, **455**, 140552.
- 1287 15 R. Shaw and S. Mukherjee, *Carbon Capture Science & Technology*, 2022, **2**, 100036.
- 1288 16 W. J. Lee, C. Li, H. Prajitno, J. Yoo, J. Patel, Y. Yang and S. Lim, *Catal. Today*, 2021, **368**, 2–
1289 19.
- 1290 17 K. Fernández-Caso, G. Díaz-Sainz, M. Alvarez-Guerra and A. Irabien, *ACS Energy Lett.*, 2023,
1291 **8**, 1992–2024.
- 1292 18 S. Fang, M. Rahaman, J. Bharti, E. Reisner, M. Robert, G. A. Ozin and Y. H. Hu, *Nat. Rev.*
1293 *Methods Primers.*, 2023, **3**, 1–21.
- 1294 19 C. Song, Z. Wang, Z. Yin, D. Xiao and D. Ma, *Chem Catal.*, 2022, **2**, 52–83.
- 1295 20 J. Zhou, H. Liu and H. Wang, *Chin. Chem. Lett.*, 2023, **34**, 107420.
- 1296 21 S. Zong, A. Chen, M. Wiśniewski, L. Macheli, L. L. Jewell, D. Hildebrandt and X. Liu, *Carbon*
1297 *Capture Science & Technology*, 2023, **8**, 100133.
- 1298 22 Z. Masoumi, M. Tayebi, M. Tayebi, S. A. Masoumi Lari, N. Sewwandi, B. Seo, C. S. Lim, H. G.
1299 Kim and D. Kyung, *Int. J. Mol. Sci.*, 2023, **24**, 9952.
- 1300 23 Z. Chen, X. Wang, J. P. Mills, C. Du, J. Kim, J. Wen and Y. A. Wu, *Nanoscale*, 2021, **13**, 19712–
1301 19739.
- 1302 24 M. Salehi, H. Al-Mahayni, A. Farzi, M. McKee, S. Kaviani, E. Pajootan, R. Lin, N. Kornienko
1303 and A. Seifitokaldani, *Appl. Catal. B: Environ.*, 2024, **353**, 124061.



Open Access Article. Published on 22/07/2025. Downloaded on 30/07/25 01:23:42.
This article is licensed under a Creative Commons Attribution 3.0 Unported Licence.



Materials Horizons Accepted Manuscript

1304 25 M. Li, S. Garg, X. Chang, L. Ge, L. Li, M. Konarova, T. E. Rufford, V. Rudolph and G. Wang,
1305 *Small Methods*, 2020, **4**, 2000033.

1306 26 Z. Wang, Y. Zhou, P. Qiu, C. Xia, W. Fang, J. Jin, L. Huang, P. Deng, Y. Su, R. Crespo-Otero, X.
1307 Tian, B. You, W. Guo, D. Di Tommaso, Y. Pang, S. Ding and B. Y. Xia, *Adv. Mater.*, 2023, **35**,
1308 2303052.

1309 27 L. Xiao, Q. Zheng, S. Luo, Y. Ying, R. Zhou, S. Zhou, X. Li, X. Ye, Z. Yu, Q. Xu, H. Liao and J. Xu,
1310 *Sci. Adv.*, 2024, **10**, 2707.

1311 28 C. Long, X. Liu, K. Wan, Y. Jiang, P. An, C. Yang, G. Wu, W. Wang, J. Guo, L. Li, K. Pang, Q. Li,
1312 C. Cui, S. Liu, T. Tan and Z. Tang, *Sci. Adv.*,
1313 DOI:10.1126/SCIADV.ADI6119/SUPPL_FILE/SCIADV.ADI6119_MOVIES_S1_AND_S2.ZIP.

1314 29 B. Peng, H. She, Z. Wei, Z. Sun, Z. Deng, Z. Sun and W. Chen, *Nat. Commun*, 2025, **16**, 1–11.

1315 30 W. Ma, S. Xie, T. Liu, Q. Fan, J. Ye, F. Sun, Z. Jiang, Q. Zhang, J. Cheng and Y. Wang, *Nat.*
1316 *Catal.*, 2020, **3**, 478–487.

1317 31 L. Fan, F. Li, T. Liu, J. E. Huang, R. K. Miao, Y. Yan, S. Feng, C. W. Tai, S. F. Hung, H. J. Tsai, M.
1318 C. Chen, Y. Bai, D. Kim, S. Park, P. Papangelakis, C. Wu, A. Shayesteh Zeraati, R. Dorakhan,
1319 L. Sun, D. Sinton and E. Sargent, *Nat. Synth.*, 2024, **4**, 262–270.

1320 32 H. Bin Yang, S. F. Hung, S. Liu, K. Yuan, S. Miao, L. Zhang, X. Huang, H. Y. Wang, W. Cai, R.
1321 Chen, J. Gao, X. Yang, W. Chen, Y. Huang, H. M. Chen, C. M. Li, T. Zhang and B. Liu, *Nat.*
1322 *Energy*, 2018, **3**, 140–147.

1323 33 A. D. Handoko, H. Chen, Y. Lum, Q. Zhang, B. Anasori and Z. W. Seh, *iScience*, 2020, **23**,
1324 101181.

- 1325 34 X. Qian, L. Li, Y. Li, Z. Liu, Z. Tian, C. Zhan and L. Chen, *Phys. Chem. Chem. Phys.*, 2021, **23**,
1326 12431–12438.
- 1327 35 Z. Li, Y. Wu, Z. Li and Y. Wu, *Small*, 2019, **15**, 1804736.
- 1328 36 A. K. Worku, M. A. Alemu, D. W. Ayele, M. Z. Getie and M. A. Teshager, *Green Chem. Lett.*
1329 *Rev.*, 2024, **17**, 2325983.
- 1330 37 B. Anasori and Y. Gogotsi, *Springer, Cham.*, 2019, 3–12.
- 1331 38 H. M. A. Sharif, M. Rashad, I. Hussain, A. Abbas, O. F. Aldosari and C. Li, *Elsevier B.V.*, 2024,
1332 preprint, DOI: 10.1016/j.apcatb.2023.123585.
- 1333 39 T. Amrillah, A. R. Supandi, V. Puspasari, A. Hermawan and Z. W. Seh, *Tianjin University*,
1334 2022, preprint, DOI: 10.1007/s12209-022-00328-9.
- 1335 40 J. Heo, N. Her, M. Jang, C. M. Park, A. Son, J. Han and Y. Yoon, *Taylor and Francis Ltd.*, 2023,
1336 preprint, DOI: 10.1080/10643389.2022.2101857.
- 1337 41 W. Wang, J. Wu, X. Chen, X. Shen, X. Jin, Y. Sun, C. Yan, Y. Li and P. Zhang, *Chem. Asian J.*,
1338 2025, **20**, e202500086.
- 1339 42 X. Q. Tan, W. Mo, X. Lin, J. Y. Loh, A. R. Mohamed and W. J. Ong, *Royal Society of Chemistry*,
1340 2023, preprint, DOI: 10.1039/d2nr05718b.
- 1341 43 B. Chang, H. Pang, F. Raziq, S. Wang, K. W. Huang, J. Ye and H. Zhang, *Energy Environ. Sci.*,
1342 2023, **16**, 4714–4758.
- 1343 44 K. Chan, *Nat. Commun.*, 2020, **11**, 1–4.



- 1344 45 J. Yu, J. Wang, Y. Ma, J. Zhou, Y. Wang, P. Lu, J. Yin, R. Ye, Z. Zhu, Z. Fan, J. Yu, J. Wang, Y.
1345 Ma, J. Zhou, Y. Wang, P. Lu, J. Yin, R. Ye, Z. Zhu, Z. Fan and Z. Fan Hong Kong Branch, *Adv.*
1346 *Funct. Mater.*, 2021, **31**, 2102151.
- 1347 46 Y. Y. Birdja, E. Pérez-Gallent, M. C. Figueiredo, A. J. Göttle, F. Calle-Vallejo and M. T. M.
1348 Koper, *Nat. Energy*, 2019, **4**, 732–745.
- 1349 47 W. Zhang, Y. Hu, L. Ma, G. Zhu, Y. Wang, X. Xue, R. Chen, S. Yang and Z. Jin, *Adv. Sci.*, 2018,
1350 **5**, 1700275.
- 1351 48 X. Zhi, A. Vasileff, Y. Zheng, Y. Jiao and S. Z. Qiao, *Energy Environ. Sci.*, 2021, **14**, 3912–3930.
- 1352 49 R.-B. Song, W. Zhu, J. Fu, Y. Chen, L. Liu, J.-R. Zhang, Y. Lin, J.-J. Zhu, R.-B. Song, J. Fu, Y.
1353 Chen, L. Liu, J.-R. Zhang, J.-J. Zhu, W. Zhu and Y. Lin, *Adv. Mater.*, 2020, **32**, 1903796.
- 1354 50 K. P. Kuhl, E. R. Cave, D. N. Abram and T. F. Jaramillo, *Energy Environ. Sci.*, 2012, **5**, 7050–
1355 7059.
- 1356 51 X. Li, X. Wu, X. Lv, J. Wang and H. Bin Wu, *Chem Catal.*, 2022, **2**, 262–291.
- 1357 52 Y. Yang, J. Wang, Y. Shu, Y. Ji, H. Dong and Y. Li, *Royal Society of Chemistry*, 2022, preprint,
1358 DOI: 10.1039/d1cp05442b.
- 1359 53 A. Ozden, F. P. García de Arquer, J. E. Huang, J. Wicks, J. Sisler, R. K. Miao, C. P. O'Brien, G.
1360 Lee, X. Wang, A. H. Ip, E. H. Sargent and D. Sinton, *Nat Sustain*, 2022, **5**, 563–573.
- 1361 54 D. Wakerley, S. Lamaison, J. Wicks, A. Clemens, J. Feaster, D. Corral, S. A. Jaffer, A. Sarkar,
1362 M. Fontecave, E. B. Duoss, S. Baker, E. H. Sargent, T. F. Jaramillo and C. Hahn, *Nat Energy*,
1363 2022, **7**, 130–143.



- 1364 55 B. Anasori and M. Naguib, *MRS Bull*, 2023, **48**, 238–244.
- 1365 56 A. D. Handoko, K. H. Khoo, T. L. Tan, H. Jin and Z. W. Seh, *J Mater Chem A Mater*, 2018, **6**,
1366 21885–21890.
- 1367 57 D. M. Feng, Y. P. Zhu, P. Chen and T. Y. Ma, *Catal.*, 2017, **7**, 373.
- 1368 58 J. He, N. J. J. Johnson, A. Huang and C. P. Berlinguette, *ChemSusChem*, 2018, **11**, 48–57.
- 1369 59 G. Marcandalli, M. C. O. Monteiro, A. Goyal and M. T. M. Koper, *Acc. Chem. Res.*, 2022, **55**,
1370 1900–1911.
- 1371 60 Y. Kang, S. M. João, R. Lin, K. Liu, L. Zhu, J. Fu, W. C. Cheong, S. Lee, K. Frank, B. Nickel, M.
1372 Liu, J. Lischner and E. Cortés, *Nat. Commun.*, 2024, **15**, 1–13.
- 1373 61 J.-J. Lv, R. Yin, L. Zhou, J. Li, R. Kikas, T. Xu, Z.-J. Wang, H. Jin, X. Wang and S. Wang, *Angew.*
1374 *Chem.*, 2022, **134**, e202207252.
- 1375 62 C. D. Koolen, W. Luo and A. Züttel, *ACS Catal.*, 2023, **13**, 948–973.
- 1376 63 X. Zhi, A. Vasileff, Y. Zheng, Y. Jiao and S. Z. Qiao, *Energy Environ. Sci.*, 2021, **14**, 3912–3930.
- 1377 64 B. Deng, M. Huang, X. Zhao, S. Mou and F. Dong, *ACS Catal.*, 2022, **12**, 331–362.
- 1378 65 L. Dong, W. Ge, Y. Fan, W. Zhang, H. Jiang, Y. Zhao and C. Li, *AIChE J.*, 2024, **70**, e18271.
- 1379 66 Y. J. Sa, C. W. Lee, S. Y. Lee, J. Na, U. Lee and Y. J. Hwang, *Chem. Soc. Rev.*, 2020, **49**, 6632–
1380 6665.
- 1381 67 J. Hou, B. Xu and Q. Lu, *Nat. Commun.*, 2024, **15**, 1–10.



- 1382 68 T. Luo, K. Liu, J. Fu, S. Chen, H. Li, H. Pan and M. Liu, *Adv. Energ. Sust. Res.*, 2023, **4**, 2200148.
- 1383 69 R. Gholizadeh, M. Pavlin, M. Huš and B. Likozar, *ChemSusChem*, 2025, **18**, e202400898.
- 1384 70 Y. Liu, Y. Song, L. Huang, J. Su, G. Li, Q. Zhang, Y. Xin, X. Cao, W. Guo, Y. Dou, M. He, T. Feng,
1385 Z. Jin and R. Ye, *ACS Nano*, 2024, **18**, 14020–14028.
- 1386 71 X. Zhang, S. X. Guo, K. A. Gandionco, A. M. Bond and J. Zhang, *Mater. Today Adv.*, 2020, **7**,
1387 100074.
- 1388 72 B. Miao, T. Bashir, H. Zhang, T. Ali, S. Raza, D. He, Y. Liu and J. Bai, *Renew. Sustain. Energy*
1389 *Rev.*, 2024, **199**, 114506.
- 1390 73 K. J. Harris, M. Bugnet, M. Naguib, M. W. Barsoum and G. R. Goward, *J. Phys. Chem. C*, 2015,
1391 **119**, 13713–13720.
- 1392 74 Y. Cheng, X. Xu, Y. Li, Y. Zhang and Y. Song, *Comput. Mater. Sci.*, 2022, **202**, 110971.
- 1393 75 C. Y. J. Lim, A. D. Handoko and Z. W. Seh, *Diam. relat. mater.*, 2022, **130**, 109461.
- 1394 76 K. Eid, Q. Lu, S. Abdel-Azeim, A. Soliman, A. M. Abdullah, A. M. Abdelgwad, R. P. Forbes, K.
1395 I. Ozoemena, R. S. Varma and M. F. Shibl, *J. Mater. Chem. A*, 2022, **10**, 1965–1975.
- 1396 77 Y. Zhang and Z. Cao, *J. Phys. Chem. C*, 2021, **125**, 13331–13342.
- 1397 78 S. Lu, Y. Zhang, F. Lou and Z. Yu, *J. CO2 Util.*, 2022, **62**, 102069.
- 1398 79 H. Bao, Y. Qiu, X. Peng, J. ao Wang, Y. Mi, S. Zhao, X. Liu, Y. Liu, R. Cao, L. Zhuo, J. Ren, J.
1399 Sun, J. Luo and X. Sun, *Nat. Commun.*, 2021, **12**, 1–9.



- 1400 80 S. Cao, H. Chen, Y. Hu, J. Li, C. Yang, Z. Chen, S. Wei, S. Liu, Z. Wang, D. Sun and X. Lu, *Chem.*
1401 *Eng. J.*, 2023, **461**, 141936.
- 1402 81 Y. Li, Y. Chen, Z. Guo, C. Tang, B. Sa, N. Miao, J. Zhou and Z. Sun, *Chem. Eng. J.*, 2022, **429**,
1403 132171.
- 1404 82 S. Krishnan, S. Marimuthu, M. K. Singh and D. K. Rai, *Energy Adv.*, 2023, **2**, 1166–1175.
- 1405 83 Z. Otgonbayar, C. M. Yoon and W. C. Oh, *Chem. Eng. J.*, 2023, **464**, 142716.
- 1406 84 D. Qu, X. Peng, Y. Mi, H. Bao, S. Zhao, X. Liu and J. Luo, *Nanoscale*, 2020, **12**, 17191–17195.
- 1407 85 F. Zhang and A. C. Co, *Angew. Chem. Int. Ed.*, 2020, **59**, 1674–1681.
- 1408 86 M. Dunwell, X. Yang, B. P. Setzler, J. Anibal, Y. Yan and B. Xu, *ACS Catal.*, 2018, **8**, 3999–
1409 4008.
- 1410 87 A. S. Varela, M. Kroschel, T. Reier and P. Strasser, *Catal. Today*, 2016, **260**, 8–13.
- 1411 88 Z. Xie, Q. Wang, R. Yang, J. Zhang, S. Ou, G. Ouyang, M. Li, J. Shi and Y. Tong, *Appl. Catal. B:*
1412 *Environ.*, 2025, **362**, 124727.
- 1413 89 X. Liu, P. Schlexer, J. Xiao, Y. Ji, L. Wang, R. B. Sandberg, M. Tang, K. S. Brown, H. Peng, S.
1414 Ringe, C. Hahn, T. F. Jaramillo, J. K. Nørskov and K. Chan, *Nat. Commun.*, 2019, **10**, 1–10.
- 1415 90 J. Shen, R. Kortlever, R. Kas, Y. Y. Birdja, O. Diaz-Morales, Y. Kwon, I. Ledezma-Yanez, K. J.
1416 P. Schouten, G. Mul and M. T. M. Koper, *Nat. Commun.*, 2015, **6**, 1–8.
- 1417 91 M. López, K. S. Exner, F. Viñes and F. Illas, *Adv. Theory Simul.*, 2023, **6**, 2200217.
- 1418 92 G. Gao, A. P. O'Mullane and A. Du, *ACS Catal.*, 2017, **7**, 494–500.



- 1419 93 L. R. Johnson, S. Sridhar, L. Zhang, K. D. Fredrickson, A. S. Raman, J. Jang, C. Leach, A.
1420 Padmanabhan, C. C. Price, N. C. Frey, A. Raizada, V. Rajaraman, S. A. Saiprasad, X. Tang and
1421 A. Vojvodic, *ACS Catal.*, 2020, **10**, 253–264.
- 1422 94 L. D. Chen, M. Urushihara, K. Chan and J. K. Nørskov, *ACS Catal.*, 2016, **6**, 7133–7139.
- 1423 95 M. R. Singh, Y. Kwon, Y. Lum, J. W. Ager and A. T. Bell, *J. Am. Chem. Soc.*, 2016, **138**, 13006–
1424 13012.
- 1425 96 A. Murata and Y. Hori, *Bull. Chem. Soc. Jpn.*, 1991, **64**, 123–127.
- 1426 97 S. Li, X. Dong, Y. Zhao, J. Mao, W. Chen, A. Chen, Y. Song, G. Li, Z. Jiang, W. Wei and Y. Sun,
1427 *Angew. Chem. Int. Ed.*, 2022, **61**, e202210432.
- 1428 98 I. T. McCrum, S. A. Akhade and M. J. Janik, *Electrochim. Acta.*, 2015, **173**, 302–309.
- 1429 99 J. J. Masana, B. Peng, Z. Shuai, M. Qiu and Y. Yu, *J. Mater. Chem. A*, 2022, **10**, 1086–1104.
- 1430 100 Y. J. Ko, J. Y. Kim, W. H. Lee, M. G. Kim, T. Y. Seong, J. Park, Y. J. Jeong, B. K. Min, W. S. Lee,
1431 D. K. Lee and H. S. Oh, *Nat. Commun.*, 2022, **13**, 1–9.
- 1432 101 W. Ni, Y. Xue, X. Zang, C. Li, H. Wang, Z. Yang and Y. M. Yan, *ACS Nano*, 2020, **14**, 2014–
1433 2023.
- 1434 102 D. Gao, F. Scholten and B. Roldan Cuenya, *ACS Catal.*, 2017, **7**, 5112–5120.
- 1435 103 R. A. Vaia, A. Jawaid, A. Hassan, G. Neher, D. Nepal, R. Pachter, W. Joshua Kennedy and S.
1436 Ramakrishnan, *ACS Nano*, 2021, **15**, 2771–2777.



- 1437 104 T. Zhang, L. Chang, X. Zhang, H. Wan, N. Liu, L. Zhou and X. Xiao, *Nat. Commun.*, 2022, **13**,
1438 1–9.
- 1439 105 Y. Li, H. Shao, Z. Lin, J. Lu, L. Liu, B. Duployer, P. O. Å. Persson, P. Eklund, L. Hultman, M. Li,
1440 K. Chen, X. H. Zha, S. Du, P. Rozier, Z. Chai, E. Raymundo-Piñero, P. L. Taberna, P. Simon and
1441 Q. Huang, *Nat. Mater.*, 2020, **19**, 894–899.
- 1442 106 Q. Zhao, C. Zhang, R. Hu, Z. Du, J. Gu, Y. Cui, X. Chen, W. Xu, Z. Cheng, S. Li, B. Li, Y. Liu, W.
1443 Chen, C. Liu, J. Shang, L. Song and S. Yang, *ACS Nano*, 2021, **15**, 4927–4936.
- 1444 107 A. Gennaro, A. A. Isse and E. Vianello, *J. Electroanal. Chem.*, 1990, **289**, 203–215.
- 1445 108 A. D. Handoko, H. Chen, Y. Lum, Q. Zhang, B. Anasori and Z. W. Seh, *iScience*, 2020, **23**,
1446 101181.
- 1447 109 N. H. Attanayake, H. R. Banjade, A. C. Thenuwara, B. Anasori, Q. Yan and D. R. Strongin,
1448 *Chem. Commun.*, 2021, **57**, 1675–1678.
- 1449 110 X. Liao, K. Zheng, G. Wang, Y. Yang, Y. Li and M. O. Coppens, *Ind. Eng. Chem. Res.*, 2022, **61**,
1450 14364–14373.
- 1451 111 Z. Lin, D. Barbara, P. L. Taberna, K. L. Van Aken, B. Anasori, Y. Gogotsi and P. Simon, *J. Power*
1452 *Sources*, 2016, **326**, 575–579.
- 1453 112 Q. Fan, R. Zhao, M. Yi, P. Qi, C. Chai, H. Ying and J. Hao, *Chem. Eng. J.*, 2022, **428**, 131107.
- 1454 113 Z. Wang, J. Chen, Y. Li, K. Dong and Y. Yu, *Phys. Chem. Chem. Phys.*, 2022, **24**, 5903–5913.
- 1455 114 X. Sun, Y. Li, Y. Wang, Z. Liu, K. Dong and S. Zhang, *Langmuir*, 2024, **40**, 2220–2229.



- 1456 115 Z. Gu, H. Shen, L. Shang, X. Lv, L. Qian, G. Zheng, Z. Gu, H. Shen, L. Shang, X. Lv, L. Qian and
1457 G. Zheng, *Small Methods*, 2018, **2**, 1800121.
- 1458 116 H. Xie, T. Wang, J. Liang, Q. Li and S. Sun, *Nano Today*, 2018, **21**, 41–54.
- 1459 117 X. Ma, Y. Zhang, T. Fan, D. Wei, Z. Huang, Z. Zhang, Z. Zhang, Y. Dong, Q. Hong, Z. Chen, X.
1460 Yi, X. Ma, T. Fan, D. Wei, Z. Huang, Q. Hong, X. Yi, Y. Zhang, Z. Zhang, Z. Chen and Y. Dong,
1461 *Adv. Funct. Mater.*, 2023, **33**, 2213145.
- 1462 118 H. Luo, B. Li, J. G. Ma and P. Cheng, *Angew. Chem. Int. Ed.*, 2022, **61**, e202116736.
- 1463 119 G. L. De Gregorio, T. Burdyny, A. Loiudice, P. Iyengar, W. A. Smith and R. Buonsanti, *ACS*
1464 *Catal.*, 2020, **10**, 4854–4862.
- 1465 120 N. Li, X. Chen, W. J. Ong, D. R. Macfarlane, X. Zhao, A. K. Cheetham and C. Sun, *ACS Nano*,
1466 2017, **11**, 10825–10833.
- 1467 121 L. Han, X. Peng, H. T. Wang, P. Ou, Y. Mi, C. W. Pao, J. Zhou, J. Wang, X. Liu, W. F. Pong, J.
1468 Song, Z. Lin, J. Luo and H. L. Xin, *PNAS*, 2022, **119**, e2207326119.
- 1469 122 B. Govindan, R. Madhu, M. Abu Haija, F. V. Kusmartsev and F. Banat, *Catal.*, 2022, **12**, 1180.
- 1470 123 J. Lin, Y. Zhang, P. Xu and L. Chen, *MRE*, 2023, **3**, 100194.
- 1471 124 S. Varhade, A. Gurujji, C. Singh, G. Cicero, M. García-Melchor, J. Helsen and D. Pant,
1472 *ChemElectroChem*, 2025, **12**, e202400512.
- 1473 125 M. Gao, Y. Sun, K. Zhao, M. Zhang, X. Wang and W. Wang, *J. Environ. Chem. Eng.*, 2024, **12**,
1474 111802.



- 1475 126 Z. Han, Y. Chang, H. Liu, Y. Wei, S. Hao, M. Y. Cong, Y. Gao and J. Gao, *Adv. Energy Mater.*,
1476 2025, 2501761.
- 1477 127 M. Abdinejad, S. Subramanian, K. Motlagh, M. Noroozifar, S. Duangdangchote, I.
1478 Neporozhnii, D. Ripepi, D. Pinto, M. Li, K. Tang, J. Middelkoop, A. Urakawa, O. Voznyy, H.-
1479 B. Kraatz, T. Burdyny, M. Abdinejad, S. Subramanian, D. Ripepi, D. Pinto, M. Li, J.
1480 Middelkoop, A. Urakawa, T. Burdyny, M. K. Motlagh, M. Noroozifar, S. Duangdangchote, I.
1481 Neporozhnii, K. Tang, O. Voznyy and H.-B. Kraatz, *Adv. Energy Mater.*, 2023, **13**, 2300402.
- 1482 128 M. Krishnan, A. Vijayaprabhakaran and M. Kathiresan, *Nanoscale*, 2024, **16**, 16218–16226.
- 1483 129 M. Naguib, M. W. Barsoum, Y. Gogotsi, M. Naguib, M. W. Barsoum, Y. Gogotsi and A. Y. J.
1484 Gogotsi, *Adv. Mater.*, 2021, **33**, 2103393.
- 1485 130 R. Khaledialidusti, M. Khazaei, S. Khazaei and K. Ohno, *Nanoscale*, 2021, **13**, 7294–7307.
- 1486 131 M. Dahlgqvist, A. Petruhins, J. Lu, L. Hultman and J. Rosen, *ACS Nano*, 2018, **12**, 7761–7770.
- 1487 132 T. S. Mathis, K. Maleski, A. Goad, A. Sarycheva, M. Anayee, A. C. Foucher, K.
1488 Hantanasirisakul, C. E. Shuck, E. A. Stach and Y. Gogotsi, *ACS Nano*, 2021, **15**, 6420–6429.
- 1489 133 J. Peng, X. Chen, W. J. Ong, X. Zhao and N. Li, *Chem*, 2019, **5**, 18–50.
- 1490 134 P. P. Michałowski, M. Anayee, T. S. Mathis, S. Kozdra, A. Wójcik, K. Hantanasirisakul, I.
1491 Józwiak, A. Piątkowska, M. Możdżonek, A. Malinowska, R. Diduszko, E. Wierzbička and Y.
1492 Gogotsi, *Nat. Nanotechnol.*, 2022, **17**, 1192–1197.
- 1493 135 C. E. Shuck, M. Han, K. Maleski, K. Hantanasirisakul, S. J. Kim, J. Choi, W. E. B. Reil and Y.
1494 Gogotsi, *ACS Appl. Nano Mater*, 2019, **2**, 3368–3376.



- 1495 136 M. Naguib, M. Kurtoglu, V. Presser, J. Lu, J. Niu, M. Heon, L. Hultman, Y. Gogotsi and M. W.
1496 Barsoum, *Adv. Mater.*, 2011, **23**, 4248–4253.
- 1497 137 Y. J. Kim, S. J. Kim, D. Seo, Y. Chae, M. Anayee, Y. Lee, Y. Gogotsi, C. W. Ahn and H. T. Jung,
1498 *Chem. Mater.*, 2021, **33**, 6346–6355.
- 1499 138 K. Hantanasirisakul, Y. Gogotsi, K. Y. Hantanasirisakul and A. J. Gogotsi, *Adv. Mater.*, 2018,
1500 **30**, 1804779.
- 1501 139 J. L. Hart, K. Hantanasirisakul, A. C. Lang, B. Anasori, D. Pinto, Y. Pivak, J. T. van Omme, S. J.
1502 May, Y. Gogotsi and M. L. Taheri, *Nat. Commun.*, 2019, **10**, 1–10.
- 1503 140 M. Anayee, N. Kurra, M. Alhabeb, M. Seredych, M. N. Hedhili, A. H. Emwas, H. N. Alshareef,
1504 B. Anasori and Y. Gogotsi, *Chem. Commun.*, 2020, **56**, 6090–6093.
- 1505 141 N. Driscoll, A. G. Richardson, K. Maleski, B. Anasori, O. Adewole, P. Lelyukh, L. Escobedo, D.
1506 K. Cullen, T. H. Lucas, Y. Gogotsi and F. Vitale, *ACS Nano*, 2018, **12**, 10419–10429.
- 1507 142 C. E. Shuck, A. Sarycheva, M. Anayee, A. Levitt, Y. Zhu, S. Uzun, V. Balitskiy, V. Zahorodna,
1508 O. Gogotsi and Y. Gogotsi, *Adv. Eng. Mater.*, 2020, **22**, 1901241.
- 1509 143 A. Thakur, Y. Zhang, Y. Gogotsi and B. Anasori, *MRS Energy Sustain.*, 2025, 1–13.
- 1510 144 M. R. Lukatskaya, J. Halim, B. Dyatkin, M. Naguib, Y. S. Buranova, M. W. Barsoum, Y.
1511 Gogotsi, J. M. R. Lukatskaya, J. Halim, B. Dyatkin, M. Naguib, Y. S. Buranova, + M. W. Barsoum
1512 and A. Y. J. Gogotsi, *Angew. Chem. Int. Ed.*, 2014, **53**, 4877–4880.
- 1513 145 S. Y. Pang, Y. T. Wong, S. Yuan, Y. Liu, M. K. Tsang, Z. Yang, H. Huang, W. T. Wong and J.
1514 Hao, *J. Am. Chem. Soc.*, 2019, **141**, 9610–9616.



- 1515 146 W. Sun, S. A. Shah, Y. Chen, Z. Tan, H. Gao, T. Habib, M. Radovic and M. J. Green, *J. Mater.*
1516 *Chem. A*, 2017, **5**, 21663–21668.
- 1517 147 J. Chen, M. Chen, W. Zhou, X. Xu, B. Liu, W. Zhang and C. Wong, *ACS Nano*, 2022, **16**, 2461–
1518 2470.
- 1519 148 M. Shen, W. Jiang, K. Liang, S. Zhao, R. Tang, L. Zhang and J. Q. Wang, *Angew. Chem. Int.*
1520 *Ed.*, 2021, **60**, 27013–27018.
- 1521 149 L. Li, G. Li, L. Tan, Y. Zhang and B. Wu, *Langmuir*, 2017, **33**, 9000–9006.
- 1522 150 T. Li, L. Yao, Q. Liu, J. Gu, R. Luo, J. Li, X. Yan, W. Wang, P. Liu, B. Chen, W. Zhang, W. Abbas,
1523 R. Naz and D. Zhang, *Angew. Chem. Int. Ed.*, 2018, **57**, 6115–6119.
- 1524 151 M. Sun, A. Staykov and M. Yamauchi, *ACS Catal.*, 2022, **12**, 14856–14863.
- 1525 152 M. Luo, Z. Wang, Y. C. Li, J. Li, F. Li, Y. Lum, D. H. Nam, B. Chen, J. Wicks, A. Xu, T. Zhuang,
1526 W. R. Leow, X. Wang, C. T. Dinh, Y. Wang, Y. Wang, D. Sinton and E. H. Sargent, *Nat.*
1527 *Commun.*, 2019, **10**, 1–7.
- 1528 153 M. A. Z. G. Sial, M. Abbas, Z. M. Bhat, S. Ligani, M. Furquan, U. Alam, A. Hussain, X. Cai and
1529 M. Qamar, *Next Energy*, 2024, **4**, 100139.
- 1530 154 M. Ghidui, M. R. Lukatskaya, M. Q. Zhao, Y. Gogotsi and M. W. Barsoum, *Nat.*, 2014, **516**,
1531 78–81.
- 1532 155 F. Liu, A. Zhou, J. Chen, J. Jia, W. Zhou, L. Wang and Q. Hu, *Appl. Surf. Sci.*, 2017, **416**, 781–
1533 789.



- 1534 156 X. Wang, Y. Shi, J. Qiu, Z. Wang, R. Li, / Chemcomm and C. Communication, *Chem.*
1535 *Commun.*, 2023, **59**, 5063–5066.
- 1536 157 M. Li, J. Lu, K. Luo, Y. Li, K. Chang, K. Chen, J. Zhou, J. Rosen, L. Hultman, P. Eklund, P. O. Å.
1537 Persson, S. Du, Z. Chai, Z. Huang and Q. Huang, *J. Am. Chem. Soc.*, 2019, **141**, 4730–4737.
- 1538 158 V. Kamysbayev, A. S. Filatov, H. Hu, X. Rui, F. Lagunas, D. Wang, R. F. Klie and D. V. Talapin,
1539 *Sci.*, 2020, **369**, 979–983.
- 1540 159 L. Liu, E. Raymundo-Piñero, P. L. Taberna and P. Simon, *Electrochem. Commun.*, 2023, **148**,
1541 107453.
- 1542 160 C. Wang, H. Shou, S. Chen, S. Wei, Y. Lin, P. Zhang, Z. Liu, K. Zhu, X. Guo, X. Wu, P. M. Ajayan,
1543 L. Song, C. Wang, H. Shou, S. Chen, S. Wei, Y. Lin, P. Zhang, Z. Liu, K. Zhu, X. Guo, L. Song, X.
1544 Wu and P. M. Ajayan, *Adv. Mater.*, 2021, **33**, 2101015.
- 1545 161 E. M. López-Alejandro, E. Ramírez-Morales, M. C. Arellano-Cortaza, C. A. Meza-Avendaño,
1546 D. M. Frías-Márquez, R. Ramírez-Bon and L. Rojas-Blanco, *Ceram. Int.*,
1547 DOI:10.1016/J.CERAMINT.2025.02.028.
- 1548 162 F. N. M. Azlan, M. A. A. M. Abdah, Y. S. Tan, M. N. Mustafa, R. Walvekar and M. Khalid, *J.*
1549 *Energy Storage*, 2023, **72**, 108620.
- 1550 163 A. Numan, S. Rafique, M. Khalid, H. A. Zaharin, A. Radwan, N. A. Mokri, O. P. Ching and R.
1551 Walvekar, *Mater. Chem. Phys.*, 2022, **288**, 126429.
- 1552 164 C. Xu, L. Wang, Z. Liu, L. Chen, J. Guo, N. Kang, X. L. Ma, H. M. Cheng and W. Ren, *Nat.*
1553 *Mater.*, 2015, **14**, 1135–1141.



- 1554 165 D. Wang, C. Zhou, A. S. Filatov, W. Cho, F. Lagunas, M. Wang, S. Vaikuntanathan, C. Liu, R.
1555 F. Klie and D. V. Talapin, *Sci.*, 2023, **379**, 1242–1247.
- 1556 166 S. Joshi, Q. Wang, A. Puntambekar and V. Chakrapani, *ACS Energy Lett.*, 2017, **2**, 1257–
1557 1262.
- 1558 167 X. Xiao, H. Yu, H. Jin, M. Wu, Y. Fang, J. Sun, Z. Hu, T. Li, J. Wu, L. Huang, Y. Gogotsi and J.
1559 Zhou, *ACS Nano*, 2017, **11**, 2180–2186.
- 1560 168 Z. Zhang, F. Zhang, H. Wang, C. Ho Chan, W. Lu and J. Y. Dai, *J. Mater. Chem. C*, 2017, **5**,
1561 10822–10827.
- 1562 169 M. Xiang, Z. Shen, J. Zheng, M. Song, Q. He, Y. Yang, J. Zhu, Y. Geng, F. Yue, Q. Dong, Y. Ge,
1563 R. Wang, J. Wei, W. Wang, H. Huang, H. Zhang, Q. Zhu and C. J. Zhang, *The Innovation*, 2024,
1564 **5**, 100540.
- 1565 170 Y. Li, H. Shao, Z. Lin, J. Lu, L. Liu, B. Duployer, P. O. Å. Persson, P. Eklund, L. Hultman, M. Li,
1566 K. Chen, X. H. Zha, S. Du, P. Rozier, Z. Chai, E. Raymundo-Piñero, P. L. Taberna, P. Simon and
1567 Q. Huang, *Nat. Mater.*, 2020, **19**, 894–899.
- 1568 171 A. Thakur, N. Chandran B.S., K. Davidson, A. Bedford, H. Fang, Y. Im, V. Kanduri, B. C. Wyatt,
1569 S. K. Nemani, V. Poliukhova, R. Kumar, Z. Fakhraai and B. Anasori, *Small Methods*, 2023, **7**,
1570 2300030.
- 1571 172 Y. Wei, P. Zhang, R. A. Soomro, Q. Zhu, B. Xu, Y. Wei, P. Zhang, R. A. Soomro, Q. Zhu and B.
1572 Xu, *Adv. Mater.*, 2021, **33**, 2103148.
- 1573 173 O. Mashtalir, M. Naguib, V. N. Mochalin, Y. Dall’Agnese, M. Heon, M. W. Barsoum and Y.
1574 Gogotsi, *Nat. Commun.*, 2013, **4**, 1–7.



- 1575 174 M. Naguib, R. R. Unocic, B. L. Armstrong and J. Nanda, *Dalton Trans.*, 2015, **44**, 9353–9358.
- 1576 175 F. Han, S. Luo, L. Xie, J. Zhu, W. Wei, X. Chen, F. Liu, W. Chen, J. Zhao, L. Dong, K. Yu, X. Zeng,
- 1577 F. Rao, L. Wang and Y. Huang, *ACS Appl. Mater. Interfaces.*, 2019, **11**, 8443–8452.
- 1578 176 K. Montazeri, H. Badr, K. Ngo, K. Sudhakar, T. Elmelegy, J. Uzarski, V. Natu and M. W.
- 1579 Barsoum, *J. Phys. Chem. C*, 2023, **127**, 10391–10397.
- 1580 177 O. Mashtalir, M. R. Lukatskaya, M.-Q. Zhao, M. W. Barsoum, Y. Gogotsi, O. Mashtalir, M. R.
- 1581 Lukatskaya, M. Zhao, M. W. Barsoum and Y. Gogotsi, *Adv. Mater.*, 2015, **27**, 3501–3506.
- 1582 178 T. Zhang, K. Shevchuk, R. J. Wang, H. Kim, J. Hourani and Y. Gogotsi, *Chem. Mater.*, 2024,
- 1583 **36**, 1998–2006.
- 1584 179 L. Liu, M. Orbay, S. Luo, S. Duluard, H. Shao, J. Harmel, P. Rozier, P. L. Taberna and P. Simon,
- 1585 *ACS Nano*, 2022, **16**, 111–118.
- 1586 180 M. Ghidui, J. Halim, S. Kota, D. Bish, Y. Gogotsi and M. W. Barsoum, *Chem. Mater.*, 2016,
- 1587 **28**, 3507–3514.
- 1588 181 H. Song, Y. Ma, Q. Yao, C. Liu, X. Li and X. Tao, *Chem. Eng. J.*, 2024, **491**, 151909.
- 1589 182 D. D. Kruger, H. García and A. Primo, *Adv. Sci.*, 2024, **11**, 2307106.
- 1590 183 Z. Zhang, Y. Ji, Q. Jiang and C. Xia, *Chem. Phys. Rev.*, DOI:10.1063/5.0215613.
- 1591 184 D. Gandla, Z. Zhuang, V. V. Jadhav and D. Q. Tan, *Energy Storage Mater.*, 2023, **63**, 102977.
- 1592 185 X. Shi, Z. Yu, Z. Liu, N. Cao, L. Zhu, Y. Liu, K. Zhao, T. Shi, L. Yin and Z. Fan, *Angew. Chem.*,
- 1593 2025, **137**, e202418420.



- 1594 186 K. R. G. Lim, M. Shekhirev, B. C. Wyatt, B. Anasori, Y. Gogotsi and Z. W. Seh, *Nat. Synth.*,
1595 2022, **1**, 601–614.
- 1596 187 C. E. Shuck, A. Sarycheva, M. Anayee, A. Levitt, Y. Zhu, S. Uzun, V. Balitskiy, V. Zahorodna,
1597 O. Gogotsi and Y. Gogotsi, *Adv. Eng. Mater.*, 2020, **22**, 1901241.
- 1598 188 M. Shekhirev, J. Busa, C. E. Shuck, A. Torres, S. Bagheri, A. Sinitskii and Y. Gogotsi, *ACS Nano*,
1599 2022, **16**, 13695–13703.
- 1600 189 P. D. Kolubah, H. O. Mohamed, A. R. Hari, Y. Ping, M. Ben Hassine, P. Dally, M. Obaid, X. Xu,
1601 J. K. El-Demellawi, P. E. Saikaly, M. Lanza, N. Ghaffour and P. Castaño, *Small*, 2024, 2406223.
- 1602 190 W. Cao, J. Nie, Y. Cao, C. Gao, M. Wang, W. Wang, X. Lu, X. Ma and P. Zhong, *Chem. Eng. J.*,
1603 2024, **496**, 154097.
- 1604 191 G. Murali, J. K. Reddy Modigunta, Y. H. Park, J. H. Lee, J. Rawal, S. Y. Lee, I. In and S. J. Park,
1605 *ACS Nano*, 2022, **16**, 13370–13429.
- 1606 192 C. Rong, T. Su, Z. Li, T. Chu, M. Zhu, Y. Yan, B. Zhang and F. Z. Xuan, *Nat. Commun*, 2024,
1607 **15**, 1–8.
- 1608 193 A. Lipatov, S. Bagheri and A. Sinitskii, *ACS Mater. Lett.*, 2024, **6**, 298–307.
- 1609 194 Z. Ling, C. E. Ren, M. Q. Zhao, J. Yang, J. M. Giammarco, J. Qiu, M. W. Barsoum and Y.
1610 Gogotsi, *PNAS*, 2014, **111**, 16676–16681.
- 1611 195 Y. Z. Zhang, J. K. El-Demellawi, Q. Jiang, G. Ge, H. Liang, K. Lee, X. Dong and H. N. Alshareef,
1612 *Chem. Soc. Rev.*, 2020, **49**, 7229–7251.



- 1613 196 C. Rong, T. Su, Z. Li, T. Chu, M. Zhu, Y. Yan, B. Zhang and F.-Z. Xuan, *Nat Commun*, 2024, **15**,
1614 1566.
- 1615 197 A. Lipatov, H. Lu, M. Alhabeb, B. Anasori, A. Gruverman, Y. Gogotsi and A. Sinitskii, *Sci Adv*,
1616 DOI:10.1126/sciadv.aat0491.
- 1617 198 B. C. Wyatt, S. K. Nemani, K. Desai, H. Kaur, B. Zhang and B. Anasori, *J. Phys. Condens.*
1618 *Matter.*, 2021, **33**, 224002.
- 1619 199 Y. Xie and P. R. C. Kent, *Phys Rev B Condens Matter Mater Phys*, 2013, **87**, 235441.
- 1620 200 R. A. Soomro, P. Zhang, B. Fan, Y. Wei and B. Xu, *Nanomicro Lett.*, 2023, **15**, 1–18.
- 1621 201 X. Liu, L. Yao, S. Zhang, C. Huang and W. Yang, *Inorg. Chem.*, 2024, **63**, 6305–6314.
- 1622 202 K. Huang, P. Qu, Y. Wang, C. Lian, J. Li, H. Su and H. Liu, *Ind. Eng. Chem. Res.*, 2023, **62**,
1623 20716–20726.
- 1624 203 H. Chen, A. D. Handoko, T. Wang, J. Qu, J. Xiao, X. Liu, D. Legut, Z. Wei Seh and Q. Zhang,
1625 *ChemSusChem*, 2020, **13**, 5690–5698.
- 1626 204 C. Y. J. Lim, A. D. Handoko and Z. W. Seh, *Diam Relat Mater*, 2022, **130**, 109461.
- 1627 205 H. Chen, A. D. Handoko, J. Xiao, X. Feng, Y. Fan, T. Wang, D. Legut, Z. W. Seh and Q. Zhang,
1628 *ACS Appl. Mater. Interfaces.*, 2019, **11**, 36571–36579.
- 1629 206 A. Parui, P. Srivastava and A. K. Singh, *ACS Appl Mater Interfaces*, 2022, **14**, 40913–40920.
- 1630 207 L. Meng, L. K. Yan, F. Viñes and F. Illas, *J. Mater. Chem. A.*, 2024, **12**, 7856–7874.



- 1631 208 A. D. Handoko, K. D. Fredrickson, B. Anasori, K. W. Convey, L. R. Johnson, Y. Gogotsi, A.
1632 Vojvodic and Z. W. Seh, *ACS Appl Energy Mater*, 2018, **1**, 173–180.
- 1633 209 A. D. Handoko, H. Chen, Y. Lum, Q. Zhang, B. Anasori and Z. W. Seh, *iScience*, 2020, **23**,
1634 101181.
- 1635 210 J. Low, L. Zhang, T. Tong, B. Shen and J. Yu, *J. Catal.*, 2018, **361**, 255–266.
- 1636 211 V. Parey, B. M. Abraham, M. V. Jyothirmai and J. K. Singh, *Catal. Sci. Technol.*, 2022, **12**,
1637 2223–2231.
- 1638 212 A. D. Handoko, K. H. Khoo, T. L. Tan, H. Jin and Z. W. Seh, *J. Mater. Chem. A.*, 2018, **6**, 21885–
1639 21890.
- 1640 213 S. Cao, Y. Liu, Y. Hu, J. Li, C. Yang, Z. Chen, Z. Wang, S. Wei, S. Liu and X. Lu, *J. Colloid Interface*
1641 *Sci.*, 2023, **642**, 273–282.
- 1642 214 X. Wu, Y. Wang and Z. S. Wu, *iScience*, 2024, **27**, 108906.
- 1643 215 Y. Zhou, Y. Wang, Y. Wang and X. Li, *Anal. Chem.*, 2020, **92**, 16033–16042.
- 1644 216 B. Miao, T. Bashir, H. Zhang, T. Ali, S. Raza, D. He, Y. Liu and J. Bai, *Renew. Sustain. Energy*
1645 *Rev.*, 2024, **199**, 114506.
- 1646 217 E. Rems, Y. J. Hu, Y. Gogotsi and R. Dominko, *Chem. Mater.*, 2024, **36**, 10295–10306.
- 1647 218 A. Miranda, J. Halim, A. Lorke and M. W. Barsoum, *Mater. Res. Lett.*, 2017, **5**, 322–328.
- 1648 219 L. Meng, L. K. Yan, F. Viñes and F. Illas, *J. Mater. Chem. A.*, 2024, **12**, 7856–7874.



- 1649 220 Y. Sun, R. Yu, J. Sun, D. Legut, J. S. Francisco and R. Zhang, *J. Mater. Chem. A.*,
1650 DOI:10.1039/D4TA06969B.
- 1651 221 Y. Shi, B. Wei, D. Legut, S. Du, J. S. Francisco and R. Zhang, *Adv. Funct. Mater.*, 2022, **32**,
1652 2210218.
- 1653 222 Y. Wang, R. Du, Z. Li, H. Song, Z. Chao, D. Zu, D. Chong, N. Gao and C. Li, *Ceram. Int.*, 2021,
1654 **47**, 28321–28327.
- 1655 223 M. H. Sliem, K. Kannan, M. R. Maurya, K. Jlassi, K. K. Sadasivuni, B. Kumar and A. M.
1656 Abdullah, *Top. Catal.*, 2022, **1**, 1–16.
- 1657 224 Y. Hao, F. Hu, S. Zhu, Y. Sun, H. Wang, L. Wang, Y. Wang, J. Xue, Y. F. Liao, M. Shao and S.
1658 Peng, *Angew. Chem. Int. Ed.*, 2023, **62**, e202304179.
- 1659 225 K. Kannan, M. H. Sliem, A. M. Abdullah, K. K. Sadasivuni and B. Kumar, *Catal.*, 2020, **10**, 549.
- 1660 226 P. K. Jiwanti, A. M. Alfaza, G. T. M. Kadja, S. A. C. Natalya, F. Sagita, Y. Einaga, A.
1661 Purwaningsih, I. Amalina and I. N. Rizki, *Energies (Basel)*, 2023, **16**, 4537.
- 1662 227 Y. Sun, R. Yu, J. Sun, D. Legut, J. S. Francisco and R. Zhang, *J. Mater. Chem. A*,
1663 DOI:10.1039/D4TA06969B.
- 1664 228 Z. Li, N. H. Attanayake, J. L. Blackburn and E. M. Miller, *Energy Environ. Sci.*, 2021, **14**, 6242–
1665 6286.
- 1666 229 Y. Wang, J. Shui, Y. Jia, H. Zhang, W. Cen, S. Tang and Y. Han, *Chem. Eng. J.*, 2025, **507**,
1667 160716.



- 1668 230 Z. W. Seh, K. D. Fredrickson, B. Anasori, J. Kibsgaard, A. L. Strickler, M. R. Lukatskaya, Y.
1669 Gogotsi, T. F. Jaramillo and A. Vojvodic, *ACS Energy Lett.*, 2016, **1**, 589–594.
- 1670 231 J. Zhang, Y. Zhao, X. Guo, C. Chen, C. L. Dong, R. S. Liu, C. P. Han, Y. Li, Y. Gogotsi and G.
1671 Wang, *Nat. Cat.*, 2018, **1**, 985–992.
- 1672 232 J. Yu, Y. Zeng, J. Chen, K. Tan and W. Lin, *J. Colloid Interface Sci.*, 2025, **697**, 137961.
- 1673 233 H.-H. Cao, Z.-H. He, P.-P. Guo, Y. Tian, X. Wang, K. Wang, W. Wang, H. Wang, Y. Yang and
1674 Z.-T. Liu, *ChemCatChem*, 2025, **17**, e202401133.
- 1675 234 W. Wu, H. Bi, Z. Zhang, L. Sun, R. Wei, L. Gao, X. Pan, J. Zhang and G. Xiao, *Colloids Surf. A:*
1676 *Physicochem. Eng. Asp.*, 2023, **657**, 130486.
- 1677 235 A. Athawale, B. M. Abraham, M. V. Jyothirmai and J. K. Singh, *J. Phys. Chem. C.*, 2023, **127**,
1678 24542–24551.
- 1679 236 B. Miao, T. Bashir, H. Zhang, T. Ali, S. Raza, D. He, Y. Liu and J. Bai, *Renew. Sustain. Energy*
1680 *Rev.*, 2024, **199**, 114506.
- 1681 237 L. Meng, L. K. Yan, F. Viñes and F. Illas, *J. Mater. Chem. A.*, 2023, **11**, 6886–6900.
- 1682 238 D. D. Kruger, J. J. Delgado, F. J. Recio, S. Goberna-Ferron, A. Primo and H. Garcia, *J. Mater.*
1683 *Chem. A.*, 2024, **12**, 25291–25303.
- 1684 239 X. An and D. Yang, *Nanoscale*, 2025, **17**, 4212–4225.
- 1685 240 E. J. Jelmy, N. Thomas, D. T. Mathew, J. Louis, N. T. Padmanabhan, V. Kumaravel, H. John
1686 and S. C. Pillai, *React. Chem. Eng.*, 2021, **6**, 1701–1738.



- 1687 241 H. Jin, T. Song, U. Paik and S. Z. Qiao, *Acc. Mater. Res.*, 2021, **2**, 559–573.
- 1688 242 X. Chia and M. Pumera, *Nat. Catal.*, 2018, **1**, 909–921.
- 1689 243 S. Xiao, Y. Zheng, X. Wu, M. Zhou, X. Rong, L. Wang, Y. Tang, X. Liu, L. Qiu and C. Cheng,
1690 *Small*, 2022, **18**, 2203281.
- 1691 244 G. Wei, Z. Mao, L. Liu, T. Hao, L. Zhu, S. Xu, X. Wang and S. Tang, *ACS Appl. Mater.*
1692 *Interfaces.*, 2024, **16**, 52233–52243.
- 1693 245 Q. Tang, T. Li, W. Tu, H. Wang, Y. Zhou and Z. Zou, *Adv. Funct. Mater.*, 2024, **34**, 2311609.
- 1694 246 L. Li, *Comput. Mater. Sci.*, 2016, **124**, 8–14.
- 1695 247 C. Lu, L. Yang, B. Yan, L. Sun, P. Zhang, W. Zhang, Z. Sun, C. Lu, L. Yang, B. Yan, P. Zhang, W.
1696 Zhang, Z. M. Sun and L. Sun, *Adv. Funct. Mater.*, 2020, **30**, 2000852.
- 1697 248 C. Liu, Y. Bai, W. Li, F. Yang, G. Zhang and H. Pang, *Angew. Chem. Int. Ed.*, 2022, **61**,
1698 e202116282.
- 1699 249 L. Zhou, Q. Tian, X. Shang, Y. Zhao, W. Yao, H. Liu and Q. Xu, *Green Chem.*, 2024, **26**, 1454–
1700 1461.
- 1701 250 F. Yang, D. Deng, X. Pan, Q. Fu and X. Bao, *Natl Sci Rev*, 2015, **2**, 183–201.
- 1702 251 A. Wang, J. Li and T. Zhang, *Nat. Rev. Chem.*, 2018, **2**, 65–81.
- 1703 252 L. Zhang, K. Doyle-Davis and X. Sun, *Energy Environ. Sci.*, 2019, **12**, 492–517.
- 1704 253 X. F. Yang, A. Wang, B. Qiao, J. Li, J. Liu and T. Zhang, *Acc. Chem. Res.*, 2013, **46**, 1740–1748.



- 1705 254 S. Ding, M. J. Hülsey, J. Pérez-Ramírez and N. Yan, *Joule*, 2019, **3**, 2897–2929.
- 1706 255 R. Gusmão, M. Veselý and Z. Sofer, *ACS Catal.*, 2020, **10**, 9634–9648.
- 1707 256 Y. Sun, X. Tan, X. Zhang, Y. Wang, Z. Ju and Q. Kang, *Mater. Lett.*, 2025, **391**, 138467.
- 1708 257 Y. Lin, F. Yu, L. Li, Y. Li, R. Huang and Y. Wen, *ACS Catal.*, 2024, **14**, 16423–16433.
- 1709 258 H. Wang, X. Li, Y. Deng, J. Jiang, H. Ma and J. Zou, *Elsevier B.V.*, 2025, preprint, DOI:
1710 10.1016/j.ccr.2025.216462.
- 1711 259 F. Li, H. Ai, C. Shi, K. H. Lo and H. Pan, *Int. J. Hydrog. Energy.*, 2021, **46**, 12886–12896.
- 1712 260 Y. H. Chen, M. Y. Qi, Y. H. Li, Z. R. Tang, T. Wang, J. Gong and Y. J. Xu, *Cell Rep Phys Sci.*,
1713 2021, **2**, 100371.
- 1714 261 D. Zhao, Z. Chen, W. Yang, S. Liu, X. Zhang, Y. Yu, W. C. Cheong, L. Zheng, F. Ren, G. Ying, X.
1715 Cao, D. Wang, Q. Peng, G. Wang and C. Chen, *J. Am. Chem. Soc.*, 2019, **141**, 4086–4093.
- 1716 262 H. Bao, Y. Qiu, X. Peng, J. ao Wang, Y. Mi, S. Zhao, X. Liu, Y. Liu, R. Cao, L. Zhuo, J. Ren, J.
1717 Sun, J. Luo and X. Sun, *Nat. Commun*, 2021, **12**, 1–9.
- 1718 263 Z. Liu, Y. Liu, J. Zhang, T. Cao, Z. Sun, J. Liu and H. Shang, *Nano Res.*, 2024, **17**, 3911–3918.
- 1719 264 H. Hu, J. Wang, P. Tao, C. Song, W. Shang, T. Deng and J. Wu, *J. Mater. Chem. A*, 2022, **10**,
1720 5835–5849.
- 1721 265 H. Yang, Q. Lin, C. Zhang, X. Yu, Z. Cheng, G. Li, Q. Hu, X. Ren, Q. Zhang, J. Liu and C. He, *Nat.*
1722 *Commun.*, 2020, **11**, 1–8.
- 1723 266 N. Li, X. Wang, X. Lu, P. Zhang and W. J. Ong, *Chem. Eur. J.*, 2021, **27**, 17900–17909.



- 1724 267 N. Li, J. Peng, Z. Shi, P. Zhang and X. Li, *Chin. J. Catal.*, 2022, **43**, 1906–1917.
- 1725 268 M. A. U. Din, S. S. A. Shah, M. S. Javed, M. Sohail, A. ur Rehman, M. A. Nazir, M. A. Assiri, T.
- 1726 Najam and N. Cheng, *Chem. Eng. J.*, 2023, **474**, 145700.
- 1727 269 D. Gao, Y. Zhang, Z. Zhou, F. Cai, X. Zhao, W. Huang, Y. Li, J. Zhu, P. Liu, F. Yang, G. Wang
- 1728 and X. Bao, *J. Am. Chem. Soc.*, 2017, **139**, 5652–5655.
- 1729 270 S. S. A. Shah, M. Sufyan Javed, T. Najam, C. Molochas, N. A. Khan, M. A. Nazir, M. Xu, P.
- 1730 Tsiakaras and S. J. Bao, *Coord. Chem. Rev.*, 2022, **471**, 214716.
- 1731 271 Y. Sun, Q. Wang, Z. Geng, Z. Liu and R. Yang, *Chem. Eng. J.*, 2021, **415**, 129044.
- 1732 272 J. C. Yan, F. M. Wang, S. Yin, J. Zhang, W. Jiang and G. G. Liu, *Rare Metals*, 2025, **44**, 2239–
- 1733 2267.
- 1734 273 T. S. Bui, E. C. Lovell, R. Daiyan and R. Amal, *Adv. Mater.*, 2023, **35**, 2205814.
- 1735 274 Z. Cai, Y. Wu, Z. Wu, L. Yin, Z. Weng, Y. Zhong, W. Xu, X. Sun and H. Wang, *ACS Energy Lett.*,
- 1736 2018, **3**, 2816–2822.
- 1737 275 L. Yang, J. Du, J. Deng, N. H. M. Sulaiman, X. Feng, C. Liu and X. Zhou, *Small*, 2024, **20**,
- 1738 2307007.
- 1739 276 S. Li, H. Chai, L. Zhang, Y. Xu, Y. Jiao and J. Chen, *J. Colloid Interface Sci.*, 2023, **642**, 235–
- 1740 245.
- 1741 277 Y.-T. Liu, P. Zhang, N. Sun, B. Anasori, Q.-Z. Zhu, H. Liu, Y. Gogotsi, B. Xu, Y. Liu, P. Zhang, N.
- 1742 Sun, Q. Zhu, H. Liu, B. Xu, B. Anasori and Y. Gogotsi, *Adv. Mater.*, 2018, **30**, 1707334.



- 1743 278 Z. Otgonbayar, C. M. Yoon and W. C. Oh, *Chem. Eng. J.*, 2023, **464**, 142716.
- 1744 279 J. Y. Kim, W. T. Hong, T. K. C. Phu, S. C. Cho, B. Kim, U. Baeck, H. S. Oh, J. H. Koh, X. Yu, C. H.
- 1745 Choi, J. Park, S. U. Lee, C. H. Chung and J. K. Kim, *Adv. Sci.*, 2024, **11**, 2405154.
- 1746
- 1747
- 1748
- 1749



Data Availability Statement

The data will be available upon request to the authors.

